UQAC
Université du Québec
à Chicoutimi

DISSOLUTION KINETICS OF ALUMINA INJECTED IN CRYOLITIC MELT: THERMAL AND CHEMICAL INFLUENCES ON THE SHERWOOD NUMBER

PAR JONATHAN ALARIE

THESIS PRESENTED TO L'UNIVERSITÉ DU QUÉBEC À CHICOUTIMI IN PARTIAL FULFILLMENT OF THE REQUIREMENTS FOR THE DEGREE OF PHILOSOPHIÆ DOCTOR (PH.D.) IN THE SUBJECT OF ENGINEERING

QUÉBEC, CANADA

RÉSUMÉ

Les défis rencontrés dans la production d'aluminium primaire sont de plus en plus préoccupants en raison des enjeux liés à la performance environnementale et énergétique. L'un de ces défis majeurs réside dans l'introduction, la dissolution et la répartition d'importantes quantités d'alumine dans un faible volume d'électrolyte. De plus, cette introduction se fait sur une grande surface horizontale en utilisant un nombre limité de points d'injection distincts. Généralement, environ un kilogramme d'alumine est injecté à chaque point d'injection toutes les minutes. Cependant, la poudre d'alumine a tendance à s'agglomérer rapidement, formant des radeaux qui entravent le contact solide-liquide, réduisant ainsi la vitesse de dissolution. Par conséquent, la formation et la dissolution de ces radeaux d'alumine dans le procédé Hall-Héroult génèrent un délai significatif entre l'injection et la disponibilité pour la réduction en vue de produire de l'aluminium.

La dissolution de l'alumine dans la cryolite a fait l'objet de nombreuses études dans la littérature, couvrant un large éventail de conditions présentées de manière variée. Afin de comparer ces résultats, un modèle empirique a été développé en se basant sur des données expérimentales obtenues à l'aide d'une méthode gravimétrique spécialement développée pour ce projet de recherche et appliquée à des disques d'alumine non poreux. Ce modèle a ensuite été appliqué aux données disponibles dans la littérature, révélant des différences significatives entre les ensembles de données. Ces variations sont ensuite analysées et discutées afin d'en identifier les causes principales. Elles sont principalement attribuées à trois facteurs majeurs ayant une influence significative sur la dissolution : la morphologie de l'alumine, l'écoulement du bain autour des échantillons, ainsi que la fraction massique des additifs dans le bain de cryolite, incluant l'alumine dissoute.

Une fois ces hypothèses confirmées, il est impératif de déterminer la diffusivité moléculaire de l'alumine dans l'électrolyte pour décrire de manière adéquate le phénomène de dissolution. Cette information permet d'utiliser les relations de transfert de masse pour estimer la diffusion de l'alumine, selon la loi de Fick. Les travaux de doctorat proposent d'utiliser l'équation de Wilke-Chang pour calculer la diffusivité moléculaire de l'alumine et ainsi tenir compte de l'influence de la composition chimique du bain sur la mobilité de l'alumine dissoute. Les données recueillies ont été utilisées pour développer un modèle plus général basé sur le nombre de Sherwood, permettant de prédire le taux de dissolution de la surface d'alumine dans des conditions spécifiques.

Ensuite, en utilisant une description détaillée du transfert de chaleur et de la diffusivité, la théorie générale du transfert de masse a été appliquée à nouveau aux données disponibles dans la littérature pour identifier leurs taux de dissolution respectifs. Le contraste entre les données expérimentales et la validation fournie par la littérature est semble découler de la morphologie de l'échantillon et de la description adéquate de

l'écoulement qui l'entoure. Les discussions ultérieures mettent en évidence le facteur prédominant affectant les coefficients de transfert de masse et identifient les défis théoriques à relever pour obtenir des relations plus précises dans les travaux futurs.

Une fois le modèle de diffusivité confirmé, il est crucial de comprendre la cinétique des interactions entre le solide et le liquide conduisant à la formation et à la dissolution des radeaux. En utilisant la théorie de l'agglomération humide, la suite de la thèse présente une analyse approfondie de la formation des radeaux et des échanges thermiques dans cette phase précoce. Cette analyse théorique permet ensuite d'estimer la taille initiale du nuage d'alumine produit lors de l'injection. Enfin, la thèse utilise une analyse dimensionnelle pour quantifier le taux de dissolution et de désintégration du radeau d'alumine ainsi formé. Une approche théorique est proposée pour comprendre les comportements clés observés lors d'expériences approfondies sur la dissolution de différentes formes macroscopiques d'alumine. En conclusion, l'application potentielle du modèle proposé est également abordée.

Les travaux présentés permettent ainsi de comprendre:

1. L'influence des additifs du bain sur la diffusivité de l'alumine.
2. L'impact du frittage de l'alumine sur la structure interne du radeau.
3. Les mécanismes de transfert de masse interne au radeau.

Ces apprentissages permettront d'obtenir une meilleure compréhension de la répartition spatiale et temporelle de l'alumine dans les cuves d'électrolyse. Ceci permettra une optimisation des stratégies d'opération des cuves, notamment les fréquences d'alimentation. En ayant une prédiction plus précise du taux de dissolution de l'alumine et de sa diffusivité, il sera possible de diminuer les effets d'anode et la création de boue en fournissant la bonne quantité d'alumine au bon moment.

ABSTRACT

The challenges encountered in the production of primary aluminum are increasingly worrying due to issues related to environmental and energy performance. One of these major challenges lies in the introduction, dissolution, and distribution of large quantities of alumina in a small volume of electrolyte. In addition, this introduction is carried out over a large horizontal surface using a limited number of distinct injection points. Typically, approximately one kilogram of alumina is injected at each injection point every minute. However, alumina powder tends to agglomerate quickly, forming rafts that impede solid-liquid contact, thereby reducing the dissolution rate. Therefore, the formation and dissolution of these alumina rafts in the Hall-Héroult process generates a significant delay between injection and availability for reduction to produce primary aluminum.

The dissolution of alumina in cryolite has been the subject of numerous studies in the literature, covering a wide range of conditions presented in a varied manner. In order to compare these results, an empirical model was developed based on experimental data obtained using a gravimetric method specially developed for this research project and applied to non-porous alumina disks. This model was then applied to data available in the literature, revealing significant differences between the data sets. These variations are then analyzed and discussed in order to identify the main causes. They are mainly attributed to three major factors having a significant influence on dissolution: the morphology of the alumina, the flow pattern around the different samples studied, as well as the mass fraction of the additives in the cryolite bath, including the dissolved alumina.

Once these hypotheses are confirmed, it is imperative to determine the molecular diffusivity of alumina in the electrolyte to adequately describe the dissolution phenomenon. This information makes it possible to use mass transfer relations to estimate the diffusion of alumina, according to Fick's law. The doctoral work proposes using the Wilke-Chang equation to calculate the molecular diffusivity of alumina and thus take into account the influence of the chemical composition of the bath on the mobility of dissolved alumina. The different conditions used, similar to those encountered in industry, modified the flow pattern in the experimental setup, and a thermal was analysis attempted to reproduce this influence as best as possible. The data collected was used to develop a more general model based on the Sherwood number, allowing the prediction of the dissolution rate of the alumina surface under specific conditions.

Then, using a detailed description of heat transfer and diffusivity, the general mass transfer theory was applied to the data available in the literature to identify their respective dissolution rates. The contrast between the experimental data and the validation provided by the literature is assumed to arise from the morphology

of the sample and the adequate description of the flow surrounding it. Subsequent discussions highlight the predominant factor affecting mass transfer coefficients and identify theoretical challenges to obtain more precise relationships in future work.

Once the diffusivity model is confirmed, it is crucial to understand the kinetics of solid-liquid interactions leading to the formation and dissolution of rafts. Using wet agglomeration theory, the remainder of the thesis presents an in-depth analysis of raft formation and heat exchange in this early phase. This theoretical analysis then makes it possible to estimate the initial size of the alumina cloud produced during injection. Finally, the thesis uses dimensional analysis to quantify the rate of dissolution and disintegration of the alumina raft thus formed. A theoretical approach is proposed to understand the key behaviors observed during extensive experiments on the dissolution of different macroscopic forms of alumina. In conclusion, the potential applications of the proposed model are also discussed.

The work presented thus allows the understanding of:

1. The influence of bath additives on alumina diffusivity.
2. The impact of alumina sintering on the internal structure of the raft.
3. Internal mass transfer mechanisms in the raft.

These learnings will provide a better understanding of the spatial and temporal distribution of alumina in electrolysis cells. This will allow optimization of cell operating strategies, including feed frequencies. By having a more accurate prediction of the alumina dissolution rate and its diffusivity, it will be possible to reduce anode effects and sludge creation by providing the right amount of alumina at the right time.

REMERCIEMENTS

J'aimerais tout d'abord remercier ma conjointe, Karine Boivin Forcier, pour son support inconditionnel pendant mes études. Il s'agissait initialement d'un projet un peu fou d'effectuer un retour aux études loin de la maison et des enfants. Ce projet de baccalauréat s'est ensuite prolongé en des études de cycles supérieurs et puis un déménagement dans une nouvelle ville. Tout au long de ce parcours, elle a toujours été là pour tenir le fort, souvent seule avec nos jeunes enfants. Sa résilience et son endurance ont permis la production du travail présenté dans les prochaines pages.

Ensuite, il va sans dire que tout ceci n'aurait pas été possible sans l'appui du Professeur László Kiss. Mon projet initial était simplement de devenir ingénieur. Cependant, celui-ci a su voir mon potentiel et m'amener vers la recherche. À son contact, j'ai pris goût aux défis de la recherche universitaire et c'est donc grâce à lui que je me suis lancé dans ce projet, malgré les défis à venir. Il a été témoin des hauts et des bas liés à mon parcours particulier et a toujours su trouver les bons mots pour me remettre en selle. Ce fut pour moi un honneur de connaître et travailler avec cet homme d'exception.

La présente thèse leur est évidemment dédiée.

J'aimerais aussi exprimer un remerciement spécial à mon co-directeur Pr. Lukas Dion pour ses conseils et sa patience. Si Pr. Kiss a su m'inculquer le niveau technique nécessaire pour réussir cette entreprise, Pr. Dion m'a quant à lui permis de tirer le meilleur de moi-même dans cette entreprise, tout en me gardant les pieds sur terre.

Tout ce travail aurait été impossible sans le support de bon nombre d'autres personnes. En cela j'aimerais remercier mes collègues du GRIPS, passés et présents, qui m'ont aidé dans cette entreprise : Patrice Paquette, Sándor Poncsák, Guillaume Bonneau, Martin Truchon, Thomas Roger, Thomas Richer, Lovatiana Rakotondramanana et Samuel Théberge. Nous avons partagé de bons moments que je garderai précieusement en mémoire.

Bien entendu, un grand merci à nos partenaires dans cette aventure, Sébastien Guérard et Jean-François Bilodeau, mais aussi Renaud Santerre dont le décès nous a privés de son humour et sa personnalité rayonnante. Ils ont toujours été présents pour me ramener à des considérations plus pratiques lors de nos trop rares et brèves rencontres. Leur expertise de terrain a joué un grand rôle dans le succès de ce travail.

Je dois aussi exprimer ma reconnaissance aux différents organismes qui ont financé mes études et m'ont permis de me concentrer exclusivement sur celles-ci. Au cours de ces années, j'ai donc pu compter sur l'appui financier des bourses du CRSNG, du FRQNT, de la Fondation de l'UQAC et de ses généreux donateurs, de Rio Tinto, du Regal et de ses partenaires, ainsi que de l'Ordre des ingénieurs du Québec.

TABLE OF CONTENTS

LIST OF TABLES

LIST OF FIGURES

CHAPTER I
INTRODUCTION

1.1 PRESENTATION

The extraction of aluminum is done by the electrolysis of alumina dissolved in an electrolyte. In steady-state operation, this bath is mainly composed of molten cryolite (Na_3AlF_6) and a proportion between 12 and 23 weight percent of additives [1]. The additives are used to reduce the operation temperature of the electrolysis cell below the melting point of pure cryolite (1011 °C). A mass fraction of approximately 11 % of aluminum fluoride is thus added to it in order to reduce its liquidus temperature to around 960 °C. The presence of calcium fluoride is also non-negligible, with a mass proportion typically between 3 and 6 %. Usually, this additive is not intentionally added to the melt but comes from alumina impurities. However, its beneficial effect on the evaporation of the bath and the infiltration of the sodium in the carbon of the cell makes a small amount of calcium fluoride desirable inside the cell. Finally, the presence of dissolved alumina fluctuating between 1 and 4 weight percent will, of course, lead to periodic variation in its liquidus. Although the additives present in the cryolite bath mainly serve to lower the liquidus temperature of the mixture, the chemical composition of the electrolyte will also influence the properties of the bath (see [2, 3, 4, 5, 6, 7]). Movement, heat and mass exchanges will therefore be influenced by the composition of the electrolyte [8]. The study presented here focuses on the mass exchange between the powdery alumina injected at the surface of the bath.

This study takes on its full meaning when considering the phenomena involved in the dissolution of alumina and presented in Figure 1.1. First, about 1 kg of alumina

powder is dropped on the surface of the liquid. Upon impact, a small amount of this alumina will be incorporated into the bath, while most of the mass will spread over the surface to form a raft [9]. From this moment on, exchanges of heat and mass, internal to the rafts formed, will cause the agglomeration of the heap of powder. Subsequently, the dissolution will take place almost exclusively between the nominal surface of the raft and the liquid [10]. As the dissolution weaken the bond between the alumina particles, the parent raft (created upon the injection) will start to disintegrate in smaller "secondary" rafts. These secondary rafts will then experience dissolution in a completely different manner from the parent raft, as explained in Chapter 4. This results in a still poorly defined delay between the injection and the complete dissolution of the dose of alumina. During this time, the raft can remain on the surface of the bath or sink and move around in the volume of the liquid. The migration patterns of these rafts are still unknown, but they necessarily result in a heterogeneous spatial distribution of dissolved alumina [11].

In addition to the spatial distribution, the proportion of dissolved alumina also varies over time. This variation comes from the process control strategy. The mass fraction of alumina in the electrolytic cells is not monitored in real-time. To overcome this situation, the current strategy for alumina feeding consists of a period of overfeeding, to increase the mass fraction until an approximate quantity is reached, followed by a period of underfeeding to consume the excess of alumina in the electrolyte. Combined with the spatial variations described above, it is evident that some areas, such as the extremity of the cell, could move substantially away from the operating target as demonstrated by Dion et al. [12]. It is therefore important to understand the effects of too much or too little dissolved alumina in an electrolytic cell.

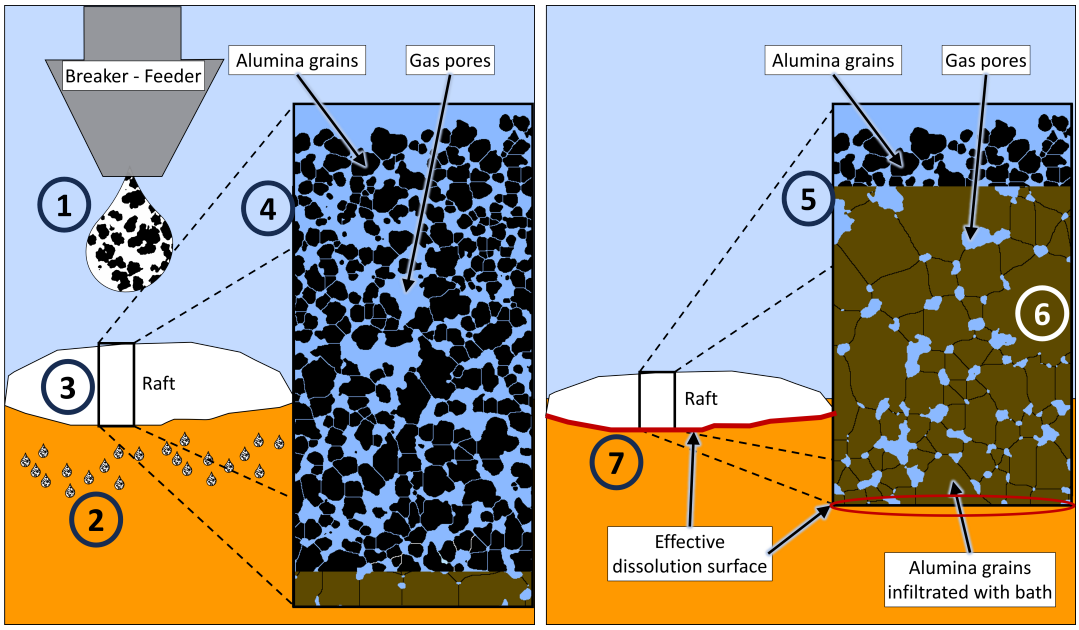

(a) Main steps of the injection. The alumina powder is dropped on the surface of the bath (1). Then a part of the powder is incorporated in the bath (2), while the rest of the batch creates a raft (3). At this moment, the raft is mainly composed of dry powder (4).

(b) Main steps of the dissolution. The powder is infiltrated by the bath (5). Then the alumina agglomerates (6). Finally, the dissolution occurs from the bottom of the raft (7).

Figure 1.1 : Schematic of the injection and dissolution of a batch of alumina powder.

It is generally recognized that a mass proportion of fewer than 1.3 weight percent of alumina favors the onset of the anode effect [13]. The anode effect is known to appear when the current density reaches a critical value for the amount of dissolved alumina in the bath [14, 15]. Typically, current density above 1.1 A/cm^2 can lead to an anode effect when the alumina content drops below 1.5 w% [16, 1]. In such a case, the current is strong enough to cause the electrolysis of the bath, which forms perfluorocarbon gases. These gases have a lower angle of contact with the carbon of the anodes than CO_2 and therefore form an insulating layer between the anode and the bath. The

electrical insulation of a large portion of the anode will increase the current density of the free portions, favoring the amplification of the anode effect. In addition to its self-sustaining character, the anode effect increases the production of heat by the Joule effect, which quickly leads to the degradation of the pot and the overconsumption of energy. Another point of importance is that perfluorocarbon gases are greenhouse gases with a warming potential up to 11,100 times greater than CO_2. Knowing that these emissions represent up to 5 % of emissions in equivalent tonnes of CO_2 [17], they can also be easily eliminated by an adequate alumina feeding strategy.

Conversely, an overabundance of dissolved alumina in the bath favors the formation of sludge under the bed of molten metal. It is well known that an exchange phenomenon exists between the bath and the underside of the metal to form therein sludge, more or less rich in alumina. This sludge is distributed unevenly over the carbon cathode surface at the bottom of the pots and locally increases the electrical resistance of the cell. In addition, the alumina present in the sludge accumulates in clusters of corundum, practically impossible to dislodge. These corundum plates being an electrical insulator, the local perturbation of the electric field that ensues becomes permanent. This increases the local current density in the vicinity of these plates, which causes premature wear on portions of the pot, limiting its lifespan. Better control of the amount of alumina dissolved in the electrolyte helps to limit the formation of sludge and therefore the permanent damage to the electrolysis cell. These examples of impacts of poor management of the quantity of alumina dissolved in the bath can be mitigated, thanks to a better knowledge of the kinetics of the dissolution of the alumina after its injection.

1.2 THESIS OBJECTIVES

Quantitatively characterize the factors that influence the formation of rafts and their dissolution.

This objective can be achieved through the following secondary objectives:

1. Determine the optimal chemical and physical conditions for dissolving alumina in cryolite;
2. Determine the mass transfer coefficient of alumina in cryolite as a function of the morphology of the alumina, the physicochemical properties of the bath, the temperature and flow conditions;
3. Identify the dissolution mechanisms of alumina;
4. Understand the phenomena surrounding the formation of alumina powder rafts;
5. Explain the structure of rafts and their formation conditions;
6. Determine favorable conditions for the formation and disintegration of rafts.

To achieve the objectives concerning the dissolution of alumina, the project includes a parametric study looking at of the chemical and thermal conditions as well as the macroscopic structure of alumina in a cryolite bath. The objectives concerning the formation and structure of the rafts will also benefit from a similar parametric study to produce rafts, with the help of a few scanning electron microscope observations.

Two major subjects will therefore be studied in this research project: the agglomeration of powder into alumina rafts and the dissolution of alumina.

1.3 LITERATURE REVIEW

The sintering and dissolution phenomena have in common dependence on the surface energy of alumina [18]. Indeed, the dissolution of alumina depends on the bonds that can be created between the solvent and the solute. However, the chemical species present on the surface of alumina to create these bonds depend on the surface energy [19]. In addition, the persistent agglomeration of alumina comes from the sintering of the grains. Through sintering, alumina seeks to increase its stability by reducing its surface energy. The alumina rafts thus limit the flow of dissolved alumina into the cells. However, the available literature is usually focused on one subject at a time and then this literature review should follow this scheme. The literature on the dissolution is first presented, then the topic of the agglomeration of the alumina is synthesized. Note that a part of the dissolution review is present both in this section and in Chapter 1, but this section aims to regroup them in a more convenient section.

1.3.1 DISSOLUTION

Alumina dissolution has been the subject of much research over the years. As such, several authors have published data on the subject, and Table 1.1 summarizes the main relevant research findings presented below. In addition, Table 1.2 shows the relative effects of bath additives on the dissolution rate.

Table 1.1 : Dissolution rates available in the literature [20].

Reference	value	unit	value	unit	Conditions
Thonstad (1988) [21]	0.035	g/cm^2·s	5.8	g/cm^2·s	Rotating pressed tablet, 39 rpm
	0.1	g/cm^2·s	16.7	g/cm^2·s	Rotating pressed tablet, 325 rpm
	0.04	g/cm^2·s	6.7	g/cm^2·s	Sintered corrundum, 325 rpm
Y. Yang et al. (2015) [22]	0.25	w%/min	4.17	mg/g·s	Powder injection, [Al_2O_3] < 3 %
	0.19	w%/min	3.17	mg/g·s	Powder injection, [Al_2O_3]= 4 w%
	0.14	w%/min	2.33	mg/g·s	Powder injection, [Al_2O_3]= 5 w%
	0.12	w%/min	2	mg/g·s	Powder injection, [Al_2O_3]= 6 w%
	0.09	w%/min	1.5	mg/g·s	Powder injection, [Al_2O_3]= 7 w%
Z. Lubyova et al. (1995) [23]	10.75	mg/s	1.39	mg/g·s	Powder injection
	12	mg/s	1.28	mg/g·s	Powder injection
	11.32	mg/s	1.29	mg/g·s	Powder injection
Y. Yang et al. (2015) [24]	1.58	g/min	5.3	mg/g·s	Powder injection, [Al_2O_3]= 0 %
	1.38	g/min	4.6	mg/g·s	Powder injection, [Al_2O_3]=1 w%
	1.23	g/min	4.1	mg/g·s	Powder injection, [Al_2O_3]=2 w%
	1.18	g/min	3.9	mg/g·s	Powder injection, [Al_2O_3]=3 w%
	1.15	g/min	3.8	mg/g·s	Powder injection, [Al_2O_3]=4 w%

Table 1.2 : Influence of physicochemical parameters of the bath on the dissolution, relative to the effect of 1 °C of superheating [25].

Ref.	AlF_3 (w%)	CaF_2 (w%)	Al_2O_3 (w%)	Agitation	Convection
Gerlach [26]	1	1	7	N/D	Rotating discs at 200 rpm
Kushel [27]	1[1]	1[1]	4	> 6	Agitation from 3 to 15 cm/s
Vasyunina [28]	1[1]	1	N/D	2	Agitation from 0 to 10 cm/s
Yang [22]	1[1]	N/D	5	N/D	No agitation

[1]Expressed as cryolite ratio

These data will serve as a basis for comparison with those collected in the project. It should be noted, however, that the method used and the type of alumina studied can greatly influence the dissolution rate. To this end, it is sufficient to compare Thonstad's data with the others, in the table 1.1, to have proof of this. Hereafter are reported the methods and conclusions of some of the most important works about alumina dissolution.

Dando et al. [29] observed the dissolution of alumina injected into cryolite with a camera and measured the mass fraction of dissolved alumina by voltammetry, coupled with a rotating electrode. In addition, the bath was agitated throughout the process by a mechanical stirrer. The study focused on the effect of preheating the alumina on the dissolution rate. Increasing the injection temperature slightly increased the dissolution rate.

Gerlach et al. [26] used a setup consisting of a conical crucible containing about 150 g of melt stirred by a propeller at 200 rpm to dissolve pressed alumina discs. They found some correlations between the dissolution rate and several crystal structures of alumina as well as with the addition to the bath of AlF_3, CaF_2, NaF, and LiF and temperature. Of these additives, only NaF had a similar behavior with temperature and increased the dissolution rate, the others decreased it.

Haverkamp et al. [30] refined a voltammetric method to measure the dissolved alumina content in a 600 g bath. They used this setup to determine the influence of bath velocity, dissolved alumina concentration, and superheat on the dissolution rate. They demonstrated that increasing superheat and fluid velocity increases the dissolution rate while increasing alumina concentration decreases it.

Kuschel et al. [27] worked on the injection dissolution of 70 g to 150 g of alumina with a combined voltammetric and visual method. Using these methods, they addressed an extensive list of bath characteristics including stirring, superheat, alumina concentration, and cryolite ratio. For alumina, they studied its dispersion, particle size, moisture content (MOI, moisture on ignition, and LOI, loss on ignition), density, α-alumina content, and fluidity. They determined that the properties of the fluid were more important than those of the alumina.

Liu et al. [31] focused on the effect of the crystal structure of alumina on its dissolution. Thus, using a 1 kg bath stirred by a graphite propeller and the thermal reaction of the bath during injection, they demonstrated that γ-alumina dissolves faster than α-alumina.

Lubyova et al. [23] attempted to determine the influence of the α-alumina content of the powder and different concentrations of fluorinated additives based on calcium, potassium, lithium, and aluminum by the isothermal saturation method in a non-stirred bath. However, no clear conclusions could be drawn from this method, except that the addition of additives decreases the dissolution rate of alumina and its solubility.

In parallel with his studies on agglomeration, Johnson [32] attempted to describe the dissolution behavior of alumina. Thus, he stated that the agglomeration behavior of alumina was in some way opposite to the ease of the dissolution of alumina. Specifically, the dissolution rate of alumina increased with agitation, small particle size, α-alumina content of the particles, and lack of dissolved alumina in the bath.

Rye et al. [33] injected a mass fraction of 2 % of primary and secondary alumina into a bath stirred by argon bubbles. This setup was used to characterize the effect on the dissolution of different α-alumina contents, particle size, preheating temperature, and superheating using a voltammetric method. These studies showed the positive effects on the dissolution rate of preheating and superheating.

Thonstad et al. [21] have extensively used the rotating disk method to measure alumina dissolution in conjunction with a voltammetric method. They have also experimented with different alumina configurations, i.e., pressed tablets, sintered disks, and powder injection at 1025 °C, into a liquid stirred by a propeller at 200 rpm. For this study, Thonstad et al. have published quantitative data on the dissolved alumina flux.

Vasyunina et al. [28] also used an electrochemical technique to measure the dissolution rate of alumina. They tried to find the effect of cryolite ratio, agitation, and dissolved alumina content of the bath. They also confirmed that increasing the additives decreases the dissolution rate and agitation increases it.

Yang et al. [22, 24, 34] have published several recent studies on alumina dissolution. They therefore used both a gravimetric and a visual method to confirm the trends previously discussed here. Not surprisingly, their results are similar to those available in the literature.

In summary, most of the important characteristics that can influence dissolution have been investigated. However, very little quantitative data has been associated with the direct influence of these parameters. This is why the research project presented here focuses on parametric studies with a gravimetric method. This method has the advantage of being very sensitive to the phenomena studied, unlike visual and electrochemical methods.

1.3.2 AGGLOMERATION

When alumina is injected into the cryolitic bath, an aggregation of the powder is formed due to the liquid bond between the grains. These bounds then solidify through a phenomenon known as sintering. Thus, the formation of rafts is a complex phenomenon involving mass and heat transfers in a multiphase system.

Sintering is a mass transfer process in which a particle tends to decrease its surface energy [35]. Through this process, the intragranular porosities can be filled with solid material and intergranular porosities will also decrease as the particles enlarge, especially at the point of contact between particles [36].

In order to achieve this, an energy barrier must be overcome [37], which can be achieved by the combined effect of temperature and the presence of a catalyst for the reaction. These two conditions favor the movement of the atoms, usually through evaporation condensation, in dry sintering, or a dissolution-precipitation process, in wet sintering. Note that the dissolution-precipitation process is much more rapid than the evaporation condensation [38].

In the present work, the base particles that will sinter are the α-alumina seeds present in an alumina grain, instead of the grain itself. It is easy to understand that the growing structure, upon contact of the alumina with the liquid cryolite, is the so-called platelets. This approach will be detailed later in Chapter 5. For now, here is the presentation of how the available literature for the agglomeration of alumina in electrolysis cells has been documented by past authors.

Dando et al. [29] studied alumina agglomeration by recovering rafts in industrial cells a few minutes after the injection. In addition, they made a mixture of alumina and powder bath in the laboratory, which they heated together up to 700 °C for 12 hours to form agglomerates. With these two types of samples, they made longitudinal sections at different heights to observe the structure. After polishing, scanning electron microscope images of these samples were compared. These images showed that the formation of alumina platelets ensures the cohesion of the rafts.

Gylver et al. [39] studied factory-produced primary and secondary alumina rafts by observation until the rafts disappeared or were recovered. In parallel, they collected information on the properties of the bath with a STARprobe®in addition to the bath height and the age of the anodes. Bath samples were also used to confirm the properties of the bath. The results of this study show that the rafts remain on the bath surface for

5 to 140 seconds. Furthermore, this time is strongly influenced by the available bath surface and the intensity of its circulation. To a lesser extent, the moisture and fluorine content of the alumina as well as the acidity and temperature of the bath also influence the raft lifetime, unlike the alumina content of the bath and overheating.

Østbø [18] has probably carried out one of the most exhaustive studies on the agglomeration of alumina. He first attempted to study this phenomenon by a method similar to that of Walker, that is to say, the infiltration of a cylinder of powder contained in support composed of half steel and half aluminum foil. Thus, the aluminum melted in contact with the bath and was allowed to hold the powder in place before the formation of a crust. However, Østbø concluded that this method was not repetitive enough for the study of the agglomeration, but still allowed to observe the infiltration of alumina by the bath. He therefore made 1.2 g pellets composed of alumina added with fluoride. These pellets were heated in order to study the temperature and time effects on agglomeration. In addition, he focused on the amount of fluoride, moisture, and α-alumina in these pellets. Also, through a semi-quantitative classification of the agglomeration, he was able to determine that there is a qualitative difference between the sintering of primary and secondary alumina.

Thonstad et al. [40] sintered secondary alumina in a furnace without cryolite. They studied the effect of temperature and time by a qualitative evaluation of the sintering. These experiments showed that sintering begins in 1 minute to form completely solid aggregates in about 10 minutes. They also studied the evolution of the internal temperature of a cylinder of alumina powder, again according to the Walker technique, in a bath with a superheat of 10 °C and agitation by a carbon propeller rotating at 200 rpm.

Townsend et al. [41] focused on the formation of a solid crust by alumina in contact with the bath. They therefore injected doses of primary and secondary alumina of 2 g to 8 g into a 1600 g bath. They subsequently recovered these rafts approximately 3 minutes after injection into this bath having a bath ratio of 1.25 at 985 °C. In addition, they alternated between agitated and non-agitated baths using a propeller at 250 rpm. They subsequently evaluated the tendency for alumina to agglomerate with pictures of samples, previously freed from the bath with a chemical method. This allowed them to describe the dissolution behavior of γ-alumina and that of recrystallization in the form of α-alumina.

Johnson [32] experimented with crust formation on different alumina. The main characteristics studied were the effect of particle size, moisture content (LOI), BET surface area, and α-alumina content. This study was carried out in 300 g baths (ratios varying from 1.2 to 1.7), stirred or not, with 3 g injections at temperatures above 985 °C. These studies led to the recognition of the tendency for alumina agglomeration to decrease with LOI, stirring, temperature, small particle size as well as high α-alumina contents of the alumina and dissolved alumina in the bath.

Rye et al. [33] conducted several experiments on the injection of primary and secondary alumina with different particle sizes, insertion temperatures, and α-alumina content. It was found that preheating and the presence of impurities (secondary alumina) prevented the formation of crust.

As mentioned above, Walker [42] tried some approaches to study alumina rafts. He recovered industrial rafts and fabricated artificial agglomerates in the laboratory. He noted that crust formation decreases with increasing AlF_2, superheating, and stirring and that sintering increases with superheating.

1.4 ORIGINALITY

The literature review is synthesized here in Figure 1.2 and Table 1.3 for the part concerning the formation of rafts. When studying the alumina raft structure, different kinds of observations can be made. First, slices of the raft can be obtained by cutting the raft (Slice of the rafts). These kinds of observations give insight into the gradient of structure, if any, inside the raft. Second, observations of the whole raft (Whole raft) are useful to obtain the general evolution of the mass of the raft and its surface of exchange with the bath. Finally, punctual observations were undertaken to observe the structure evolution of the grains inside the raft. These last kinds of observations use magnification in the range of the alumina particle size and are taken randomly inside the raft.

Figure 1.3 and Table 1.4 synthesize the part concerning the kinetics of alumina dissolution. The methods used consist of electrochemical measurement of the dissolved alumina (voltammetry), direct observation of the dissolution (visual), measurement of the weight of the alumina after a given time (mass difference), chemical analysis of bath sample (bath sampling), and measurement of the temperature variation due to the presence of alumina in the bath (temperature). It can be seen that the current project stands out for the scope of the phenomena and parameters studied. Indeed, no previous work has simultaneously considered the bath chemistry, the properties of the alumina as well as the agitation and the superheating in the same study of the temporal evolution of the dissolution of the alumina.

The use of a methodology that first uses non-porous discs and then modifies the morphology of the alumina to a powdery state, also makes it possible to isolate the fundamental phenomena of dissolution and then add more complex phenomena related to the use of powders. Finally, the number of samples used to carry out the experiments,

Table 1.3 : Summary of work on alumina rafts.

Observations	**Industry**	**Laboratory**	
Slice of the raft	**Dando [29]**	**Dando [29]** **Alarie**	**Thonstad [40]**
Whole raft	*Gylver [43]* *Walker [42]*	*Dando [29]* *Johnson [32]* *Alarie*	*Walker [42]* *Townsend [41]*
Punctual		Johnson [32] Alarie	Østbø [18]

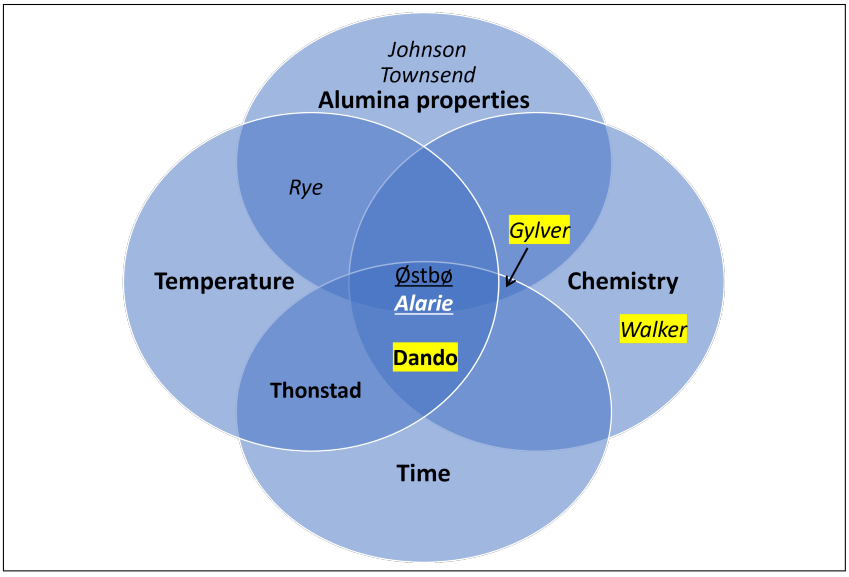

Figure 1.2 : Status of the project concerning the literature on raft formation. Table 1.3 is the legend of text formatting.

more than 400, gives an incomparable robustness in comparison to the few samples presented for each article in the literature.

Table 1.4 : Summary of works on the dissolution of alumina.

Method	Disk	Powder	
Voltammetry	**Thonstad [44, 21]**	**Jain [45]** **Dando [29]** **Rye [33]**	**Haverkamp [46, 30]** **Kuschel [27]** **Thonstad [44, 21]**
Visual	*Isaeva [47]*	*Vasyuniná [28]* *Kuschel [27]* *Alarie*	*Dando [29]* *Johnson [27]*
Difference mass	Alarie	Gylver [43] Alarie	Yang [24, 34]
Sampling bath	Frazer [48] Thonstad [44, 21] Gerlach [26]	Lubyová [23]	Thonstad [44, 21]
TEMPERATURE		LIU [31]	

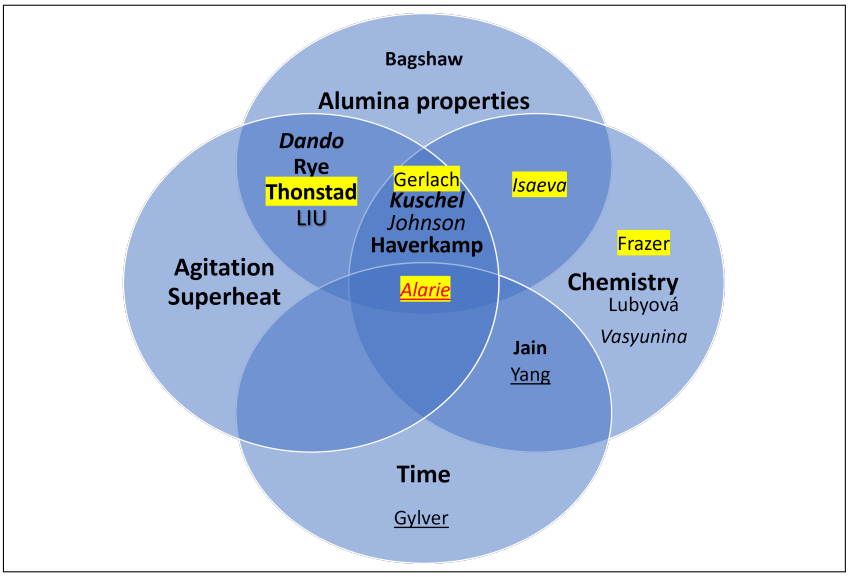

Figure 1.3 : Situation of the project concerning the literature on the dissolution of alumina. Table 1.4 is the legend of text formatting.

Ultimately, the project distinguishes itself from literature thanks to :

- The measuring method.
- The video recording method.

- The number of samples for each test.
- The number of structures studied.
- The number of conditions studied.
- The number of parameters studied.
- The analysis approach.

REFERENCES

[1] K. Grjotheim, *Introduction to aluminium electrolysis: understanding the Hall-Hérloult process*. Aluminium-Verlag, 1993.

[2] A. Solheim, S. Rolseth, E. Skybakmoen, L. Støen, Å. Sterten, and T. Støre, "Liquidus temperatures for primary crystallization of cryolite in molten salt systems of interest for aluminum electrolysis," *Metallurgical and Materials Transactions B*, vol. 27, no. 5, p. 739, 1996.

[3] H. Kvande and H. Rørvik, "Influence of bath density in aluminum electrolysis," *Journal of Metals*, vol. 36, pp. 62–62, 1984.

[4] T. Hertzberg, K. Tørklep, and H. Øye, "Viscosity of molten naf-alf3-al2o3-caf2 mixtures: Selecting and fitting models in a complex system," in *Essential Readings in Light Metals*. Springer, 1980, pp. 19–24.

[5] E. Skybakmoen, A. Solheim, and Å. Sterten, "Alumina solubility in molten salt systems of interest for aluminum electrolysis and related phase diagram data," *Metallurgical and materials transactions B*, vol. 28, no. 1, pp. 81–86, 1997.

[6] V. Daněk, O. Pataraák, and T. Østvold, "Surface tension of cryolite-based melts." *Canadian Metallurgical Quarterly*, vol. 34, no. 2, pp. 129–133, 1995.

[7] V. A. Khokhlov, E. Filatov, A. Solheim, and J. Thonstad, "Thermal conductivity in cryolitic melts-new data and its influence on heat transfer in aluminum cells," in *Light Metals 1998)*, 1998, pp. 501–506.

[8] Y. A. Cengel and A. J. Ghajar, *Heat and mass transfer : fundamentals & applications*, 5th ed. New York, N.Y.: McGraw-Hill Education, 2015.

[9] L. I. Kiss, "Alumina dissolution - a critical step in aluminum electrolysis," in *TMS 2018*, 2018, Conference Proceedings.

[10] J. Alarie, L. I. Kiss, L. Dion, M. Truchon, S. Guérard, and J.-F. Bilodeau, "Dimensional analysis applied to the dissolution and disintegration of alumina rafts : The riddle of dissolving alumina rafts solved." in *TMS light Metals*, TMS, Ed. Springer,

2024, Conference Paper.

[11] V. Bojarevics and M. Dupuis, *Advanced alumina dissolution modelling.* Springer, 2022, pp. 339–348.

[12] L. Dion, "Modelisation of perfluorocarbon emissions based on the alumina distribution and local current density in an aluminium electrolysis cell," Ph.D. dissertation, Université du Québec à Chicoutimi, 2018.

[13] J. Thonstad, *Aluminium electrolysis : fundamentals of the Hall-Héroult process*, 3rd ed. Düsseldorf: Aluminium-Verlag, 2001.

[14] J. Thonstad, T. Utigard, and H. Vogt, *On the Anode Effect in Aluminum Electrolysis*, 2000, pp. 131–138.

[15] A. T. Tabereaux and R. D. Peterson, *Chapter 2.5 - Aluminum Production.* Boston: Elsevier, 2014, pp. 839–917.

[16] S. Poncsák, "Formation et évolution des bulles de gaz au-dessous de l'anode dans une cuve d'électrolyse d'aluminium," Ph.D. dissertation, Université du Québec à Chicoutimi, Chicoutimi, 2000.

[17] H. Kvande, G. Saevarsdottir, and B. J. Welch, "Direct and indirect CO_2 equivalent emissions from primary aluminium production," in *Light Metals 2022.* Springer, 2022, pp. 998–1003.

[18] P. N. Østbø, "Evolution of alpha phase alumina in agglomerates upon addition to cryolitic melts," Ph.D. dissertation, Trondheim, 2002.

[19] M. C. Rastogi, *Surface and interfacial science : applications to engineering and technology.* New Delhi: Narosa, 2003.

[20] J. Alarie, T. Roger, L. I. Kiss, S. Poncsák, S. Guérard, and J.-F. Bilodeau, "Validation of the gravimetric method to properly follow alumina dissolution in cryolitic bath," in *Light Metals 2020.* Springer, 2020, pp. 680–687.

[21] J. Thonstad, A. Solheim, S. Rolseth, and O. Skar, "The dissolution of alumina in cryolite melts," in *Essential Readings in Light Metals*, 1988, pp. 105–111.

[22] Y. Yang, B. Gao, Z. Wang, Z. Shi, and X. Hu, "Effect of physiochemical properties and bath chemistry on alumina dissolution rate in cryolite electrolyte," *JOM*, vol. 67, no. 5, pp. 973–983, 2015.

[23] Z. Lubyová and V. Danek, "Control mechanism for alumina dissolution in cryolite melts," *Chemical Papers*, vol. 49, no. 2, pp. 59–63, 1995.

[24] Y. Yang, B. Gao, Z. Wang, Z. Shi, and X. Hu, "The formation and dissolution of crust upon alumina addition into cryolite electrolyte," *JOM*, vol. 67, no. 9, pp. 2170–2180, 2015.

[25] J. Alarie, L. I. Kiss, S. Poncsák, R. Santerre, S. Guérard, and J. F. Bilodeau, "Influence of additives on alumina dissolution in superheated cryolite melts." in *TMS 2021*. Springer, 2021, pp. 533–540.

[26] J. Gerlach, U. Hennig, and K. Kern, "The dissolution of aluminum oxide in cryolite melts," *Metallurgical and Materials Transactions B*, vol. 6, no. 1, pp. 83–86, 1975.

[27] G. Kuschel and B. Welch, "Effect of alumina properties and operation of smelting cells on the dissolution behaviour of alumina," *The Alumina Quality Workshop*, 1990.

[28] N. V. Vasyunina, I. P. Vasyunina, Y. G. Mikhalev, and A. M. Vinogradov, "The solubility and dissolution rate of alumina in acidic cryolite aluminous melts," *Russian Journal of Non-Ferrous Metals*, vol. 50, no. 4, pp. 338–342, 2009.

[29] N. Dando, X. Wang, J. Sorensen, and W. Xu, "Impact of thermal pretreatment on alumina dissolution rate and HF evolution." in *Light Metals*, 2010, pp. 541–546.

[30] R. G. Haverkamp and B. J. Welch, "Modelling the dissolution of alumina powder in cryolite," *Chemical Engineering and Processing: Process Intensification*, vol. 37, no. 2, pp. 177–187, 1998.

[31] J. Liu, M. Taylor, and M. Dorreen, "Response of cryolite-based bath to a shift in

heat input/output balance," *Metallurgical and Materials Transactions B*, vol. 48, pp. 1079–1091, 2017.

[32] A. R. Johnson, "Alumina crusting and dissolution in molten electrolyte," *Journal of Metals*, vol. 34, no. 3, pp. 63–68, 1982.

[33] K. A. Rye, S. Rolseth, J. Thonstad, and K. Zhanling, "Behaviour of alumina on addition to cryolitic baths," 1990.

[34] Y. Yang, Y. Li, Y. Huang, B. Gao, X. Hu, Z. Wang, W. Tao, F. Liu, Z. Shi, and J. Yu, "Formation and dissolution of crust upon alumina addition into cryolite electrolyte (ii)," *JOM*, vol. 71, no. 2, pp. 485–491, 2019.

[35] S.-J. L. Kang, *Sintering: densification, grain growth and microstructure*. Elsevier, 2004.

[36] R. M. German, *Sintering theory and practice*, 1996.

[37] M. G. Norton and C. B. Carter, "Sintering and grain growth," in *Ceramic Materials*. Springer New York, 2007, pp. 427–443.

[38] A. Ndayishimiye, "On a new process for the low temperature sintering of ceramics and multimaterials : the hydrothermal sintering. development and mechanistic approach," Ph.D. dissertation, Université de Bordeaux, 2017.

[39] S. E. Gylver, N. H. Omdahl, A. K. Prytz, A. J. Meyer, L. P. Lossius, and K. E. Einarsrud, "Alumina feeding and raft formation: Raft collection and process parameters," in *Light Metals 2019*. Springer, 2019, pp. 659–666.

[40] J. Thonstad, O. Kobbeltvedt, and S. Rolseth, "Agglomeration of alumina during dissolution in aluminium cells," *The Alumina Quality Workshop*, 1999.

[41] D. Townsend and L. Boxall, "Crusting behavior of smelter aluminas," in *Essential Readings in Light Metals*, 1984, pp. 613–621.

[42] D. I. Walker, "Alumina in aluminum smelting and its behavior after addition to cryolite-based electrolytes," Ph.D. dissertation, University of Toronto (Canada), Ann Arbor, 1993.

[43] S. E. Gylver, "Alumina dissolution in cryolite melts-formation and behavior of rafts," Ph.D. dissertation, NTNU, 2018.

[44] J. Thonstad, F. Nordmo, and J. Paulsen, "Dissolution of alumina in molten cryolite," *Metallurgical and Materials Transactions B*, vol. 3, no. 2, pp. 407–412, 1972.

[45] R. Jain, S. Tricklebank, B. Welch, and D. Williams, "Interaction of aluminas with aluminum smelting electrolytes," *Light Metals 1983*, pp. 609–622, 1983.

[46] R. Haverkamp, B. Welch, and J. Metson, "The influence of fluorination on the dissolution rate of alumina in smelter electrolyte," in *Light Metals - Warrendale*, 1994, pp. 365–365.

[47] L. A. Isaeva, A. B. Braslavskii, and P. V. Polyakov, "Effect of the content of the alpha-phase and granulometric composition on the dissolution rate of alumina in cryolite-alumina melts," *Russian Journal of Non-Ferrous Metals*, vol. 50, no. 6, pp. 600–605, 2009.

[48] E. J. Frazer and J. Thonstad, "Alumina solubility and diffusion coefficient of the dissolved alumina species in low-temperature fluoride electrolytes," *Metallurgical and Materials Transactions B*, vol. 41, no. 3, pp. 543–548, 2010.

CHAPTER II
METHODOLOGY

2.1 THESIS STRUCTURE

The present thesis is a collection of articles already published and reproduced here with the authorization of the editors. They represent the main milestones throughout the project. They are briefly introduced at the beginning of each chapter with their contribution and role in the achievement of the objectives of the thesis, along with the publication's information and the list of the symbols used.

The first article compares the state of the art of knowledge on alumina dissolution to the first results obtained with the gravimetric method. It also introduces the use of the Sherwood in such analysis to help the comparison.

The second article relates to the dissolution of alumina through a known boundary, that is to say, non-porous discs of alumina. It determines the direct interaction between the solid and the liquid as a change in the alumina diffusivity depending on the bath composition and temperature.

The third article revisits the results obtained in the literature with the findings about the alumina diffusivity. It serves as a new comparison basis for the results of the parametric study with the literature. It is also the first attempt to use general mass transfer correlations to the injection of alumina powder.

The last article uses the progress made and applies it to the injection of alumina and its dissolution in cryolite. The work carried out makes it possible to make a close

link between the well-known fundamental phenomena and the experimental results produced during a parametric study on the dissolution of alumina powder.

The work presented in these articles is based on an experimental setup (gravimetric system) specially designed to perform a parametric study on alumina dissolution.

2.2 EXPERIMENTAL SETUP

The gravimetric system allows the measurement of the variation of the sum of the forces on the sample, expressed in the form of weight. Thus, any phenomenon affecting the volume, or the mass of the sample will have an impact on the apparent weight. Figure 2.1 summarizes the main forces in action on a disc at the bath-air interface.

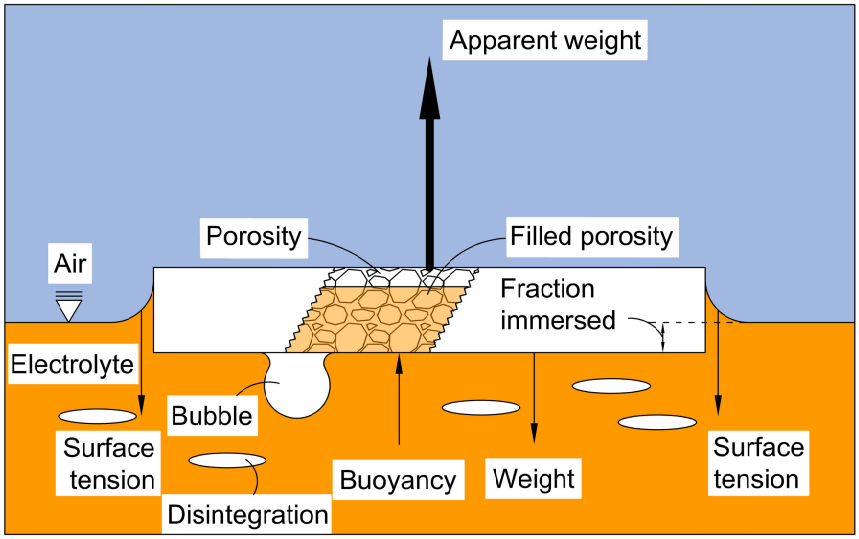

Figure 2.1 : Schematic of the force balance that influences the apparent weight measure on a disc.

The different forces will have different influences on the apparent weight of the sample, which represents the recording of the gravimetric apparatus. Thereafter, is presented this influence for each force in Figure 2.1, from right to left:

1. The contact between the solid and the liquid at the interface adds the surface tension to the sum of the forces.

2. The weight of the disc varies with the density of the sample and increases as the air in the porosities is filled with bath.

3. The immersed fraction of the disc is related to its buoyancy. As the immersed fraction increases, so does the buoyancy, and then the apparent weight diminishes accordingly.

4. Bubbles are created by the desorption of gas from the alumina grains. These bubbles appear in the porosities of the raft and push the bath outside of them. Therefore, the effective density of the disc decreases until the bubble escapes the raft. At this moment, the bath will replace the gas generated in the porosities and the raft will have a sudden increase in its apparent weight.

5. Disintegration of the raft occurs with porous samples. These events lead to a sudden drop in the weight of the disc.

It is also important to understand that the sample is supported by a load cell, which is, by definition, slightly flexible. In that case, a change in the weight of the sample can significantly influence the immersed fraction of the sample, and thus the buoyancy. Therefore, any change to the mass of the sample or its volume is damped by this small movement.

Typically, the samples are maintained at the desired depth, either at the surface or 25 mm beneath it, with a support made of Nichrome wire. This support is thin enough to prevent any distortion of the flow around the sample, generally being a simple cross of wire under the sample. In the case of injection of powder, a stainless steel ring can be added to obtain a raft of the desired diameter.

Also, the gravimetric system includes a camera to film the dissolution of the samples. This was particularly useful in the case of powder injection, where the shape of the samples changes over the test duration.

2.3 PARAMETRIC STUDY

Using this equipment, a parametric study was performed. Its objective is to quantify the effect of superheat, agitation, and variation in the mass fraction of additives commonly used in industrial electrolytes on the dissolution rate of different structures of alumina. The parametric study is then divided according to the structure of the alumina samples: non-porous discs, porous discs, and powder injection. This diversity of samples was designed to make it possible to verify the impact of the infiltration and porosity dynamics on the dissolution by isolating the physics as much as possible. The conditions of the experiments, along with the raw results for one sample, are described thereafter in order of increasing analysis complexity.

2.3.1 NON-POROUS DISCS

For the test on non-porous discs, a disc of approximately 40 g of alumina is first preheated for 5 minutes at 25 mm above the bath. Then, it is immersed in a cryolite bath of approximately 13 kg for 30 minutes. As observed in the preliminary experiments,

less than half of the sample is dissolved for each test. Thus, the increase in the mass fraction of alumina in the bath will be less than 0.15 w% for each dissolved sample. During this time, the bath temperature is kept constant at ±1 °C of the target superheat to maintain stable natural convection in the crucible. In order to ensure the repeatability of an experiment, 6 samples are dissolved sequentially in the same bath. It should be noted, however, that the conditions of each of these samples, although similar, are not identical due to the dissolution of alumina and the evaporation of AlF_3. Bath samples are taken at the beginning, middle, and end of the experiment to corroborate and evaluate the variations of these parameters. Figure 2.2 presents an example of the output of the gravimetric system for the dissolution of a non-porous disc. It can be seen that the dissolution of such a sample is quite monotone and then easy to analyze.

2.3.2 POROUS DISCS

The experimental conditions for the dissolution of porous discs were similar to those of non-porous discs. However, the mass of the samples was lower, around 16 g, due to the porosities, with a similar volume. Another difference was the support of the sample, which was a circular grid, to maintain the integrity of the sample. Since the dissolution mainly occurs from the top (see Alarie et al. [49] and the flow description in Chapter 4), the influence of the support on the flow pattern around the sample is here again supposed negligible. Those samples were designed to see the influence of the porosity on the dissolution behavior of a sample, as presented in Figure 2.3. However, these results were set aside along the way, since physical relationships could be established directly between the powder samples and their results.

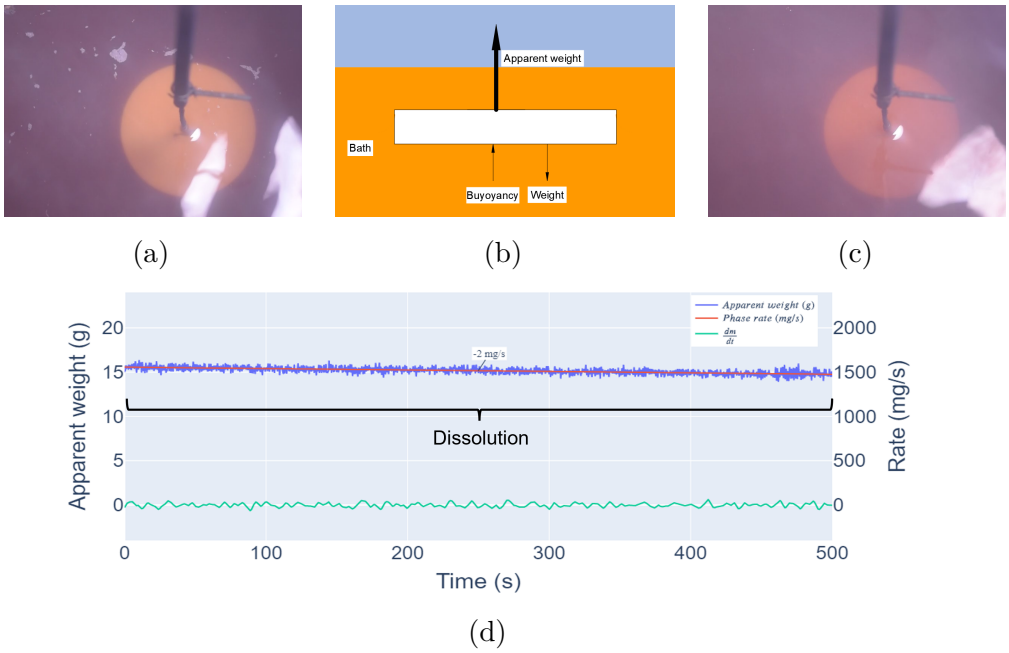

Figure 2.2 : Evolution of the shape and apparent weight of a non-porous disc. (a) sample at the beginning of the test. (b) schematic of the forces acting on the sample. (c) sample at the end of the test. (d) recording of the apparent weight with the identification of known events.

2.3.3 IMMERSED POWDER

The injection of a powder adds much new physics, such as thermal phenomena as well as the phase change of alumina, in addition to the random effects inherent in the use of powder. To be able to compare the results obtained with the first two structures, powder injections were carried out in a metal ring and then submerged to the same depth as the disks, as shown in figure 2.4b. It is also important to note, from figures 2.4a and 2.4c, that the sample now changes shape during the dissolution, since most of the injected mass is dissolved in the time considered. Also, a large part of the infiltration phase occurs before the immersion of the sample, in order to preserve its integrity. Finally, the sample presented here tilted on the support before its complete dissolution and this event is visible in figure 2.4d. Here again, those results were set

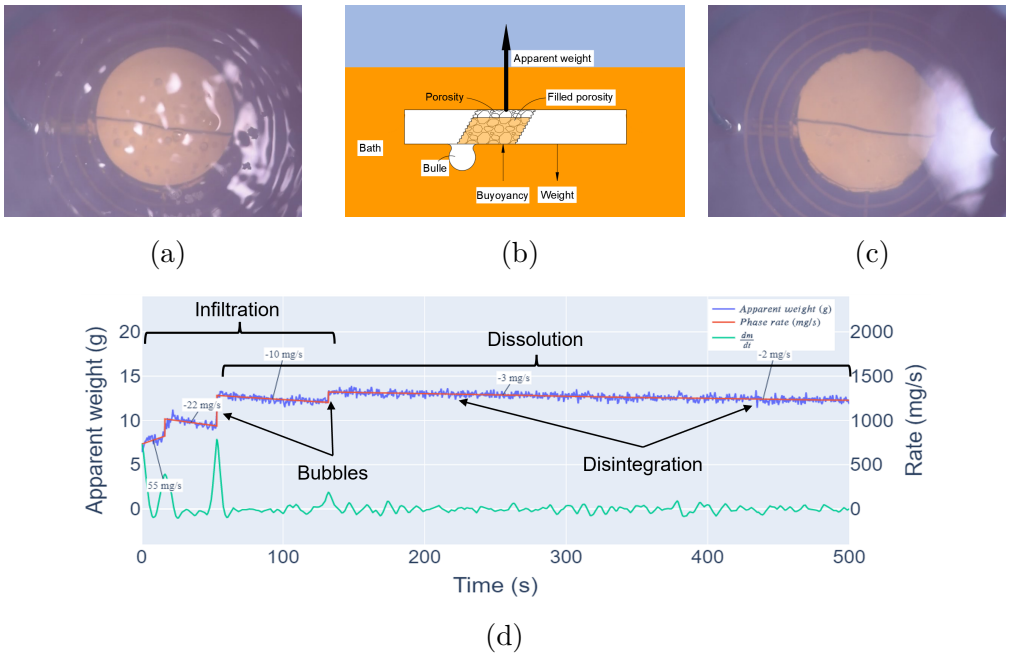

Figure 2.3 : Evolution of the shape and apparent weight of a porous disc. (a) sample at the beginning of the test. (b) schematic of the forces acting on the sample. (c) sample at the end of the test. (d) recording of the apparent weight with the identification of known events.

aside during the analysis, because the link between the non-porous discs and a raft at the bath-air interface was no more needed.

2.4 POWDER CONSTRAINED AT THE SURFACE

Once the transposition of the discs to the powder is understood, it is now possible to add the effects related to the interface, as illustrated by Figure 2.5b. New injections were made, kept on the surface, and constrained with a metal ring in order to have an initial repetitive raft shape. The holder, made of a cross of Nichrome wire with a stainless steel ring, was lowered before the injection. The alumina is then poured with a funnel into the middle of the holder. Alumina then sinter with the holder to allow the

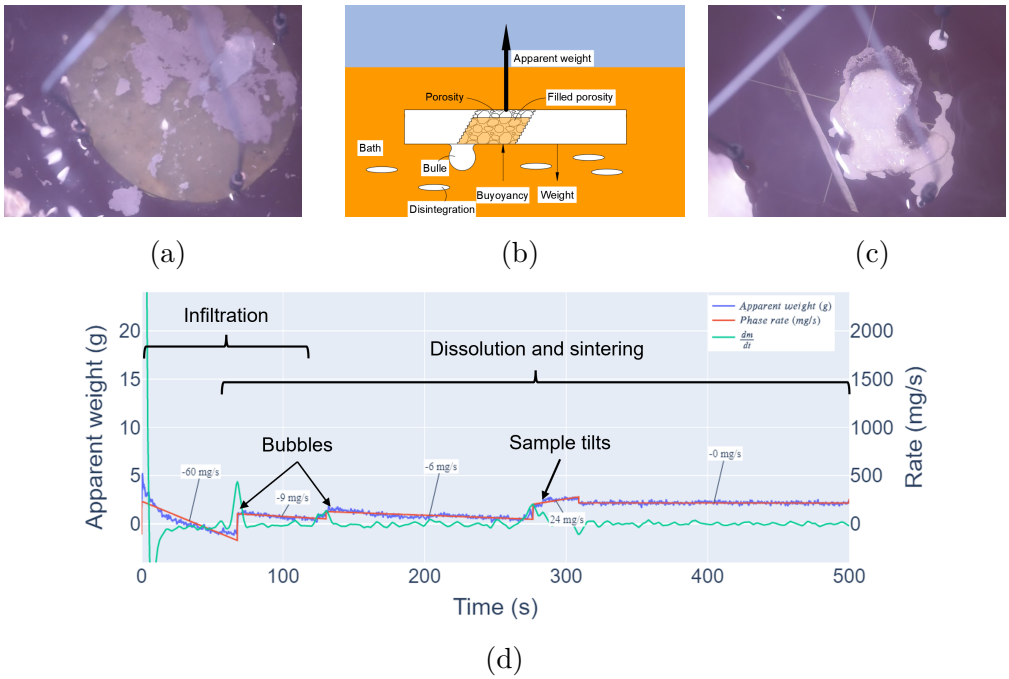

Figure 2.4 : Evolution of the shape and apparent weight of an immersed injection of alumina powder. (a) sample at the beginning of the test. (b) schematic of the forces acting on the sample. (c) sample at the end of the test. (d) recording of the apparent weight with the identification of known events.

measurements. These are the samples with the most variations observed in the recorded curve, as shown by Figure 2.5d, despite a small evolution of the shape, as shown by figures 2.5a and 2.5c. The infiltration phase is important and superimposed on some disintegration in addition to the release of bubbles. Also, it is clear that at about 60 seconds, the density of the sample is such that it sinks and is simply retained on the surface by the support of the device.

2.5 FREE SURFACE POWDER

The previous steps wanted to isolate and understand each of the phenomena found in Figure 2.6d. This figure shows the evolution of the apparent weight of an

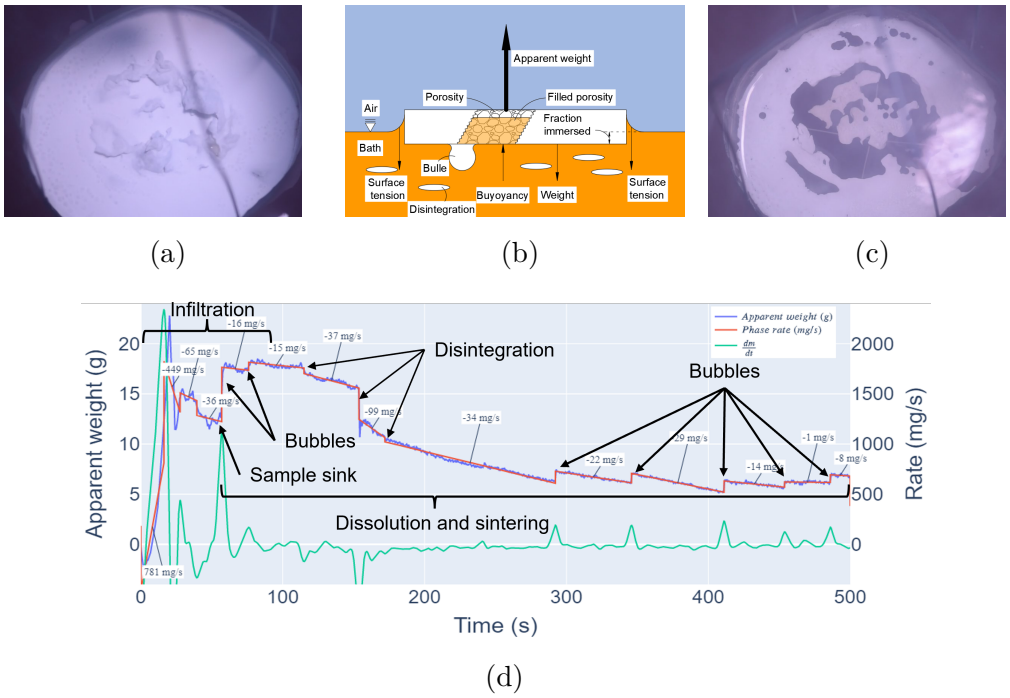

Figure 2.5 : Evolution of the shape and apparent weight of a constrained injection of alumina powder at the surface. (a) sample at the beginning of the test. (b) schematic of the forces acting on the sample. (c) sample at the end of the test. (d) recording of the apparent weight with the identification of known events.

unconstrained alumina raft on the surface of the bath. Figures 2.6a and 2.6c show the evolution of the contact surface between the liquid and the solid during the recording of Figure 2.6d. It can be seen that the raft is not very thick and loses a lot of its surface throughout the experiment. In addition, except for the infiltration phase, the dissolution is much more monotonous than when the powder is constrained. The difference between the thickness of the two types of samples explains this observation. In addition, the dissolution part seems to follow a decreasing exponential curve, consistent with the rate of loss of its surface.

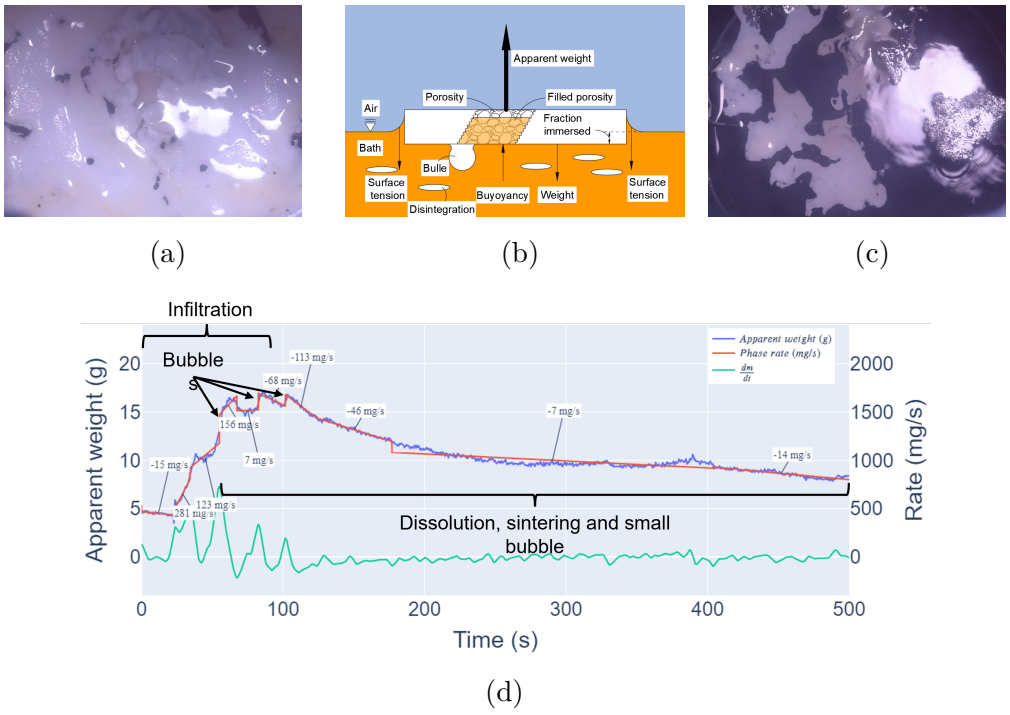

Figure 2.6 : Evolution of the shape and apparent weight of a free surface injection of alumina powder. (a) sample at the beginning of the test. (b) schematic of the forces acting on the sample. (c) sample at the end of the test. (d) recording of the apparent weight with the identification of known events.

2.6 ALUMINA STRUCTURES

Aside from the tests with the gravimetric apparatus, tests on alumina sintering were also performed. These tests involved 40 g of primary alumina poured into 150 mL of bath, with different compositions. The powder and the bath were gradually heated in the setup presented in Figure 2.7, in order to avoid the formation of a solidified bath around the alumina. Once the target temperature was reached and maintained for 15 minutes, the alumina powder was poured into the bath and allowed to cool after a given wetting time.

Figure 2.7 : Experimental setup for the tests on the sintering of alumina

These tests were used to obtain scanning electron microscope images of the microstructures found in a raft. The image obtained allows a deeper understanding of the raft's internal modification over time. Figure 2.8 shows examples of the images obtained with these tests, while complete results will be analyzed in future work. Figure 2.8 presents the evolution of the structure of the alumina when put in contact with cryolite. It is possible to see that the highly porous γ-alumina is transformed in dense α-alumina platelets with larger intragranular porosities. These porosities fill themselves with bath when in contact with the liquid.

Note that there are three kinds of structure encountered throughout these figures :

1. The raft (Figures 2.8a and 2.8b)
2. An alumina grain (Figures 2.8e and 2.8f)
3. A platelet (Figures 2.8c and 2.8d)

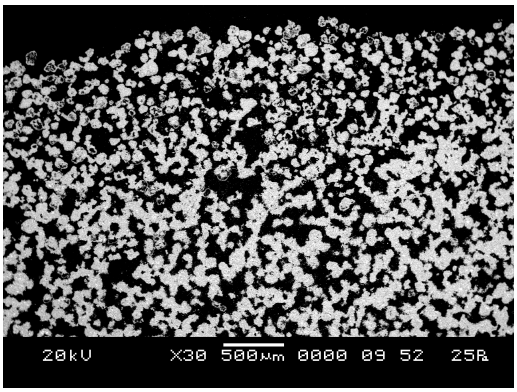

(a)

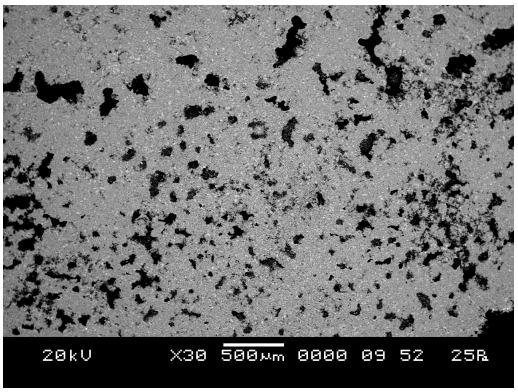

(b)

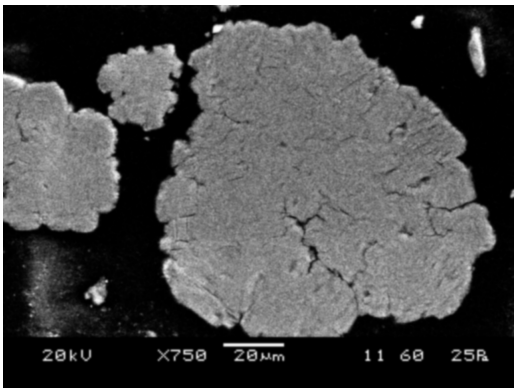

(c)

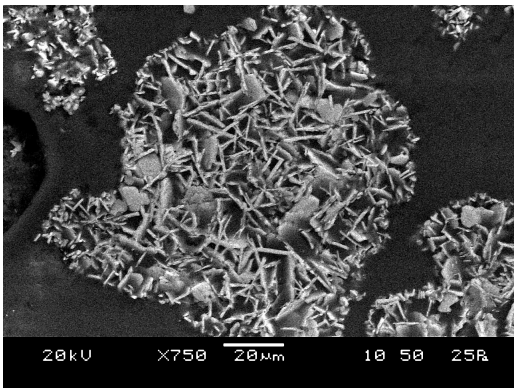

(d)

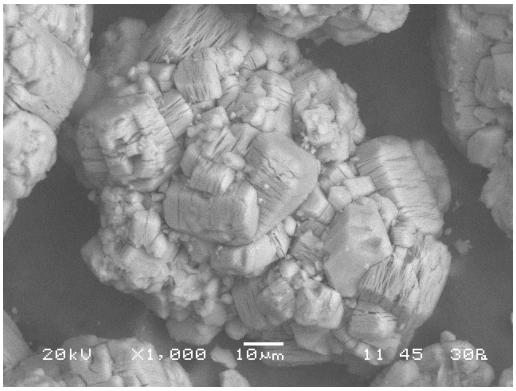

(e)

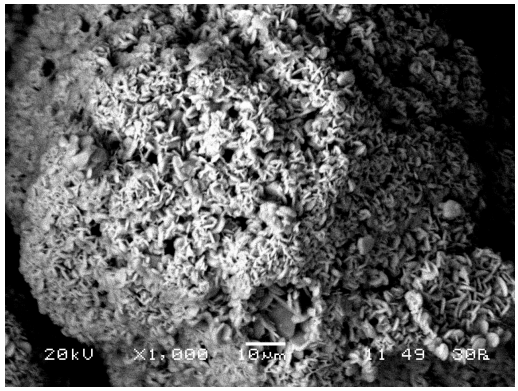

(f)

Figure 2.8 : Alumina transformation. Left: Alumina before contact with the fluoride (liquid or gaseous). Right: Alumina after contact with the liquid (± 2 min). (a-b) Liquid contact, 30x. (c-d) Gaseous contact, 750x. (e-f) Gaseous contact, 1000x.

Each of these structures has its particular composition, mainly due to the filling of their porosity with bath or air, which changes over time. Therefore, it is important to distinguish the properties of the materials, such as alumina and the bath, from the effective properties of a particular structure. This particular distinction is made throughout the text by the use of effective properties. Effective properties represent an equivalent value of a property if the entire structure were composed of a homogeneous material, which is not the case. For example, the effective density of the raft is related to the mass of alumina, bath (solid or liquid), and air inside the volume of the raft. This effective density will change over time as the raft is slowly infiltrated, while that of its component is considered constant (some constituent can see their density change with chemical reactions). The same logic applies to the effective dissolution of a structure, which is considered as the uniform dissolution of the structure as if the structure is completely composed of a homogeneous solid that dissolves through the surface of the structure in contact with the liquid.

REFERENCES

[49] J. Alarie, T. Roger, L. I. Kiss, S. Poncsák, S. Guérard, and J.-F. Bilodeau, "Validation of the gravimetric method to properly follow alumina dissolution in cryolitic bath," in *Light Metals 2020*. Springer, 2020, pp. 680–687.

CHAPTER III
EMPIRICAL PREDICTION OF ALUMINA DISSOLUTION RATE IN A CRYOLITIC MELT: COMPARISON WITH THE EXISTING LITERATURE.

3.1 SYNOPSIS

3.1.1 OBJECTIVES

This article represents a comprehensive analysis of the literature available for alumina dissolution. Its contribution is indirect to the objectives of the thesis and constitutes the basis from which the thesis is built.

3.1.2 SCIENTIFIC CONTRIBUTION

Any scientific work first needs a solid basis built on past work on the subject and the physics involved in the process. This article relates the most important work on the subject of alumina dissolution. Then, a discussion of the main parameters that influence the alumina dissolution is presented. This part shows that alumina dissolution is a very complicated subject with more than 50 possible parameters. A comprehensive analysis of these parameters allows identifying a dozen main parameters involved in the alumina dissolution.

From the literature data available and the experimental work on the non-porous discs, the first model to predict alumina dissolution was built. This model allows comparing the results obtained from the experimental tests with the literature and confirms that the methodology is suitable. The subsequent analysis suggests that the

dissolution of alumina is best studied with the help of the bath properties and the Sherwood number.

Finally, a simple simulation shows how this kind of model can be used to help enhance the control of industrial electrolysis cells. It is easier to compare the output of the model from an industrial point of view, which is well known than to compare it to the only model available in the literature [50]. This simulation integrates the dissolution and consumption of the alumina mass present in the cell with 4 kg of alumina added every 30 seconds. The alumina mass is divided into smaller chunks of 5 g with a dissolution rate determined by equation 3.1. The cell is a 400 kA with current efficiency of 0.9 and 7 000 kg of standard industrial bath (11.5 w% AlF_3, 5.5 w% CaF_2 and 10 °C Superheat) with consumption of alumina rounded from 1.89 kg/kg_{Al} to 2 kg/kg_{Al} to consider impurities.

3.1.3 AUTHORS CONTRIBUTIONS

Work	Contributors
Direction	Prof. László I. Kiss and Prof. Lukas Dion
Original Idea	Prof. László I. Kiss and Thomas Roger
Design of the apparatus	Jonathan Alarie
Construction	Jonathan Alarie and Patrice Paquette
Experimental plan	Jonathan Alarie
Tests	Martin Truchon and Jonathan Alarie
Data mining	Jonathan Alarie
Analysis	Jonathan Alarie
Writing	Jonathan Alarie
Revision	Prof. László I. Kiss and Prof. Lukas Dion
Technical Support	Sébastien Guérard and Jean-François Bilodeau

3.1.4 PUBLICATION

Authors	Jonathan Alarie, László I. Kiss, Lukas Dion, Martin Truchon, Renaud Santerre, Sébastien Guérard and Jean-François Bilodeau
Year	2022
Title	Empirical prediction of alumina dissolution rate in a cryolitic melt: comparison with the existing literature
Journal	TMS Light Metals
Status	Published (Reprint permission available in Appendix A.1)
Date	March 2022

3.1.5 RÉSUMÉ

La dissolution de l'alumine dans la cryolite a fait l'objet de nombreuses publications dans la littérature. Cependant, ces études couvrent un grand intervalle de conditions différentes, souvent présentés dans des formats aussi différents. Afin de comparer ces résultats, un modèle empirique a été développé à partir de données expérimentales obtenues grâce à la méthode gravimétrique sur des disques d'alumine non-poreux. Ce modèle a ensuite été appliqué aux données provenant de la litérature et montre des différences significatives entre les jeux de données. Ces différences sont ensuite décrites et discuté pour en identifier les causes. La plupart des variations observées sont attribuées à trois principaux facteurs qui influence le plus fortement la dissolution. Le premier facteur est la morphologie de l'alumine et sa fraction massique dissoute dans l'électrolyte. Ensuite, les flux massiques et thermiques autour des différents échantillons étudiés sont aussi de première importance. Finalement, l'influence de la fraction massique des additifs dans le bain de cryolite représente aussi un paramètre important pour la dissolution de l'alumine.

3.1.6 NOMENCLATURE

Parameter	Definition
A	Area of contact
D	Diffusivity
$\frac{dw}{dx}$	Mass fraction gradient
g	Gravity constant
Gr	Grashof number
h_m	Convection mass transfer coefficient
L_c	Characteristic length
$\dot{m}$	Mass flow rate
Sc	Schmidt number
Sh	Sherwood number
T	Temperature
w	Mass fraction
Greek letters	**Definition**
Δ	Difference
ν	Kinematic viscosity
ρ	Density
φ	Mass flux
Subscript	**Definition**
∞	Bulk value
i	Value for the component
m	Melt value
ref	Reference value
s	Surface value

EMPIRICAL PREDICTION OF ALUMINA DISSOLUTION RATE IN A CRYOLITIC MELT: COMPARISON WITH THE EXISTING LITERATURE.

Jonathan Alarie[a], László I. Kiss[a], Lukas Dion[a], Martin Truchon[a], Renaud Santerre[b], Sébastien Guérard[c], Jean-François Bilodeau[c]

[a]GRIPS, University of Quebec at Chicoutimi, 555 Boul Universite, Saguenay, G7H 2B1, Quebec, Canada [b]Technical advisor, Retired from Rio Tinto, 1955 Mellon Boulevard, Jonquiere, G7S 4K8, Quebec, Canada [c]Arvida Research and Development Centre, Rio Tinto, 1955 Mellon Boulevard, Jonquiere, G7S 4K8, Quebec, Canada

ABSTRACT

There are numerous studies published in the literature related to alumina dissolution rates in cryolite melts. However, such studies cover a broad range of results given in various formats. A new empirical equation was developed based on the results of an extensive parametric study using the gravimetric method on alumina disks. A comparison between these models shows large differences with the existing literature. The present paper describes and discusses these differences. Most of the variation is caused by three main parameters strongly influencing the alumina dissolution kinetics. First, there is the alumina content and its morphology. Secondly, there is the mass and heat flow around the sample inherent to the experimental methods that were used. Thirdly, the influence of the concentration of the additives in the bath was identified as a strong contributor to explaining the reported differences.

Keywords: Aluminum electrolysis, Alumina dissolution, Cryolite properties

3.2 INTRODUCTION

The control of the alumina distribution in an industrial pot is an everyday challenge. The typical strategy involves a periodic alternation between under and overfeeding cycles respective of basic rules or targets defined by process engineers. Such dynamics allow the operation of the pots in a specific range of alumina concentration that mitigate the apparition of anode effects, or oppositely, avoid estimated high values of alumina mass fractions. In the pursuit towards an ideal process, one could foresee a narrowband of alumina concentration around a desired operation point where the variations between underfeeding and overfeeding would be minimal, or non-existent. Such a scenario could hypothetically lead to a steady-state point of operation for the cell. Such amelioration would lead to better stability of the process, thus a higher production rate and a potential increase in the safety of the plant workers. Practically, to lean towards this desired behavior, a better understanding of the alumina dissolution kinetics is necessary. It is well known that there is a substantial time lag between the injection of alumina powder in the bath and its complete dissolution. Many researchers tried to estimate this time lag, which is an essential component of the transient mass balance of the cells that could lead to the ideal feeding process described previously. This paper summarizes relevant work in this field of study and compares the literature results to research data developed by the principal author with the use of a gravimetric method. A mathematical model is then extracted from the summation of these data to predict the dissolution rate of alumina in molten cryolite. Finally, a practical application for the model is presented by simulating transient variations in an aluminum electrolysis cell.

3.2.1 LITERATURE REVIEW

Before the analysis, it is necessary to present the published studies that were considered to build the “alumina dissolution database ”.

One of the well-known works is from Gerlach et al. [51] who used an experimental setup built from a conical crucible with about 150 g of bath stirred with a propeller to dissolve pressed tablets. They found the effects of the chemical composition of the bath and crystalline structure on the dissolution rate of alumina.

Jain et al. [52] used the voltammetric method to describe the dissolution of 1 to 2.5 w% of alumina powder injected in cryolite. Their study aimed to compare the dissolution of different smelter-grade alumina. They also tried to characterize the effect of the bath superheat on the dissolution of alumina by increasing the bath temperature and use of different chemistry. The use of time series in this study makes the results more tedious to add to this work. So, only the linear portion of the curve was used to compute an average dissolution rate found in these tests.

Bagshaw et al. [53] used a voltammetric method to follow the alumina mass fraction in the melt. They injected different alumina powders in the same bath composition. The parameters they studied are the properties of alumina, namely the BET surface and the crystallographic structure of alumina.

Isaeva et al. [54] used a visual method to determine the dissolution rate of batches of 0.5 w% of alumina powder. They tried to study the effects of the alumina content of the melt and the properties of alumina on the dissolution rate. One of the main differences with the present work is that the chemical composition of their melt was pretty much the same from one test to another.

Lubyová et al. [55, 56] used a gravimetric method of samples of the bath to determine the alumina content of melts with natural convection. With this method, they tried to determine the influence of the additives, including AlF_3, LiF, and KF as well as alumina content, over the dissolution rate of alumina powder.

Vasyunina et al. [57] used a combination of visual and voltammetric methods to measure the dissolution rate of alumina powder. They used different bath chemistry without agitation.

Yang et al. [58, 59] visualized the dissolution of alumina with different properties in a few bath compositions. They published a few papers on the subject, but only one is retained here, since a large portion of their work covers the use of LiF, unlike the majority of the authors considered here.

Frazer et al. [60] used the rotating disc method to study the dissolution of the alumina in low-temperature melt. Despite the high content in AlF_3 in this melt that can lead to a lower dissolution rate, these data were still included in this work.

Gylver [61] studied the mass of rafts over time. He injected alumina powder into the melt and retrieved them at different times.

3.3 METHOD

The work presented here comes from multiple sets of data divided into two categories. First, data was borrowed from the literature as described in the previous section. Secondly, a set of experimental data obtained using a gravimetric method [62] is also considered for a comparison with the data from the literature. Using this complete dataset, a linear multifactor regression model using key drivers for the alumina dissolution rate has been developed. To build the data set from the literature, a dozen

publications were selected for the details of the method and parameters used to study the alumina dissolution. From the pieces of information in the papers, as many as 50 different parameters influencing the dissolution rate were identified. In the post-treatment of this database, redundant indicators were excluded (e.g., bath ratio vs. cryolite ratio) while other parameters that were not sufficiently described from one author to another had to be discarded. Overall, the relevant list of indicators from the "alumina dissolution database" has been reduced to a dozen parameters, listed as follows:

Time: The period between the injection of the alumina sample and the measured information. As the infiltration and dissolution of the alumina sample occur, the area of contact between the solid and the liquid will change and thus the dissolution rate. So, powder injection will see their dissolution rate change over time, but with non-linear behavior. It is indeed due to the agglomeration behavior of the powder injected in the bath that reduces the area of contact between the solid and the liquid. Few authors, like Jain et al. [52], published time series data to present this behavior when injecting alumina powder into the bath. Unfortunately, this kind of data was too uncommon among the papers cited in this work to properly consider the time parameter in the linear regression model.

Measurement method: The method used to measure the alumina dissolution such as the voltammetry method, the gravimetric method, or bath sample analysis. It also includes the frequency of the measurement which generally considers either complete time series or punctual measurements at 75 % or 100 % of the complete dissolution. The measurement technique can influence the measured value of the dissolution rate as the uncertainty of a method can differ from one method to another. Different measurement methods also give different outputs, such as alumina content, dissolution rate, or mass loss from the sample. In this work, the output was standardized as dissolution rates.

Also, with the assumption that the uncertainty of published data is small, there is no need to distinguish the method used to build the model.

Nature of the alumina samples: Alumina in the form of a powder, a pressed tablet, or a sintered disc was used in the different studies. The behavior of a powder is very different from that of a sintered disc. Therefore, the dissolution rate will be impacted. To tackle this behavior, a numeric categorical level has been suggested. However, preliminary results demonstrated that categorical levels were inadequate to properly represent the behavior of this indicator using linear regression.

BET: The specific surface of an alumina sample is dependent on its porosity. A larger porosity let presume a larger surface of contact with the liquid. All specific surfaces in the literature were assumed to have been determined by the BET method. However, this parameter was not described sufficiently by the authors considered. The area of contact between the liquid and the solid is of first importance to adequately scale results from the different masses of samples.

Agitation: The level of agitation of the electrolyte such as natural convection, stirring, bubbling, or the use of a rotating disc was registered. The convection around a dissolving solid is of first importance in the mass transfer process. Stronger convection makes dissolution easier. Since it is very difficult to quantify, a numeric categorical level was selected for the natural and forced convection as well as for the bubbling and rotating discs. Unless otherwise specified, natural convection applies for a test. However, preliminary results demonstrated that categorical levels were inadequate to properly represent the behavior of this indicator using linear regression.

Additives (AlF_3, CaF_2, LiF): They represent the mass fraction of each additive. A higher mass fraction of additives in the electrolyte leads to a weakened ability of the

bath to dissolve alumina. They also have a strong effect on the properties of the bath such as the liquidus temperature, the alumina solubility, viscosity, and density. However, the LiF mass fraction was considered only by a few authors and cannot be retained as a useful parameter in this work. Surprisingly, the CaF_2 parameter was also revealed to be insignificant in this work, since most of the authors used similar CaF_2 content.

α-alumina: The mass fraction of α-alumina in the alumina injected. When this information was unavailable, a mass fraction of 1 w% was assumed in the alumina sample [63]. The alumina can take many crystalline forms. The most stable of them is the α-alumina phase. This structure is more difficult to dissolve than the others, generally designated as γ-alumina phases. So, the content of the α-alumina phase is expected to decrease the dissolution rate of an alumina sample. Unfortunately, the variation of this parameter in the literature data was often too small when studied at all.

Al_2O_3: Initial and final mass fraction of alumina in the melt. The initial alumina content will decrease the dissolution rate of a sample as it is a key component of the dissolution rate kinetics. In the rare cases where it was unspecified by the author, the initial alumina content is assumed to be 1 w%

Liquidus: The liquidus temperature as computed from the formula of Solheim et al. [64]. Along with the bath temperature, the liquidus is used to determine the superheat. The superheat is considered one of the main parameters of the dissolution process because it combines the effect of the bath temperature and the chemistry of the electrolyte.

Bath Temperature: Mean temperature of the melt during the test. When unavailable, the liquidus temperature with an assumed superheat of 10 °C was used. The bath

temperature provides the required energy to heat the alumina and fuel the dissolution process.

Solubility: The alumina solubility as computed from the formula of Skybakmoen et al. [65]. The solubility indicates how much alumina an electrolyte can contain. Along with the alumina content, it represents the main driving force of the dissolution.

Dissolution Rate: The dissolution of a given mass of alumina divided by the time needed to dissolve it. The mass dissolved during the test can be generally 75 % or 100 % of the mass injected. This is the target parameter that is sought and predicted with the linear regression.

These parameters represent the ones that were somehow consistent from one author to another. The use of these parameters was compared by building different models with and without them, which is consistent with the physics of the phenomena. The correlation coefficients of these models were compared between themselves, while the significance of the parameters was kept consistent. This means that the p-value of every parameter is not greater than 0.05, which represents less than a 5 % chance that the null hypothesis can apply to that parameter. Also, simpler models were favored over the more complex ones to ensure the significance of all parameters. The Akaike and Bayesian information criteria were used to discriminate complex models when needed and ultimately prevent any form of overfitting. Also, some authors, such as Haverkamp [66], studied the effect of surface phenomena on dissolution. Since the main parameters that they studied are not considered by most of the authors, their inclusion resulted in large deviations from the model presented here and has been put aside. In the end, only three parameters were kept and used to predict the alumina dissolution rate.

3.4 RESULTS

3.4.1 DESCRIPTION OF THE MODEL

As discussed previously, the resulting model was developed with three input parameters: the mass fraction of aluminum fluoride and alumina, as well as the bath temperature. Figure 3.1 shows the accuracy of the correlation between the data and the model. Also, the model is given by the equation 3.1, normalized for an average injection in the alumina dissolution database ($\dot{m}_ref$), from $\mathrm{mg/g_{Al_2O_3}{\cdot}s}$ to dimensionless dissolution rate by the predicted rate at a median scenario.

$$\begin{aligned} \dot{m}\left[\frac{(mg/g_{Al_2O_3}\cdot s)_i}{(mg/g_{Al_2O_3}\cdot s)_{ref}}\right] = \\ -3.41\times10^{-2}\cdot AlF_3\,[w\%] \\ -2.89\times10^{-1}\cdot Al_2O_3\,[w\%] \\ +2.61\times10^{-3}\cdot T\,[^\circ C] \end{aligned} \tag{3.1}$$

From Figure 3.1, it can be seen that even a small number of input parameters can provide a good estimation of the alumina dissolution rate. The three parameters used in the model can explain 83.8 % of the variance between the data from all authors united. This also means that the addition of any other parameters to the model can only have a limited effect since only 16.2 % of the variance is left to describe. The nature of these parameters is also very important because they are commonly described in the industry as factors with a significant influence on the dissolution rate within an electrolysis cell. For improved prediction accuracy, an important requirement here is that all the parameters in the regression should be independent. This naturally leads to the use

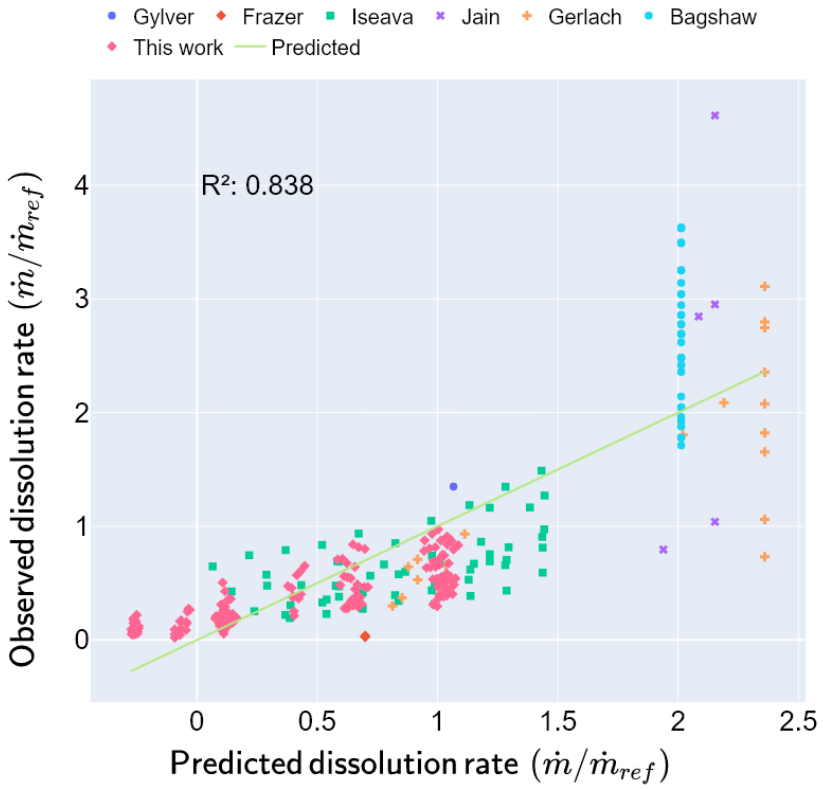

Figure 3.1 : Correlation between the predicted values of the model (line) with the observed values by each author (markers).

of chemical additives and the bath temperature. These parameters drive the liquidus temperature and alumina solubility of the melt as well as its density and viscosity. So, the use of any of these bath properties will be redundant and provoke undesirable effects in the mathematical regression process because of the collinearity of the inputs, unless these properties describe the interactions or non-linearity of the chemical composition of the bath. Surprisingly, the agitation parameter does not seem to have a strong influence on the model built. It is expected that the flow around the sample will greatly affect the dissolution rate. However, to include it in the model without an extensive comprehension of the convection in each experimental setup, a numerical categorical parameter was used. So, to ensure the significance of this parameter, it is necessary

to create a mapping of these categories that fit with the influence of the flow on the dissolution. In other words, one needs to master the effect of the convection around the sample in each experimental setup to set an appropriate level for each of them. This was beyond the scope of this work and led us to the rejection of this parameter.

3.4.2 SIGNIFICANCE OF THE MODEL

From Figure 3.1, it can also be seen that the model performs well for the entire dataset. However, data from some authors seem to show large variations compared to the established model. This can be easily explained by two phenomena. The first one is inherent to the physical nature of each respective study. Many authors studied different parameters than the inputs considered for the model presented here; parameters such as the alumina crystalline phase or the specific surface. Therefore, as the three inputs of this regression remain constant, the predicted behavior will remain the same even if the corresponding measurement shows differences in dissolution rates. This will lead to vertical distribution of their data points compared to the prediction. This vertical behavior can be seen particularly when we apply the model to the data from Gerlach et al. [51] and Bagshaw et al. [53]. The second phenomenon is mathematical. As was said earlier, the different authors did not study the effect of the same parameters in their respective designs of experiments. So, if a parameter used in the present model was not varied by an author, that parameter is not relevant to his data. This led to a loss of accuracy concerning the scoring of these data on the model presented here. A good example here is the data from Isaeva et al. [54], her analysis concerns mainly the fraction of fine particles, the α-alumina phase content, and the LOI of the alumina. Since the variation of the alumina mass fraction was a part of her work, her data were included here. However, the direct application of the present model on her data points

cannot tackle all the behavior of her alumina samples. Due to the inherent properties of the dataset considered in the development of the alumina dissolution model, there are limits to the validity of its utilization. The extremes of the data used to build the model are described in Table 3.1 and the model should be used exclusively within this domain to avoid extrapolating outside its range of validity.

Table 3.1 : Validity range of the model

Parameter	Minimum	Maximum
AlF_3 (w%)	0	36.9
CaF_2 (w%)	0	9.9
Al_2O_3 (w%)	1	8
Temperature (°C)	750	1015
Powder mass (g)	1	25

3.4.3 BATH PROPERTIES

The dissolution process is controlled by the diffusion of alumina in the laminar sublayer along the solid surface, according to Fick's first law (eq. 3.2) [67]. Its practical use is limited by the need to solve the system of mass, momentum, and energy balance equations to find the concentration gradient at the surface. Introducing the h_m mass transfer coefficient and the difference of the saturation and bulk mass fractions as driving forces, the dissolution rate can be calculated by the simple expression (eq. 3.3). Most practical calculations of mass transfer in solid-liquid systems are based on this approach, frequently using a representation in dimensionless form. The dimensionless parameter Sh (Sherwood number) that is proportional to h_m is expressed as a function of other groups describing the effect of flow parameters and the influence of material properties like the Reynolds, Grashof, and Schmidt numbers. The concrete form of this correlation

is determined by measurements and sometimes by mathematical modeling. An empirical formula describing mass transfer in the case of natural convection is given in (eq. 3.5 [67]).

At this point, it is worth mentioning that the correlation of eq. 3.5 was assumed to fit the case of a raft on the surface of the bath (hypothesis one). With a constant characteristic length of the sample (hypothesis two) and the diffusion coefficient of the alumina in the cryolite also constant (hypothesis three), these three hypotheses serve as a comparison base for the following explanation. So, the Sherwood number can also be approximated with empirical relations from the flow conditions (eq. 3.5), described by the Grashof number (eq. 3.6) and by the Schmidt number (eq. 3.7). The viscosity and the density of the fluid should be of first importance in these calculations. These two properties have been well described by Hertzberg et al. [68] and Kvande in Thonstad [69] using the bath chemistry and the superheat as input to estimate the resulting properties of the bath. To adequately correlate the effect of the bath chemistry with the dissolution rate, all four parameters used in this model and their effect on the bath properties are summarized in figures 3.2 to 3.4. These figures show the relative influence of a single parameter on the bath properties and the Sherwood number. However, it was hypothesized that all other parameters are kept constant around a typical process value. Additionally, a diffusion coefficient of $1x10^{-9}$ m^2/s [70] and a characteristic length of 10 cm were considered. The characteristic length corresponds to the area-to-perimeter ratio of a raft with 40 cm diameter [67], thus resulting in the value of its diameter divided by four. A final hypothesis considers that the raft behaves like a flat plate over the cryolite melt.

$$\varphi = -\rho D \frac{dw}{dx} \left[\frac{kg}{m^2 s} \right] \tag{3.2}$$

$$\varphi = \frac{\dot{m}}{A} = h_m \rho (w_s - w_\infty) \left[\frac{kg}{m^2 s} \right] \tag{3.3}$$

$$Sh = \frac{h_m L_c}{D} \tag{3.4}$$

$$Sh = 0.27(Gr \cdot Sc)^{1/4} \tag{3.5}$$

$$Gr = \frac{g \Delta \rho L_c^3}{\rho_m \nu^2} \tag{3.6}$$

$$Sc = \frac{\nu}{D} \tag{3.7}$$

From Figure 3.2 it can be seen that the effect of the CaF_2 on the bath properties is limited. This led to a slight reduction of the Sherwood number, from 27.6 to 27.2, and therefore the CaF_2 has a lesser influence on the dissolution of alumina, as depicted in the model presented above. The stronger effect of this parameter comes from the diminution of the solubility of alumina, which lowers the driving force of the alumina dissolution. At this point, it is necessary to remember that the dissolution rate found with Fick's law and the Sherwood number is greatly dependent on the hypothesis of the characteristic length and the diffusion coefficient. If their ratio is very high, such as when the diffusion coefficient is as low as $1x10^{-9}$ m^2/s, a small variation of the Sherwood number can lead to a great difference in the dissolution rate, as depicted in figures 3.2 to 3.4

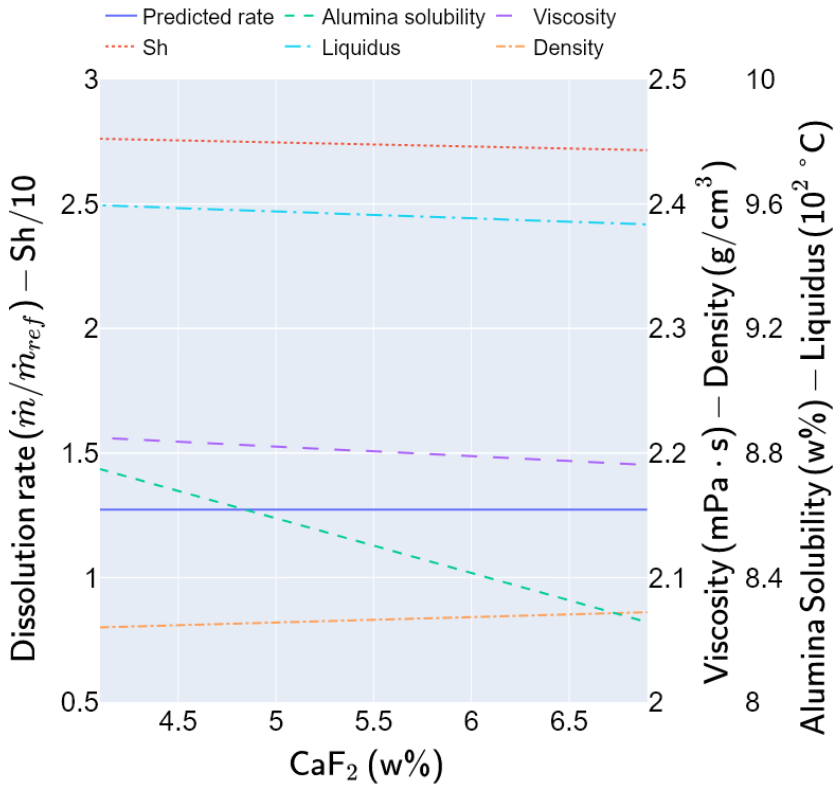

Figure 3.2 : Effect of CaF_2 on the bath properties and the predicted dissolution rate

For the AlF_3 content, shown in Figure 3.3, it can be seen that its effect on the bath properties is important except for the Sherwood number which remains fairly constant. It is worth mentioning that the AlF_3 content greatly decreases the viscosity of the melt, leading to a slight increase in the Sherwood number from 27.4 to 27.5. Similar to CaF_2, the main influence of the AlF_3 comes from the change in the alumina solubility of the melt. Together, the augmentation of the Sherwood number and the diminution of the alumina solubility leads to a lesser influence of the AlF_3 than the alumina or the temperature effect. One can also easily figure out the direct effect of the AlF_3 parameters on the liquidus temperature [65]. While the CaF_2 decreases the liquidus temperature by 2.1 °C/w%, the liquidus decreases by 4.7 °C/w% for the AlF_3

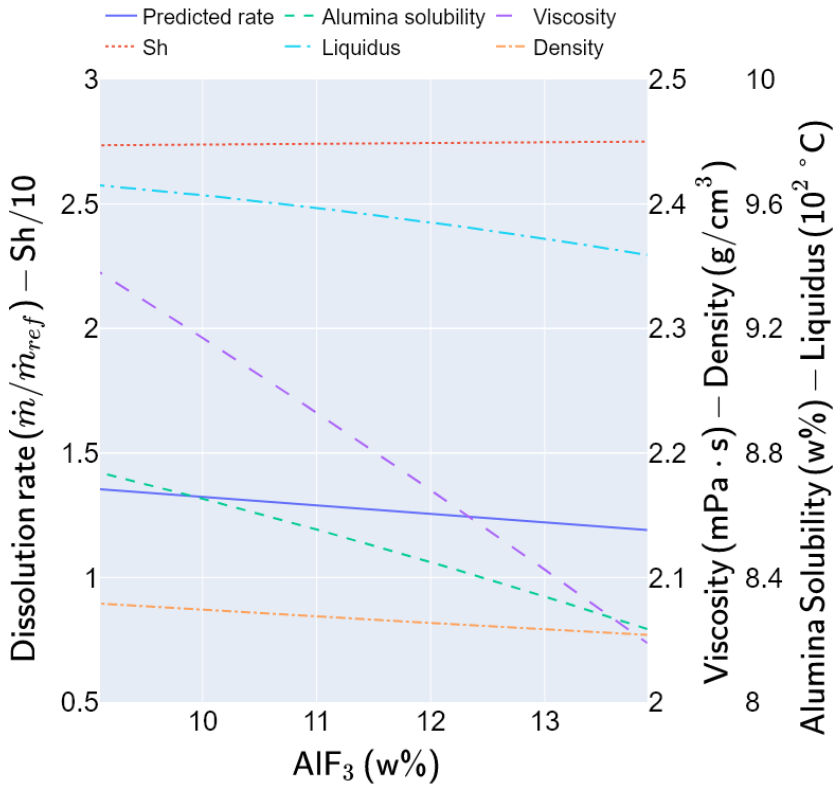

Figure 3.3 : Effect of AlF_3 on the bath properties and the predicted dissolution rate

content. This causes, at a constant temperature of the bath, an increase of the superheat much more important with the AlF_3 content, which has a known beneficial effect on the alumina dissolution rate.

The strongest parameter affecting the bath properties is the bath temperature as presented in Figure 3.4. It also has a strong influence on the viscosity, which leads to an increase in the Sherwood number, from 26.5 to 28.1. In addition to a positive effect on alumina solubility, it is the only parameter that affects positively the dissolution rate as the value increases.

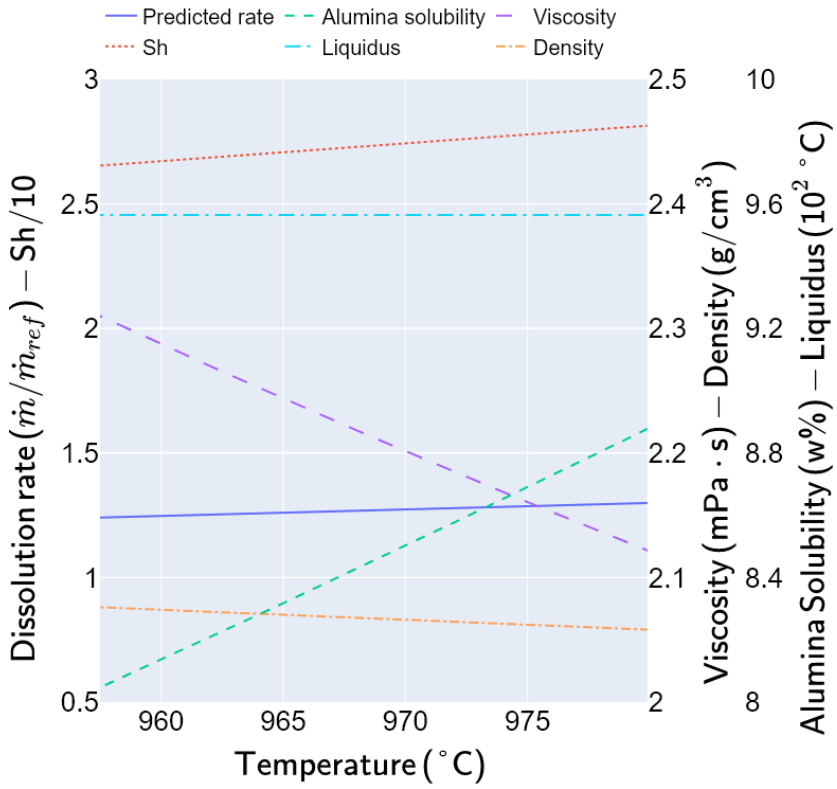

Figure 3.4 : Effect of the bath temperature on the bath properties and the predicted dissolution rate

From Figure 3.4, it can be seen that the dissolution rate is only lightly correlated with the alumina solubility limit. This is in accordance with the previous observations from Johnson [71], Hu et al. [72] and Yang et al. [58], demonstrating that there are slight chemical modifications of the melt when the alumina concentration reaches over 4 w%. That is to say that as it remains below 4 w% in alumina, the difference in alumina concentration between the melt and the alumina surface isn't the limiting factor for the dissolution process.

Finally, from Figure 3.5, a non-linear change in the cryolite melt properties can be seen as the alumina content increases beyond 3 w%. In fact, from 1 w% to 3 w%, only

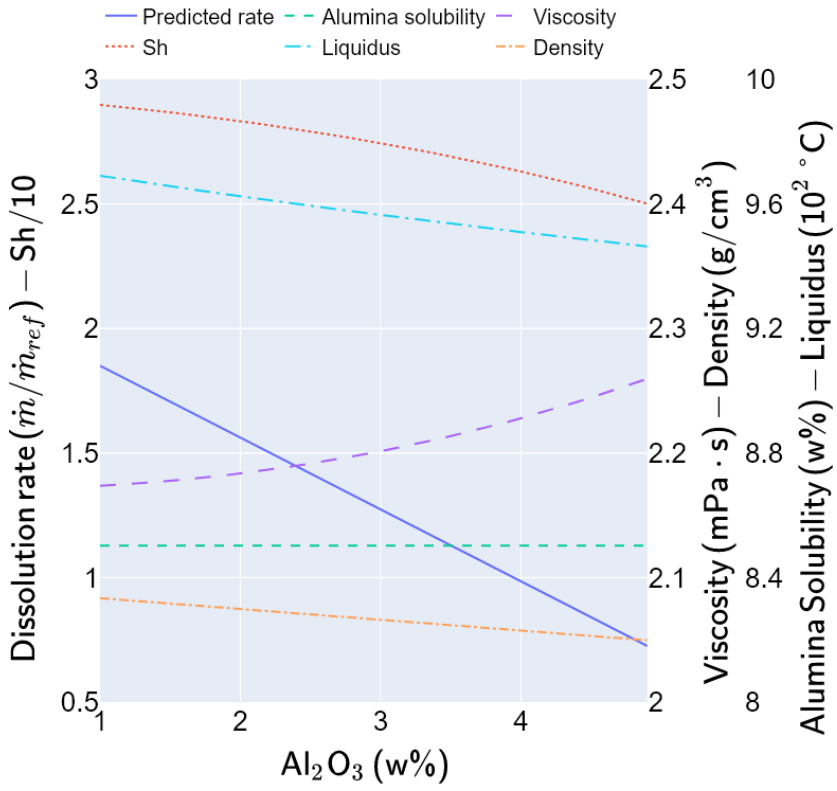

Figure 3.5 : Effect of Al_2O_3 on the bath properties and the predicted dissolution rate

slight changes are noticeable in the properties of the bath. However, starting from 3 w%, the viscosity increases more and more rapidly, which leads to a proportional decrease in the Sherwood number. Nonetheless, this behavior doesn't appear on the predicted dissolution rate, a behavior intrinsic to a linear model. It is unsurprising to observe that the change in the alumina mass fraction from the melt drives the dissolution rate. Even the decrease in the liquidus temperature is insufficient to counter the effect of this driving force.

3.4.4 MODEL EXAMPLE

In a context where we can adequately estimate the chemistry of the bath and its temperature, it is possible to predict the dissolution rate of an alumina sample at any given time after its injection. Accordingly, the relationship between the dissolution rate and the bath chemistry presented here can be used to follow the alumina mass fraction within the electrolyte through time. Another advantage of the proposed model is that the mass fraction of the additives (AlF_3 and CaF_2) in an electrolysis cell can be easily measured and are somehow stable over a relatively longer period in comparison to the alumina concentration. Daily chemical analysis and temperature measurement of the bath, as performed by some smelters, would be enough to roughly keep track of the parameters needed for the model. Therefore, starting from a specific moment in the alumina feeding process, e.g., after a purge tracking, it would be possible to keep track of the transient alumina fluctuations in the electrolysis cell.

A simplified example is presented which considers alumina injections of 4 kg. However, the scaling of the model from its validity range to an industrial size requires an extended knowledge of the contact area between the solid and the liquid. The behavior of rafts in the industrial cells is also important and was studied by some authors [73, 74, 75]. So, the simple application of the model is a simplification of the real phenomena, outside the validity range of the model, and cannot be taken as the true behavior of a raft. These rafts are injected in a typical range of compositions for an industrial bath with a starting alumina content of 2 w%. These conditions presume that the pot is at the end of an underfeeding sequence, where no alumina is left to dissolve in the cell. These injections occur in an electrolysis cell (CE = 0.9, 400 kA) every 30 seconds as described by Haupin [76] and Welch in Grjotheim [77]. Calculations are made every second and the dissolution rate computed depends on the conditions of the bath at the last injection

and applies to the number of rafts not dissolved. Figure 3.6 shows the output that can produce such a kind of simple simulation.

In this graph, you can see that the overfeeding sequence is initialized with an injection at t = 0, which leads to a dissolution rate of 3.10 mg/g·s of the raft. After 30 seconds, a second mass of 4 kg is added to the bath. The dissolution rate is then revised and increases to 3.12 mg/g·s, due to the pot consumption of alumina. Since the first mass isn't completely dissolved, the new dissolution rate is considered for all remaining rafts. The augmentation of the mass of alumina increases the total dissolution rate of alumina and lowers the decrease of the alumina mass fraction in the cell. The dissolution of the alumina decreases the number of rafts in the pot, so the change in the alumina mass fraction between each injection is not exactly linear. By this time, the mass fraction of alumina dissolved in the electrolyte dropped from 2 w% to 1.97 w%. This mechanism continues further to attain the increase of the alumina content in the bath after the seventh injection. Each injection thereafter will see the dissolution rate decrease and the alumina content increase.

It is interesting to see that a time lag is present between the start of the overfeeding sequence and the end of the alumina content decrease. It is then important to carefully choose the moment to begin the overfeeding sequence to avoid low alumina content, which can lead to an anode effect. The model presented here can help to calculate this time lag and ensure better stability of the pot. Ultimately, by adjusting the parameters within this simulation, it is possible to find an optimal point of operation for a given electrolysis cell.

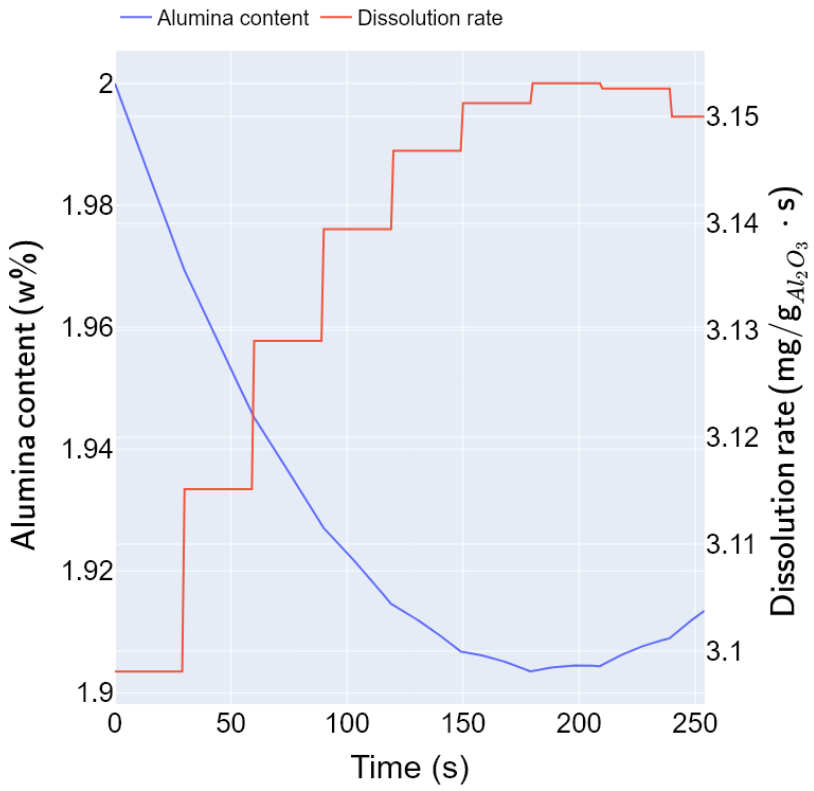

Figure 3.6 : Simulation of successive injections in an industrial bath.

3.5 CONCLUSION

Data from the literature and the gravimetric method have been used to build a linear model predicting the dissolution rate of alumina in a cryolite melt. The model created indicates good agreement between the data from the literature and the experimental work of the author. Using an alumina dissolution database, it appears that three main parameters are adequate to develop a linear regression model predicting the dissolution rate of alumina. These parameters are the mass fractions of AlF_3 and Al_2O_3, as well as the bath temperature. The additives influence the dissolution rate either by influencing the alumina solubility or changing the bath properties leading to changes in the Sherwood number, and thus the dissolution behavior of the alumina.

Furthermore, the bath temperature influences both the solubility of alumina and the Sherwood number to amplify the dissolution.

Using the model built from these three parameters, it is possible to predict the alumina dissolution rate of an alumina sample injected in the bath. This information is of great interest when applied to a simulation of a pot. Even if the actual implementation of this tool is inherent to some practical industrial challenges, the simulation shows that the dissolution rate given by the model could help to attune the time between the injections in an electrolysis cell.

3.6 ACKNOWLEDGMENTS

The authors express their thanks to the Natural Sciences and Engineering Research Council (NSERC) of Canada, Rio Tinto Aluminum, and the Fonds de recherche du Québec—Nature et Technologies, by the intermediary of doctoral scholarship, and of the Aluminum Research Centre REGAL, for their financial and technical support in this project.

REFERENCES

[50] R. G. Haverkamp and B. J. Welch, "Modelling the dissolution of alumina powder in cryolite," *Chemical Engineering and Processing: Process Intensification*, vol. 37, no. 2, pp. 177–187, 1998.

[51] J. Gerlach, U. Hennig, and K. Kern, "The dissolution of aluminum oxide in cryolite melts," *Metallurgical and Materials Transactions B*, vol. 6, no. 1, pp. 83–86, 1975.

[52] R. Jain, S. Tricklebank, B. Welch, and D. Williams, "Interaction of aluminas with aluminum smelting electrolytes," *Light Metals 1983*, pp. 609–622, 1983.

[53] A. Bagshaw and B. Welch, "The influence of alumina properties on its dissolution in smelting electrolyte," in *Essential Readings in Light Metals*. Springer, 2016, pp. 783–787.

[54] L. A. Isaeva, A. B. Braslavskii, and P. V. Polyakov, "Effect of the content of the alpha-phase and granulometric composition on the dissolution rate of alumina in cryolite-alumina melts," *Russian Journal of Non-Ferrous Metals*, vol. 50, no. 6, pp. 600–605, 2009.

[55] Z. Lubyova, P. Fellner, and J. Gabcova, "Solubility and rate of dissolution of alumina in cryolite-based alf3-rich melts with additions of lif, caf2, and mgf2," *Chemical Papers*, vol. 47, no. 4, pp. 218–220, 1993.

[56] Z. Lubyová and V. Danek, "Control mechanism for alumina dissolution in cryolite melts," *Chemical Papers*, vol. 49, no. 2, pp. 59–63, 1995.

[57] N. V. Vasyunina, I. P. Vasyunina, Y. G. Mikhalev, and A. M. Vinogradov, "The solubility and dissolution rate of alumina in acidic cryolite aluminous melts," *Russian Journal of Non-Ferrous Metals*, vol. 50, no. 4, pp. 338–342, 2009.

[58] Y. Yang, B. Gao, Z. Wang, Z. Shi, and X. Hu, "Effect of physiochemical properties and bath chemistry on alumina dissolution rate in cryolite electrolyte," *JOM*, vol. 67, no. 5, pp. 973–983, 2015.

[59] Y. Yang, Y. Li, Y. Huang, B. Gao, X. Hu, Z. Wang, W. Tao, F. Liu, Z. Shi, and J. Yu,

"Formation and dissolution of crust upon alumina addition into cryolite electrolyte (ii)," *JOM*, vol. 71, no. 2, pp. 485–491, 2019.

[60] E. J. Frazer and J. Thonstad, "Alumina solubility and diffusion coefficient of the dissolved alumina species in low-temperature fluoride electrolytes," *Metallurgical and Materials Transactions B*, vol. 41, no. 3, pp. 543–548, 2010.

[61] S. E. Gylver, "Alumina dissolution in cryolite melts-formation and behavior of rafts," Ph.D. dissertation, NTNU, 2018.

[62] J. Alarie, L. I. Kiss, S. Poncsák, R. Santerre, S. Guérard, and J. F. Bilodeau, "Influence of additives on alumina dissolution in superheated cryolite melts." in *TMS 2021*. Springer, 2021, pp. 533–540.

[63] A. N. Bagshaw, *The Aluminium Story - Bauxite To Alumina: The Bayer Process*, 2017. [Online]. Available: https://nzic.org.nz/app/uploads/2018/09/Bauxite-to-Alumina-Book-2018.pdf

[64] A. Solheim, S. Rolseth, E. Skybakmoen, L. Støen, Å. Sterten, and T. Støre, "Liquidus temperatures for primary crystallization of cryolite in molten salt systems of interest for aluminum electrolysis," *Metallurgical and Materials Transactions B*, vol. 27, no. 5, p. 739, 1996.

[65] E. Skybakmoen, A. Solheim, and Å. Sterten, "Alumina solubility in molten salt systems of interest for aluminum electrolysis and related phase diagram data," *Metallurgical and materials transactions B*, vol. 28, no. 1, pp. 81–86, 1997.

[66] R. Haverkamp, B. Welch, and J. Metson, "The influence of fluorination on the dissolution rate of alumina in smelter electrolyte," in *Light Metals - Warrendale*, 1994, pp. 365–365.

[67] Y. A. Cengel and A. J. Ghajar, *Heat and mass transfer : fundamentals & applications*, 5th ed. New York, N.Y.: McGraw-Hill Education, 2015.

[68] T. Hertzberg, K. Tørklep, and H. Øye, "Viscosity of molten naf-alf3-al2o3-caf2 mixtures: Selecting and fitting models in a complex system," in *Essential Readings*

in Light Metals. Springer, 1980, pp. 19–24.

[69] J. Thonstad, *Aluminium electrolysis : fundamentals of the Hall-Héroult process*, 3rd ed. Düsseldorf: Aluminium-Verlag, 2001.

[70] A. Solheim and E. Skybakmoen, "Mass-and heat transfer during dissolution of alumina," in *Light Metals 2020*. Springer, 2020, pp. 664–671.

[71] A. R. Johnson, "Alumina crusting and dissolution in molten electrolyte," *Journal of Metals*, vol. 34, no. 3, pp. 63–68, 1982.

[72] X.-W. Hu, J.-Y. Qu, B.-L. Gao, Z.-N. Shi, F.-G. Liu, and Z.-W. Wang, "Raman spectroscopy and ionic structure of na sub (3 alf) sub (6)-al sub (2 o) sub (3) melts," *Transactions of the Nonferrous Metals Society of China*, vol. 21, no. 2, pp. 402–406, 2011.

[73] N. Dando, X. Wang, J. Sorensen, and W. Xu, "Impact of thermal pretreatment on alumina dissolution rate and HF evolution." in *Light Metals*, 2010, pp. 541–546.

[74] S. E. Gylver, N. H. Omdahl, A. K. Prytz, A. J. Meyer, L. P. Lossius, and K. E. Einarsrud, "Alumina feeding and raft formation: Raft collection and process parameters," in *Light Metals 2019*. Springer, 2019, pp. 659–666.

[75] D. I. Walker, "Alumina in aluminum smelting and its behavior after addition to cryolite-based electrolytes," Ph.D. dissertation, University of Toronto (Canada), Ann Arbor, 1993.

[76] W. E. Haupin, *Principles of Aluminum Electrolysis*, 1995, pp. 1–11.

[77] K. Grjotheim, *Introduction to aluminium electrolysis: understanding the Hall-Hérloult process*. Aluminium-Verlag, 1993.

CHAPTER IV
DETERMINATION OF THE ALUMINA DIFFUSIVITY AND DISSOLUTION RATE FOR ALUMINA SAMPLES IMMERSED IN A CRYOLITIC BATH

4.1 SYNOPSIS

4.1.1 OBJECTIVES

This article contributes to the objectives 1 to 3 of the thesis. The contributions are as follows:

1. The description of the alumina diffusivity and the Sherwood number from the bath composition, temperature, and flow pattern allows the possibility of finding an optimum for the dissolution of an alumina surface.
2. The mass transfer coefficient can easily be found with the Sherwood number for an alumina surface.
3. The Wilke-Chang equation reveals that there are three different mechanisms of diffusion for the dissolved alumina in cryolite melts.

4.1.2 SCIENTIFIC CONTRIBUTION

The first step to understanding the dissolution of a powder raft in cryolite is to quantify the mass transfer through an alumina surface. This article describes the influence of the chemical composition and temperature of the electrolyte on the mass transfer for a known area.

Past works, as presented in the introduction of the thesis, tried to relate directly the dissolution rate to the mass fraction of the additives in the melt and to the superheat. This article tries a new approach by transforming the bath composition and superheat to the bath's internal properties, namely the density, the viscosity, and the alumina gradient. The proof is also made that this simple transformation allows for a substantial increase in the reliability of a mathematical model to predict the data.

This approach is consequent with the usual manner in which mass transfer works are presented with the help of the Sherwood number. The problem is that the diffusivity of the alumina in the electrolyte is of first concern to obtain such a model. Some works, such as Solheim and Skybakmoen [78] and Thonstad et al. [79] tried to obtain this value, but they neglected the influence of the bath composition to favor that of the temperature on the diffusivity of alumina in cryolite. The use of the Wilke-Chang equation [80], as proposed in this article, represents a step forward to a better understanding of the dissolution behavior. This equation allows the finding of the diffusivity of the alumina in different melt compositions, which is essential in mass transfer studies.

The description of the diffusivity makes it possible to describe the influence of the fluid properties through the Schmidt number, along with the Reynolds number in the experimental setup for each condition. A specific Sherwood formulation is then proposed to describe the dissolution in the conditions studied.

The work presented here describes the mass exchange between an alumina surface and the cryolite melt. Therefore, the diffusivity obtained by the Wilke-Chang equation can be used in the case of alumina raft as presented in Chapter 6. However, this model is also suitable to describe the dissolution of a piece of raft that disintegrates from the main raft and can be used in these cases. To perform such calculations, the size of these

chunks and the flow conditions around them should be known. Unfortunately, this is not the case at the moment in industrial conditions.

4.1.3 AUTHORS CONTRIBUTIONS

Work	Contributors
Direction	Prof. László I. Kiss and Prof. Lukas Dion
Original Idea	Prof. László I. Kiss and Thomas Roger
Design of the apparatus	Jonathan Alarie
Construction	Jonathan Alarie and Patrice Paquette
Experimental plan	Jonathan Alarie
Tests	Martin Truchon and Jonathan Alarie
Analysis	Jonathan Alarie
Writing	Jonathan Alarie
Revision	Prof. László I. Kiss and Prof. Lukas Dion
Technical Support	Sébastien Guérard and Jean-François Bilodeau

4.1.4 PUBLICATION

Authors	Jonathan Alarie, László I. Kiss, Lukas Dion, Sébastien Guérard, Jean-François Bilodeau and Renaud Santerre
Year	2023
Title	Determination of the alumina diffusivity and dissolution rate for alumina samples immersed in a cryolitic bath
Journal	Materialia, vol. 32
Status	Published (Reprint permission available in Appendix A.2)
Date	December 2023

4.1.5 RÉSUMÉ

La dissolution de l'alumine est l'un des principaux défis afin de maintenir la stabilité et l'afficacité des cellules d'électrolyse dans le procédé Hall-Héroult. Ainsi, afin de correctement décrire ce phénomène, il est nécessaire de connaître la diffusivité moléculaire de l'alumine dans l'électrolyte. Ceci permet ensuite d'utiliser les relations de transfert de masse pour estimer la diffusion de l'alumine, telle que décrite par la loi

de Fick. Ces travaux proposent d'utiliser l'équation de Wilke-Chang pour déterminer la diffusivité moléculaire de l'alumine et ainsi prendre en compte l'influence de la chimie du bain sur la diffusion moléculaire de l'alumine dissoute. En parallèle, des intervalles similaires à ceux rencontrés en industrie ont été étudiés grâce à la méthode gravimétrique sur des disques d'alumine non-poreux immergés dans la cryolite, avec et sans présence de bulles pour augmenter l'agitation. Les différentes conditions générées modifient aussi le patron d'écoulement dans le montage expérimental et une analyse thermique tente de reproduire le plus fidèlement possible cette influence. Les données ainsi recueillies sont utilisées pour obtenir un modèle plus général grâce au nombre de Sherwood pour prédire le taux de dissolution d'une surface d'alumine dans une conditions donnée. Finalement, une discussion explique les applications possibles et directes du modèle présenté ici.

4.1.6 NOMENCLATURE

Parameter	Definition
a	Sherwood fitting coefficient
A	Area of contact
B	Thickness of the upward velocity layer
d	Diameter
D	Diffusivity
D_0	Arrhenius frequency factor
$\frac{dw}{dx}$	Mass fraction gradient
E_d	Activation energy
Eo	Eotvos number
f	Frequency
f_{sc}	Factor for the suppressed internal gas circulation due to surface contaminants
g	Gravity constant
h	Convection heat transfer coefficient
h_m	Convection mass transfer coefficient
l	Length
L_c	Characteristic length
$\dot{m}$	Mass flow rate
M	Molar mass
Mo	Morton number
Nu	Nusselt number
p	Association parameter
$\dot{q}$	Heat flux
$\dot{Q}$	Volume flow rate
r	Radius
R	Gas constant
Ra	Rayleigh number
Re	Reynolds number
Sc	Schmidt number
Sh	Sherwood number
T	Absolute temperature
V	Volume
U	Velocity
w	Mass fraction
x	Mole fraction

Greek letters	Definition
α	Thermal diffusivity
β	Coefficient of volume expansion
γ	Surface tension
Δ	Difference
ϵ	Emissivity of the surface
κ	Thermal conductivity
μ	Dynamic viscosity
ν	Kinematic viscosity
ρ	Density
σ	Stefan-Boltzmann constant
ϕ	Mass flux

Subscript	Definition
0	Initial value
∞	Bulk value
air	Value for the air
b	Bubble value
$boiling$	Boiling point
$b.sc$	Spherical cap bubble
$b.s$	Spheroid bubble
$b.d$	Influence of the distance from the bubble
$chimney$	Value for the chimney above the crucible
$crucible$	Value inside the crucible
e	Spherical equivalent
env	Value for the surrounding environment
g	Value for the gas
i	Value for the component
l	Value for the liquid
M	Molar
rad	Value for the radiation
s	Surface value
w	Value for the walls

Superscript	Definition
m	Reynolds fitting exponent
n	Schmidt fitting exponent

DETERMINATION OF THE ALUMINA DIFFUSIVITY AND DISSOLUTION RATE FOR ALUMINA SAMPLES IMMERSED IN A CRYOLITIC BATH

Jonathan Alarie[a], László I. Kiss[a], Lukas Dion[a], Sébastien Guérard[b], Jean-François Bilodeau[b], Renaud Santerre[c]

[a] *University of Quebec at Chicoutimi, 555 Boul Universite, Saguenay, G7H 2B1, Quebec, Canada*

[b] *Arvida Research and Development Centre, Rio Tinto, 1955 Mellon Boulevard, Jonquiere, G7S 4K8, Quebec, Canada*

[c] *In Memoriam*

ABSTRACT

The alumina dissolution is one of the main concerns for the stability and efficiency of the electrolysis cells in the Hall-Héroult process. Therefore, to correctly describe this phenomenon, it is necessary to know the diffusivity of alumina in the electrolyte to use mass transfer relationships and evaluate Fick's law of diffusion. In this work, a formulation for the molecular diffusivity is proposed to take into account the influence of the different chemistry of each condition on the diffusivity of dissolved alumina. Then, data obtained by a gravimetric method are correlated to obtain a general formulation of the Sherwood number representing alumina discs immersed in a cryolitic bath. Conditions similar to the industrial range were used to produce these data with and without bubbles. Consequently, the different conditions slightly modified the flow around the sample, which needs an accurate description to obtain an optimal relationship. Finally, a discussion explains how this research is relevant for industrial use.

Keywords: Aluminum electrolysis, Alumina dissolution, Cryolite properties

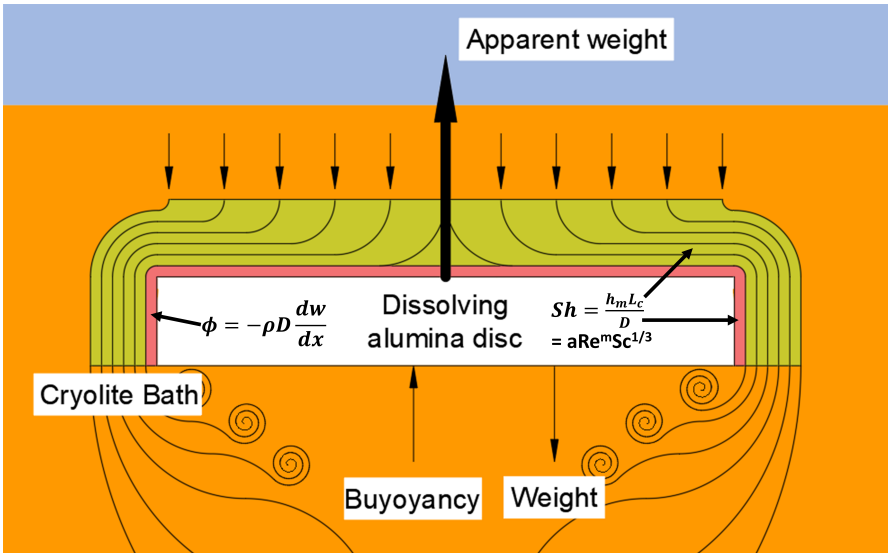

4.2 INTRODUCTION

Uniformity in the concentration of alumina in the cryolitic bath in the Hall-Héroult process is one of the key parameters for the stability of the electrolysis cell. Thus, for a cleaner process and more efficient production, the dissolved alumina needs to be transported to the reaction zone of the electrolysis. However, electrolysis cells are known to have a heterogeneous distribution of alumina varying with time and space [81]. As an example, feeding strategies imply a sequence of overfeeding to increase the dissolved alumina content in the bath, followed by underfeeding periods to deplete all the excess alumina injected into the cell [82]. This leads to the temporal variation of the dissolved alumina content in the bath. In addition, the injection of eight tons or so of alumina per day is done in three to five points over a surface of about 80 square meters with a mean electrolyte height of less than ten centimeters. This configuration necessarily

induces a time lag for the transport of the dissolved alumina to any point in the cell, hence the source of the spatial heterogeneity. The liquid movement, induced by the metal pad and the bubble generation under the anodes, helps the alumina to reach every point in the cell. These variations of the alumina content in the bath favor the muck formation when reaching a maximum concentration and the apparition of anode effects when reaching a low concentration [83]. The muck formation could be harmful to the overall life expectancy of the cell. It increases the cell instability and leads to zones where the resistance to the electrical current is much higher, preventing the electrolysis at these points and prematurely damaging the surrounding area. On the other hand, the anode effect has a more instantaneous effect on the stability of the cell. It rapidly creates an isolating layer of gas under the anode, unbalancing the thermal and electrical equilibrium of the cell. All these phenomena augment the energy consumption of the cell and the release of greenhouse gases [81]. This is particularly true in the case of the anode effect, where the CF_4 and the C_2F_6 gas produced represent respectively 6 630 and 11 100 times the amount of CO_2 equivalent per kilogram released. Hence, to ensure a uniform distribution of dissolved alumina in the cell, it is necessary to understand how it dissolves and mostly, how to enhance its dissolution rate.

It is well known that upon the injection of the powder in the melt, the alumina agglomerates and forms solid rafts that slowly dissolve. It is generally accepted that the main aggregates will be disintegrated into smaller parts that will sink and dissolve at their respective rate. This agglomeration behavior and the subsequent dissolution behavior were determined to be mostly mass transfer controlled, as pointed out by Thonstad et al. [84, 79] and Gerlach et al. [85]. However, a specific condition, namely a low superheat, leads to a heat transfer limited process, as described by Lubyová and Daněk [86] as well as Haverkamp and Welch [87]. These authors, namely Thonstad,

also proposed general equations for the heat and mass transfer process. The work presented in this paper builds upon their works and enhances the general understanding that defines alumina dissolution kinetics. Previous works (Alarie et al. [88, 89]) have shown the general influence of the bath composition and flow around the sample to have an important effect on the dissolution rate. These results were compared with the literature and show good agreement with the different research groups working on alumina dissolution. Following this work, Figure 4.1 and 4.2 show that a change of variable between the bath composition and the bath properties allows a better prediction of the dissolution rate of non-porous disc of alumina immersed in cryolite. Instead of using the mass fraction of the additives and the superheat of the bath, as in Figure 4.1, these compositions have been used to compute the density, the viscosity, and the alumina solubility of the bath. These internal properties are then used to make the regression present in Figure 4.2. The increase in the reliability of the model obtained can easily be explained by the non-linear behavior of the relations between the composition and the properties of the bath. In Figure 4.1 the model is based on the assumption that two bath compositions cannot have the same dissolution rate. On the other hand, Figure 4.2 assumes that it is a given set of properties of the bath that cannot result in the same dissolution rate as another. However, some compositions with different superheat can lead to similar density or viscosity and then should give similar dissolution rates.

Therefore, it became evident that a more specific formulation to describe the dissolution is necessary, especially to catch the non-linear behavior of the process. The model produced in Figure 4.2 unfortunately does not respect the physics relation between the flow properties and the mass transfer between the cryolite and an alumina surface. Consequently, the work presented in this article will try to create a model as

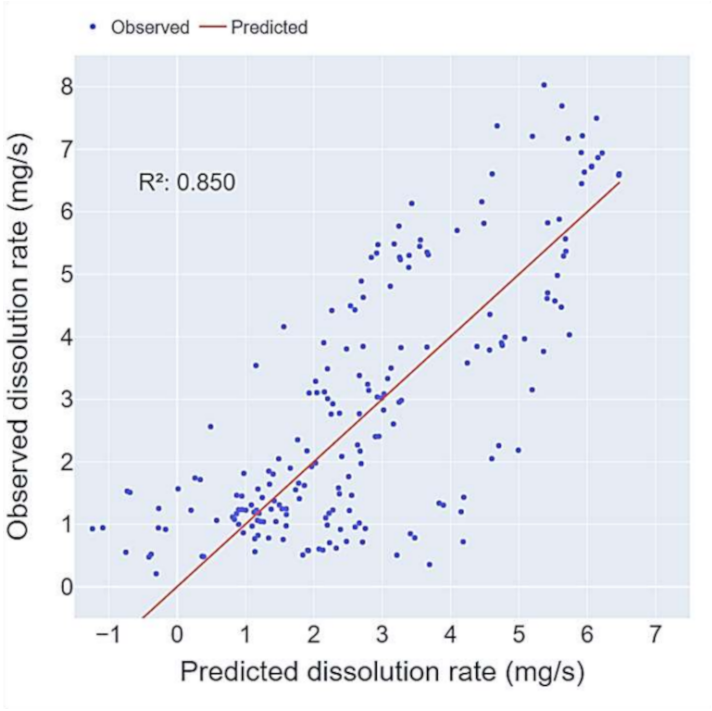

Figure 4.1 : Linear regression of the alumina dissolution rate using the mass fraction of each additive, the superheat, and the bubbling.

representative as Figure 4.2 of the dissolution using a Sherwood number formulation. The present work limits itself to the mass transfer through the known surface of alumina discs and represents only a part of the whole dissolution process of alumina injected in cryolite. Further work will use this knowledge to address the other phenomena involving the use of powder.

4.3 EXPERIMENTAL METHOD

In our approach to the dissolution problem, a series of dissolution tests have been conducted on 99 % sintered alumina discs of 63 mm in diameter by 3 mm high with no apparent porosities (produced by Lianyungang Baibo New Material Co. Ltd). These samples had a mass of 40 g of alumina and allowed the dissolution to occur mainly on

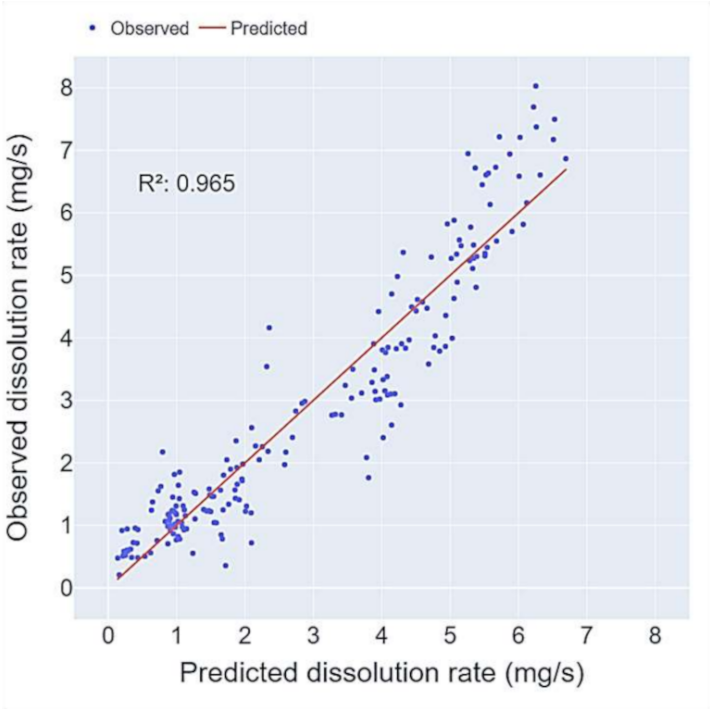

Figure 4.2 : Linear regression of the alumina dissolution rate using the viscosity, density, temperature, and bubbling.

the two circular faces, while the dissolution on the edge can be neglected. This form of the alumina is much simpler than a powder injection and allows understanding of the dissolution process with known conditions, namely the area of contact between the melt and the alumina. The tests were performed in a carbon crucible containing more than 12.5 kg of bath with a diameter of 200 mm placed in a radiative furnace, with a mean bath height of 185 mm. The measurements were performed by a previously developed gravimetric apparatus (see Alarie et al. [90]) to continuously record the diminution of the apparent weight of a sample suspended by a central rod and immersed in cryolite. In addition, a bubbling tube was placed at the bottom of the crucible to allow bubbles to escape from three 6.35 mm holes to agitate the bath around the sample at a rate of 1 Hz, similar to that encountered in industrial cells [91]. A numerical filter was also used to remove the noise created by the vibration of the samples. A total of 35

different conditions were tested with about five to six samples, each time. Additional repetitions were also executed to ensure the repeatability of the method. The associated experimental plan is presented in Table 4.1 and produced about 250 samples overall. Note here that the superheat values are added to the liquidus temperature obtained with the relation of Solheim et al. [92], presented further, to obtain the bath temperature. Since the dissolution of the alumina disc is very slow, the change in the content of dissolved alumina in the bath is negligible (less than 0.1 w% [88]) and the temperature of the bath is then constant for a whole test containing five to six samples. The bath temperature was recorded by a thermocouple located in the center of the crucible at 50 mm from the bottom of the crucible. The components mixed to attain the desired composition were also stored in the ambient atmosphere. Therefore, the thermodynamic equilibrium of oxidation was attained and induced a slight deviation from the real alumina content. These deviations were measured by chemical analysis of the base components and the liquid melt and are taken into account in the analysis. Overall, nearly 150 unique conditions were tested in the experimental work. For simplicity, only the nominal value is reported in Table 4.1, and the deviation is no more than 2 w%. In a typical test, the sample is preheated 25 mm above the bath to prevent any freezing of the melt around it during immersion, thus only considering the chemical effect of the dissolution process. Afterward, the sample is lowered 25 mm under the bath surface and allowed to dissolve for 20 min. Then, the sample will pierce the interface and the buoyancy will influence the sample. Therefore, the apparent weight of the sample will represent its weight from which the buoyancy must be subtracted to retrieve the dissolution rate of alumina. To explain the experimental setup, Figure 4.3 shows the setup of the crucible and the gravimetric apparatus. The apparatus is also equipped with a visualization device to help confirm some behavior and was used on less than 15 samples.

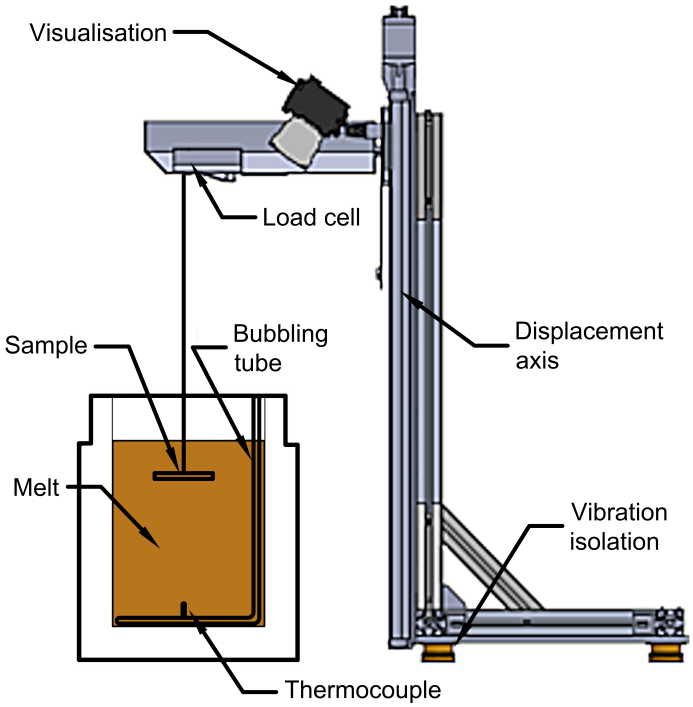

Figure 4.3 : Experimental setup used for the dissolution measurements.

In the setup, the flow around the sample is created by the natural convection resulting from the temperature gradient inside the crucible. At a steady state, a constant heat flux comes from the radiative furnace to heat the wall of the crucible. The lower end is insulated, preventing loss from this direction, while the top of the melt is not completely insulated. Heat loss from the top creates a lower temperature at the melt surface that enables convection. In addition, several tests were conducted with a bubbling generated at the bottom of the crucible. This bubbling was foreseen to enhance the dissolution of the samples and reproduce the conditions encountered by a sinking piece of raft in an industrial cell. Here say that the bubbling was far enough to prevent accumulation under the sample. Even if the flow is created by the natural convection in the crucible, the flow around the sample is considered forced, since the source of the liquid movement is outside the referenced systems, that is to say in the vicinity of the sample.

Table 4.1 : Experimental plans for the sensibility of the dissolution due to the cryolite additive mass fraction and superheat (cryolite filled up to 100 %).

Run	Superheat (°C)	AlF_3 (w%)[1]	CaF_2 (w%)[1]	Al_2O_3 (w%)[1]	Bubbling
1	15	14	7	6	Without
2	10	14	4	6	With
3	5	14	4	3	Without
4	15	9	4	3	With
5	10	9	4	3	Without
6	5	9	7	6	With
7	15	14	4	6	Without
8	5	9	4	6	With
9	10	9	7	6	Without
10	10	14	7	3	With
11	5	14	7	3	Without
12	15	9	7	3	With
13	10	14	4	3	Without
14	10	9	4	3	With
15	5	9	4	3	Without
16	10	9	7	6	Without
17	15	9	4	6	Without
18	5	14	7	3	With
19	15	9	7	3	With
20	15	14	7	3	Without
21	15	14	7	5.25	With
22	5	14	7	6	With
23	5	14	4	3.75	With
24	5	14	4	6	Without
25	15	14	4	3	With
26	5	9	4	6	Without
27	5	11.5	7	6	Without
28	15	9	4	6	With
29	5	9	7	3	Without
30	5	10.25	7	3.75	With
31	5	9	5.5	3	With
32	15	9	7	3	Without
33	15	11.5	7	6	With
34	15	14	5.5	3.75	With
35	10	11.5	5.5	5.25	Without

[1]Mass fraction before melting

4.4 DISSOLUTION

The dissolution process is a complex phenomenon that involves many phases, as presented thereafter. At first, the solid and the liquid must be in direct contact. In the case of an injection of cold alumina powder in a melt with a low superheat, the freeze of the melt can delay this direct contact. Once the contact is established, the solute adsorbs the solvent molecules from its surface. Therefore, a chemical reaction occurs to form new and more stable molecules if the environmental conditions allow it. Finally, the new molecules are desorbed and can migrate to the liquid. This phase change process is usually exothermic since the molecules reach a lower energy state. Here to say that the identity of the molecules formed during the alumina dissolution is a complete field of research. Different authors suggest that several molecules are created during the dissolution, but they do not agree on the number or the identity of these molecules. However, Machado [93] gives a detailed review and analysis of the suspected ions created by the dissolution of alumina in cryolite. She also mentions that the species Al_2OF_x are favored for a cryolite ratio($CR = \frac{\overline{NaF}}{\overline{AlF_3}}$) under 3 or at low alumina concentration and that the species $Al_2O_2F_x$ for CR above 3 or at high alumina content.

As soon as the desorption is completed, the dissolved molecules enter the liquid and diffuse in the concentration boundary layer. This diffusion mechanism limits the net flux of dissolution from the solid to the liquid, because of the no-slip boundary condition at the surface. The Fick's law of diffusion, presented in equation 4.1 from Çengel and Ghajar [94] for a one-dimensional case at constant density, links the net flux of molecules through a given surface (ϕ) with its driving force, the mass concentration gradient ($\rho\frac{dw}{dx}$) with the use of the molecular diffusivity (D) in the liquid. In other terms, Fick's law defines molecular diffusivity as the ability of the solute molecule to move in

a liquid under the driving force of the concentration gradient. Since the gradient of concentration in a direction is hardly known, it is more convenient to use the equation 4.2 to describe the dissolution rate ($\dot{m}$). Equation 4.2 also defines the mass transfer coefficient (h_m) as the effect of the flow and the geometry on the mass transfer through a surface (A) in a liquid of a given density (ρ) driven by a difference of the solute mass fraction at the surface (w_s) and in the bulk (w_∞).

$$\phi = -\rho D \frac{dw}{dx} \left[\frac{kg}{m^2 s}\right] \tag{4.1}$$

$$\phi = \frac{\dot{m}}{A} = h_m \rho (w_s - w_\infty) \left[\frac{kg}{m^2 s}\right] \tag{4.2}$$

Another convenient expression for this phenomenon is the Sherwood number (Sh), presented in equation 4.3. This dimensionless number describes the effectiveness of the convective mass transfer of a characteristic length of the sample (L_c) over the diffusive mass transfer. This is particularly useful because the Sherwood number is known to correlate, with reasonable accuracy (see Çengel and Ghajar [94]), to a function of the Reynolds (equation 4.5) and Schmidt (equation 4.6) numbers, as presented by equation 4.4. Here, the Reynolds number is used to describe the flow around the sample and depends on the velocity of the fluid (V), the characteristic length of the sample (L_c), and the kinematic viscosity (equation 4.7) of the fluid. Therefore, the Reynolds number evaluates to which extent the inertial flow from the speed and the density of the fluid is comparable to its viscous flow. Consequently, a larger Reynolds number illustrates a flow more turbulent, since the viscous flow cannot dampen the variation in the inertial flow as described in Çengel and Ghajar [94]. On the other hand, the Schmidt number describes the convection diffusivity of the fluid, expressed as the kinematic viscosity

(ν), on its molecular diffusivity (D). As a result, the Schmidt number depends only on the property of the fluid and describes the relative thickness of the velocity boundary layer compared to that of the diffusive layer. Note here that these relations are strongly dependent on the accuracy of the values of the electrolyte properties. In the case of the cryolite melt, existing experimental relations between the melt composition and its internal properties give a fair estimation of the value of these properties, but slightly differs from the thermodynamics relations available in the literature (see the works of Robelin, Gheribi, Chartrand, et al. [95, 96, 97, 98]). Therefore, the exact behavior of these properties is still to be found and will influence the results presented here.

$$Sh = \frac{h_m L_c}{D} \tag{4.3}$$

$$Sh = aRe^m \cdot Sc^n \tag{4.4}$$

$$Re = \frac{UL_c}{\nu} \tag{4.5}$$

$$Sc = \frac{\nu}{D} \tag{4.6}$$

$$\nu = \frac{\mu}{\rho} \tag{4.7}$$

While these two numbers (Re and Pr) depend mainly on the flow characteristics and properties, the geometry of the system is also of great importance. This role is achieved in the Sh relation by the preceding coefficient (a) and by the exponents (m and n). These parameters are usually fitted to a curve with experimental data. However, Blasius and Pohlausen, as presented in Welty et al. [99], demonstrated by the exact analysis of the boundary layer that the relative thickness of the velocity boundary compared to the diffusive layer is proportional to $Sc^{\frac{1}{3}}$ instead of only the Sc number for

the mass transfer over a flat plate. Since the geometry used in this work is very similar to a flat plate, it is natural to consider that the n exponent of the Sherwood number relation will be $\frac{1}{3}$. For the two other parameters (a and m), it is necessary to know the flow pattern around the sample. As presented above, the flow is considered to be similar to a flow normal to the top surface of an immersed plate. Since no correlation was found for a finite disc in a flow normal to its surface, Table 4.2 summarizes the coefficient a and m for infinite tubes of cylindrical, squared, and flat cross-section immersed in a liquid with a flow normal to their axis, from Holman [100]. These relations will serve as guidelines for further analysis with the following observations :

1. For the same geometry, the exponent m will increase with the range of the Reynolds number.

2. For a similar range of Reynolds number, the exponent will increase with the turbulence created by the edges of the cross-section.

3. The coefficient a tends to decrease as the exponent and the Reynolds number increase.

The a and m parameters will need to be curve-fitted, but this requires the knowledge of the Reynolds and Schmidt numbers. A description of the flow pattern around the sample will allow finding suitable values for the Reynolds number, while an analysis of the molecular theory will provide input for the molecular diffusivity needed to compute the Schmidt number.

Table 4.2 : Available models in literature for infinite tube immersed in a liquid flow perpendicular to the sample surface for use with equation 4.4, from Holman [100].

Cross section	Re min	Re max	a	m
Cylinder	40	4,000	0.683	0.466
Cylinder	4,000	40,000	0.193	0.618
Square	5,000	100,000	0.102	0.675
Flat plate	4,000	15,000	0.228	0.731

4.4.1 FLOW DESCRIPTION

The description of the flow around the sample is of primary concern in this kind of analysis. Any deviation from reality can lead to a large loss of accuracy in the model. It is then a priority to experimentally characterize the flow to have a better model available. However, this is not always possible, as in the case presented here. The high temperature and the hostile environment of the molten cryolite prohibited the measurements of the flow pattern in this study. Hence, a theoretical approach to the characterization of the flow is here used. This theoretical analysis will ensure that the relative change of the flow from one condition to another is consistent with reality and an experimental measurement should be conducted to confirm the results. Figure 4.4 shows the expected flow around the sample. The dominant flow comes from the natural convection in the crucible, created by the heat flux from the wall through the melt. So, the heat flux increases the liquid temperature and thus lowers its density at the wall interface. Therefore, the liquid will rise on the wall of the crucible and accelerate to attain its maximum velocity at the surface of the melt. Once at the free surface, the fluid will travel from the wall of the crucible to its middle. Meanwhile, the liquid will heat the air in contact with it, consequently lowering its temperature and increasing its density. This will provoke a part of the melt, which has gained a higher density, to go

down instead of reaching the middle. This will result in a pretty constant downward flow from the free surface to the bottom of the crucible, as demonstrated by Hess et al. [101]. In this kind of geometry, this natural convection can be described by the Rayleigh number, as presented by Hess et al. [101] in equation 4.8. This equation takes as input the gravitational constant (g), the heat flux from the wall (q_w), the volume expansion coefficient (β), the characteristic length of the wall (L_{c-w}) over the kinematic viscosity (ν), the thermal conductivity (κ), and the thermal diffusivity (α) of the bath. It is important here to understand that the flow created by the heat flux is a natural flow only if the reference system is the crucible. In such a case, the flow is internal to the system and thus considered natural. However, when the studied system is a smaller piece inside the crucible, such as the alumina sample in our case, the liquid flow is created by an external source. Then, the flow around the sample is by definition a forced convection, especially since the sample has little influence on the global flow pattern (see Bird et al. [102]).

$$Ra_{crucible} = \frac{g\beta q_w L_{c,w}^4}{\nu\kappa\alpha} \tag{4.8}$$

$$\dot{q}_{rad}\left[\frac{W}{m^2}\right] = \epsilon\sigma\left(T_s^4 - T_{env}^4\right) \tag{4.9}$$

$$Gr_{chimney} = \frac{g\beta\Delta T x^3}{\nu^2} \tag{4.10}$$

$$Nu = \frac{hl_{chimney}}{\kappa_{air}} \tag{4.11}$$

$$\dot{q}_{conv}\left[\frac{W}{m^2}\right] = h\Delta T \tag{4.12}$$

To find the Rayleigh number in such a way, the electrolyte's internal properties are needed. These properties can be obtained with the values presented in Table 4.1

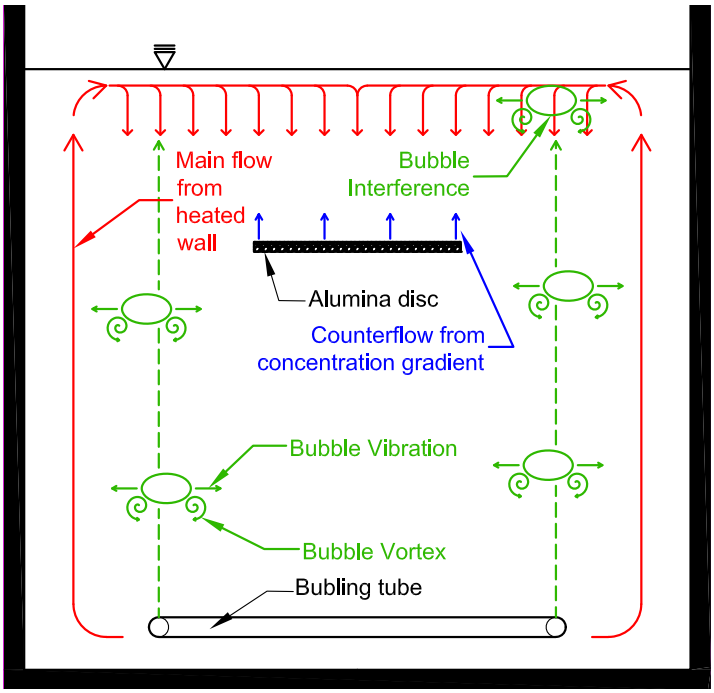

Figure 4.4 : A description of the different flows in the experimental setup. The main flow is created by the heating of the walls (red lines), agitation added by the bubbles (green lines), and natural convection created by the sample (blue lines).

and from the relations found in the works of Kvande et al. [103], Hertzberg [104], and Khokhlov [105], most of them presented in Thonstad [106]. However, the relation of the viscosity from Hertzberg [104] was slightly modified with the help of the work presented by Robelin and Chartrand [96] to take into account the contribution of calcium fluoride to the viscosity. This modification represents only an estimation of the contribution of the calcium fluoride to the viscosity. The approach used by Robelin and Chartrand [96] is expected to give a more precise result, but this level of precision was unnecessary at this stage of the work. The characteristic length (L_{c-w}) in this type of flow is considered to be the height of the liquid. This represents the maximal length between the minimum and maximum temperature in the system as shown in the VDI heat atlas [107]. In this work, the characteristic length (L_{c-w}) is then 185 mm.

Heat flux from the wall (q_{rad}) to calculate the Rayleigh number can be estimated with a simple heat transfer scenario, illustrated in Figure 4.5. At a steady state, the heat flux from the furnace will keep the bath at a constant temperature by compensating the radiative and convective heat loss. The radiative heat loss ($\dot{q}_{rad}$) can easily be estimated from equation 4.9 using the Stefan-Boltzmann constant (σ) and the temperature difference between the melt (T_s^4) and the environment (T_{env}^4), assuming a black body emission. This assumption is supported by the fact that the radiation emitted by the melt needs to heat the walls of the chimney, which themselves lose heat by radiation to the environment. So the surface of the opening of the chimney, which is supposed to be similar to the melt surface due to the instruments inserted in the bath, can be considered to have an emission coefficient of 0.9 (ε) since the setup does not act as a perfect black body. Also, the convective heat loss ($\dot{q}_{conv}$) through the chimney can be estimated with the help of the Grashof number ($Gr_{chimney}$) of equations 4.10 with the temperature difference between the hot and cold points (ΔT) at a given chimney length ($l_{chimney}$). Considering the air thermal conductivity (k_{air}) at 550°C, it is possible to find the Nusselt number (Nu) and to retrieve the convective heat loss with equations 4.11 and 4.12. When applying these equations to the experimental setup used in this work, it turns out that the convective heat loss is about 5 % of the total heat loss. From this result, the convective heat flux has been neglected in further calculations.

From the heat flux (q_w) found with equation 4.8, the mean velocity (U_l) of the liquid can be estimated by equation 4.13 adapted from [102] to use the heat flux from the wall as in Hess et al. [101]. This relation needs the thickness of the upward velocity layer (B) as an input and can be found with the help of the work from Hess et al. [101]. They present a relation between the Rayleigh number and the thickness of the rising layer. Simple regression then allows the use of such a relation in this work. From

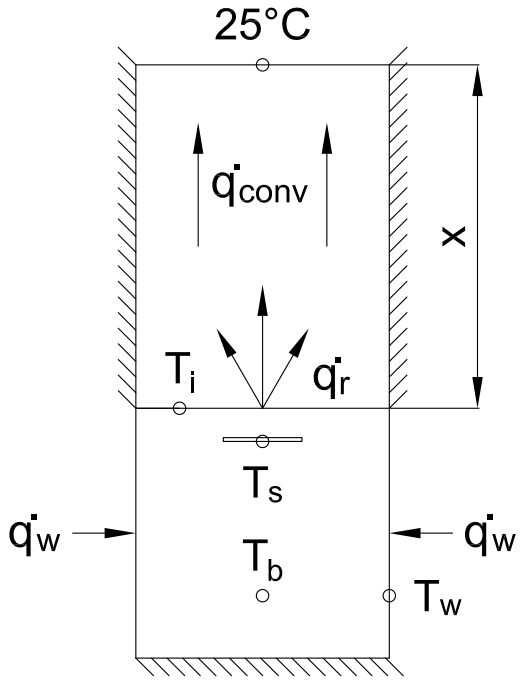

Figure 4.5 : Schematic of the heat transfer model used to estimate the natural convection in the different experimental setups. The interface temperature (T_i) drives the radiative heat loss from the melt surface, while the convective heat flux from the surface to the environment through a chimney of a given length (x) can be neglected. This heat loss is compensated by the heat flux from the furnace ($\dot{q}$), creating the temperature difference between the wall (T_w) and the bulk (T_b). The sample temperature (T_s) is also slightly lower than the bulk due to the dissolution process.

their results, it can also be seen that the upward velocity obtained is about three times larger than the downward flow. The velocity of the liquid estimated this way was also confirmed by a video recording of the dissolution of a few samples.

$$U_l = \frac{\rho \beta g q_w B^3}{48 \mu \kappa} \tag{4.13}$$

As pointed out above, the flow of the liquid in the crucible can only be considered as a natural flow for the crucible itself. From the sample point of view, the flow created by the heating of the crucible leads to a forced convection around the sample. This is inherent to the definition of a forced flow for which the flow pattern needs to be created by a source external to the system studied (see Bird et al. [102]). The velocity of the bath can then be used to compute the Reynolds number, as presented in equation 4.5, and using the diameter of the sample. Also, some tests were performed with bubbling from the bottom of the crucible. As it can be seen in Figure 4.4, the bubbling flow increases the mixing of the melt around the sample. Furthermore, it increases the turbulence of the main flow in interaction with the sample. It is now necessary to estimate the bubbles rising velocity to find the contribution of the bubbles to the convection. This will be used to find an effective Reynolds number for the sample, along with those of the main flow and the natural convection created by the sample dissolution. The relations presented here allow a good estimation of the contribution of the bubble to the convection of the liquid around the sample. However, this demonstration relies on some assumptions, such as the creation of uniform spherical bubbles by the bubbling tube that rapidly attains its terminal speed. Since the reality can slightly differ from these hypotheses, namely by the wear of the tube, the exact contribution of the bubble to the convection can be difficult to catch. To overcome such problems, it should be necessary to experimentally measure this contribution with an adapted apparatus, which is difficult to implement.

From the radius of the hole in the bubbling tube (r_0), the surface tension of the liquid (σ_l), and the density difference between the liquid and the gas used ($\Delta\rho$), Tate's law (equation 4.14) related by Park [108] gives us the equivalent volume (V_e) of the bubbles created. When the gas flow is well known, it is also possible to relate the known

frequency of the escaping bubbles (f) to the gas flow ($\dot{Q}_g$) and an equivalent bubble volume by the simple relation in equation 4.15. So, with the equivalent spherical bubble volume, the equivalent diameter of the bubble (d_e) can be computed from geometric relation, with a mean value of 6 mm. Then, Park [109] related different equations for the terminal speed of a bubble (U_b) in a liquid pool for different bubble shapes. He shows that there is a relation between the Reynolds number, the Eotvos number (presented in equation 4.16), and the shape of a bubble. So, as a first estimation, the relation of a spherical-cap bubble presented in equation 4.17, along with equation 4.19 deduced from Miller [110] to assess the influence of the distance between the bubble and the sample (l_b), was used to estimate the Reynolds number. With this relation, the Reynolds number of a rising bubble, with its equivalent diameter as the characteristic length (L_{c-b}), is in the order of 10^2. Also, the Eotvos number of bubbles of 6 mm in diameter in liquid cryolite of a given density (ρ_l) is about 6.5. With this information, Park [109] shows that a bubble should have a spheroid shape. Substituting equation 4.17 with the equation 4.18 gives the terminal speed for a spheroidal bubble. This velocity can then be applied to the Reynolds number expression (eq. 4.5) with the equivalent bubble diameter as the characteristic length (L_{c-b}) and the melt kinematic viscosity.

$$V_e = \frac{2\pi r_0 \sigma_l}{\Delta \rho g} \tag{4.14}$$

$$\dot{Q}_g = f V_e \tag{4.15}$$

$$Eo = \frac{g \rho_l d_e^2}{\gamma_l} \tag{4.16}$$

$$U_{b.sc} = 0.721 \sqrt{g d_e} \tag{4.17}$$

$$U_{b.s} = \sqrt{\frac{2.14 \sigma_l}{\rho_l d_e} + 0.505 g d_e} \tag{4.18}$$

$$U_{b.d} = 0.7256 \cdot U_{b.sc} \frac{d_e}{l_b} \tag{4.19}$$

The last contribution to the convection around the sample comes from the difference in density between the sample surface and the bulk density. This difference is caused by the dissolved alumina content and the temperature drop of the liquid in contact with the sample. As it happens, the alumina in contact with the liquid will dissolve and the liquid region close to the sample will become saturated with dissolved alumina. This causes the liquid to have a lower density than the bulk density. In parallel, the dissolution process is an endothermic reaction. This implies that the melt needs to give a fraction of its thermal energy to allow the dissolution, leading to an estimated temperature of 2°C lower (from the ratio of the heating and dissolution enthalpies change presented by Solheim et al. [78]) and thus, a slightly higher density at the sample surface. To adequately compute the Rayleigh number, the density of the melt instead of its temperature gradient needs to be applied like equation 4.20. Similarly to the thermal liquid flow, the equivalent velocity created by the natural convection of the thermal and concentration gradient can be found by equation 4.13 and used to find the associated Reynolds number. Here, it is worth mentioning that the temperature gradient in the

density formulation from Kvande et al. [103] has an influence of an order of magnitude lower than that of the concentration gradient and can then be neglected. Moreover, the whole contribution of the density gradient from temperature and concentration from the sample surface to the bulk value is thin around the alumina disc compared to that of the convection provoked by the heating of the crucible. Therefore, this analysis is only useful when the natural convection around the sample is dominant, which is not the case in this work. The natural convection created by the dissolution of the alumina is then negligible.

$$Ra = \frac{g\Delta\rho L_c^3}{\rho_l \nu \alpha} \tag{4.20}$$

Now that every contribution to the convection in the systems has been described, it is time to add them in a congruent way. For this purpose, Çengel and Ghajar [94] described equation 4.21 to add to the effect of natural and forced convection in an assisting or transversal configuration and subtract those in opposing effects of heat transfer problems. Usually, the exponent found in equation 4.21 depends on the geometry and varies between three and four when dealing with vertical and horizontal flow, respectively. Since the flows observed in the present work affect the same surface, an acceptable simplification is that the characteristic length and the kinematic viscosity used to calculate the Nusselt number (Nu) from the Reynolds number are quite the same. Also, the geometry used here is not as simple as those presented in Çengel and Ghajar [94]. The rising bubbles flow farther away from the wall of the crucible, where the heat convection takes place, and then can't be seen as a perfect assisting flow, nor opposing to the downward flow that takes place around the sample. In addition, the

rising bubbles cause small whirlpools in the liquid as they rise and bring more liquid to the surface of the melt. So, to adequately represent the addition of the main and bubble flow to the natural convection created by the sample, equation 4.22, derivates from equation 4.21 assuming constant ν and L_c, is proposed to find a unique Reynolds number for the situation. For this purpose, the n exponent in equation 4.21 was fixed to 3, due to the vertical flow. Figure 4.4 shows the relation between these different flows. Here, the main flow influence is enhanced by the bubble flow. Their movement brings more liquid from the bottom of the tank to its top and adds turbulence to the flow already existing from the thermal convection of the crucible. On the other hand, the natural flow created by the concentration gradient between the surface of the sample and the bulk slightly reduces the flow around the sample. Then, the main and bubble flow need to be added together, while the density gradient flow of the sample is subtracted, even if it is negligible.

$$Nu = \sqrt[n]{\sum \pm Nu_i^n} \tag{4.21}$$

$$Re = \sqrt[3]{\sum \pm Re_i^3} \tag{4.22}$$

4.4.2 MOLECULAR DIFFUSIVITY

The molecular diffusivity is of first interest in mass transfer: it is often the limiting parameter, as stated by Fick's law (eq. 4.1). In mass transfer correlations, this behavior is taken into account in the Sherwood and the Schmidt numbers, which use this value as a reference to estimate the contribution of the convection to the mass transfer process. Hence, the accurate description of the dissolution conditions will deeply impact the

model obtained. For this purpose, the molecular diffusivity of the alumina in cryolite melt has been estimated to be $1 \times 10^{-9} W/m^2$ by Thonstad et al. [79]. This value was later confirmed by Solheim and Skybakmoen [78], who also specified its dependence on the absolute temperature (T) and the gas constant (R) as well as a fitting constant (D_0). They used the Arrhenius equation to establish the temperature dependence of a chemical reaction (here the diffusion D) with two parameters, an activation energy threshold (E_D) and a factor specific to the reaction (D_0) to obtain equation 4.23, specific to the molecular diffusivity.

This relation supposes that the main diffusion mechanism of the alumina in the melt occurs in a somehow stable lattice with some space that can be reached only by the overcoming of energetic barriers (E_D), as presented in Figure 4.6. While this hypothesis is strongly supported in solid diffusion phenomena, the mechanism involved in liquid diffusion is more diverse and complex. As an example, Hirschfelder et al. [111] described a mechanism where the diffusion occurs by the swap of two molecules, as in Figure 4.6. In this kind of diffusion, the required activation energy is much lower than that needed in a solid diffusion, due to a lower bottleneck from the static molecules. Therefore, in addition to the temperature of the liquid, the molecular diffusivity will also depend on the mobility of the molecules. Then, it is more convenient to use the viscosity in the definition of the molecular diffusivity. The viscosity of the liquid describes the shear stress between two layers of a fluid in motion relative to each other. In a diffusion mechanism as described in Figure 4.6, the swap between the two molecules also induces a motion between some molecules and thus will certainly be influenced by the viscosity.

Some formulations to describe the molecular diffusivity with the use of temperature and viscosity already exist. For simplicity, yet precise formulation, the modified Wilke-

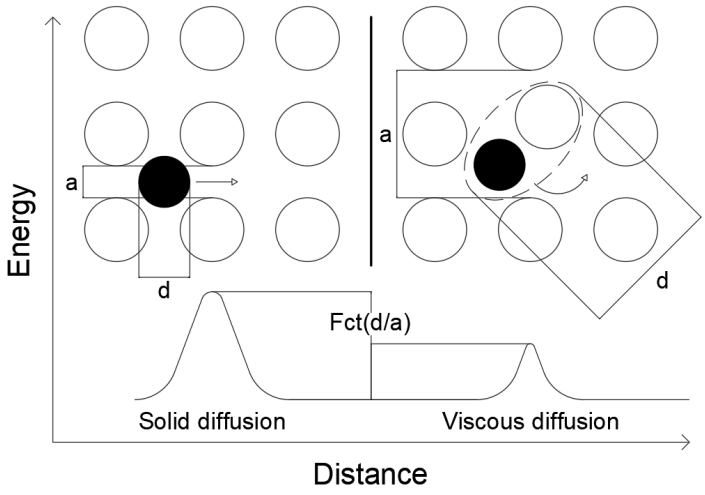

Figure 4.6 : Description of the different diffusion mechanisms (adapted from Hirschfelder [111]) In a rigid matrix (left side), the diffusion needs to overcome a strong energetic barrier. In a liquid (right side), the molecules of the solvent can also be displaced, so that the energy required for the diffusion process is lower.

Chang equation was selected and is presented by equation 4.24 which was adapted for a multicomponent mixture from Miyabe et al. [80]. To describe the "resistance" of the melt to the solute diffusion, this empirical correlation uses the absolute temperature (T) and dynamic viscosity (μ) of the melt. Also, the molecular weight of the component of the solvent (M_i) and the mole fraction (x_i) of these components, along with an association parameter (p_i), will influence this "resistance". The size of the solute molecule is taken into account with the help of the molar volume at the normal boiling point of the solute ($V_{M,boiling}$) and can also use an association parameter (p_s) to describe the solute affinity with the solvent. As stated by Wilke and Chang [112], this relation is a simplification of the real mechanism involved in diffusion and represents only a practical result. Since the molecular diffusivity in the industrial cryolite melt represents a challenge to measure, this formulation will be used as a first estimation with every association parameter set to unity.

$$D = D_0 \cdot e^{\frac{-E_D}{RT}} \tag{4.23}$$

$$D = \frac{7.4 \times 10^{-8} \cdot T\sqrt{\sum x_i p_i M_i}}{\mu (p_s V_{M,boiling})^{0.6}} \tag{4.24}$$

$$\rho_{Al_3O_3,l} = 2.79(1 - 4.22 \times 10^{-5}(T - 2500)) \tag{4.25}$$

$$V_{M,boiling} = \frac{M}{\rho_{Al_2O_3,l}} \tag{4.26}$$

In equation 4.24, it is necessary to use the molecular weight of each basic component of the bath. So, the cryolite needs to be split in terms of NaF and AlF_3. This will therefore take into account the chemistry change induced by a higher bath ratio. Also, the association theory used by Wilke [112] states that non-associated solvents and other non-hydrogen bonding solvents should use an association parameter (p) of unity, while water mixtures use a parameter of 2.6, which represents the higher border. In the absence of hydrogen bonding in the cryolite melt, an association parameter of unity has been selected for each component of the bath. The Wilke-Chang equation also needs the molar volume of alumina at its boiling point, which is attained at 3250 K. At this temperature, the density of the liquid alumina ($\rho_{Al_2O_3,l}$) at atmospheric pressure can be found with the help of the equation 4.25, found by Glorieux et al. [113]. Despite the fact that this relation is limited to the range of 2000 K to 3100 K, Shi et al. [114] demonstrated that this correlation can be extrapolated up to the boiling temperature with good reliability. So, the density of alumina at its boiling temperature is assumed to be 2.702 g/cm^3. With the molar mass of alumina (M) of 101.96 g/mol, the molar volume of the solute ($V_{M,boiling}$) can easily be found with equation 4.26 to be 37.74 cm^3/mol in standard conditions.

4.5 RESULTS

4.5.1 MOLECULAR DIFFUSIVITY

With the theoretical background presented above, it is now possible to compute the molecular diffusivity value needed for the Schmidt number (eq. 4.6). Using the Wilke-Chang equation (eq. 4.24), Figure 4.7 presents the molecular diffusivity obtained for each sample. The values of the diffusivity vary from $2.51 \times 10^{-9}\, m^2/s$ to $3.29 \times 10^{-9}\, m^2/s$. From this Arrhenius-type plot, it can also be seen that the logarithm of the molecular diffusivity group itself into three linear batches of data when plotted against the reciprocal of the temperature. This grouping is indeed inherent to the experimental plan presented in Table 4.1. Nevertheless, hypotheses on the cause of this aggregation are presented here. The trend line of each of these data batches will give the activation energy for the diffusion process, according to the Arrhenius equation (eq. 4.23). The aggregation present in Figure 4.7 suggests that there are different mechanisms of diffusion in the range of bath composition studied. The first one (solid red line) shows a mechanism that needs more energy before the activation of the diffusion. The slope of the line gives an energy of activation for the diffusion (E_D) of $-92\, KJ/mol$ and a constant (D_0) of $2.5 \times 10^{-5}\, m^2/s$. Also, this mechanism appears only with the sample for which the cryolite ratio is under 2.2, as shown in Figure 4.7. Above the limit of 2.2, two other mechanisms can be observed. From Figure 4.7 a similar diffusion mechanism (pink dotted line) can be observed with cryolite ratios above 2.5. This mechanism has an activation energy of $-97\, KJ/mol$ and a constant (D_0) of $3.4 \times 10^{-5}\, m^2/s$, which leads to a smaller molecular diffusivity than the first mechanism. A third mechanism appears between the first two (blue dashed line) and it is characterized by a much lower activation energy of $-67\, KJ/mol$ and a constant (D_0) of $1.9 \times 10^{-6}\, m^2/s$. However,

this chunk of data covers a wide range of CR, and the associated hypotheses are still being studied.

The results of the first mechanism are comparable to those reported by Solheim et al. [78], who obtained an energy of activation of $-79\,485\,J/mol$ with a constant of $2.50 \times 10^{-6}\,m^2/s$ with their data. The constant that they obtained is indeed different from what we found, but it can be easily explained with Figure 4.8. In this figure, our data are plotted beside those reported by Solheim et al. [78], neglecting the right part of the plot, and three things show up. First, there is a slight shift between the two sets of data. As mentioned, the Wilke-Chang equation is an approximation of the molecular diffusivity and can slightly differ from the real value. Furthermore, Solheim et al. [78] mentioned that the strict experimental requirements of the rotating disc method can't be fulfilled. This can also lead to a difference in their value compared to the real value of the molecular diffusivity. The second reason is that Solheim et al. [78] neglected the effect of the chemical composition of the bath on the molecular diffusivity. Therefore, they fitted all the data available to the Arrhenius equation 4.23, thus obtaining a different equation. It can easily be seen from Figure 4.8 that their results, despite an offset, fit the mechanisms that we identified. The third reason is that the association parameters for the alumina (p_s) used in the modified Wilke-Chang equation 4.24 can be different from unity. Consequently, as the association parameter is raised, the difference between the constant found by Solheim et al. [78] and in this work will decay.

The presence of three diffusion mechanisms is consistent with the description of the structure of dissolved alumina in cryolite made by Kvande et al. [115]. They show that the cryolite ratio favors the formation of different anions. Their work shows that at CR

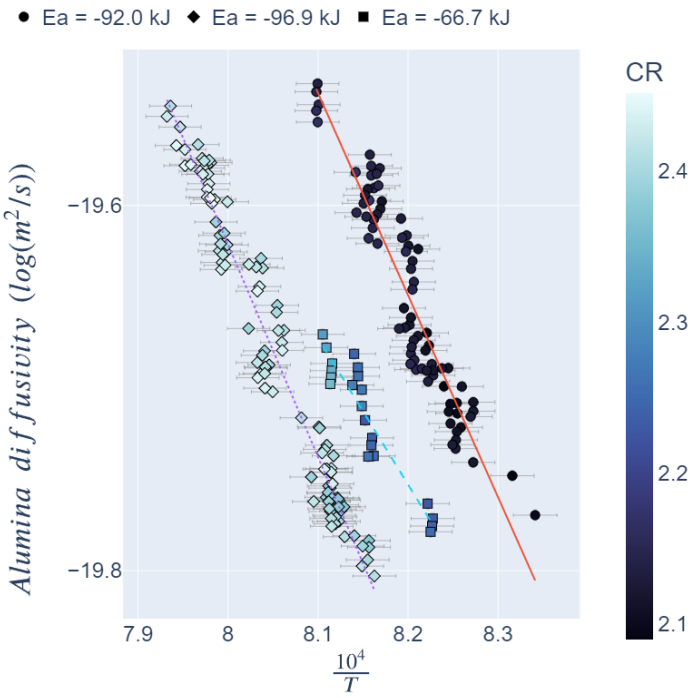

Figure 4.7 : Arrhenius plot of the molecular diffusivity and its dependence on the bath ratio. The regression lines indicate three different mechanisms of diffusion.

under 2.2 at 1012 °C, the anion $Al_2OF_6^{2-}$ is rapidly favored, with a maximum obtained around 1.5. We suppose that this observation is somehow similar to a temperature slightly lower, such as in the range studied in our work. This is plausible if the formation of these anions depends both on the temperature and the molar ratio, as expected for any chemical reaction. In this case, the first diffusion mechanism observed in Figure 4.7 (solid red line) could be associated with the formation of the $Al_2OF_6^{2-}$ anion. As the CR increase, the fraction of the anion $Al_2OF_6^{2-}$ rapidly decays and some other anion begins to form, such as the $Al_2O_2F_6^{4-}$ and $Al_2OF_8^{4-}$, while the anion fraction of $Al_2O_2F_4^{2-}$ slightly increase. The similarity between the evolution of the CR in the second mechanism of diffusion and the variation of the molar fraction of the anions suggest that the second diffusion mechanism (pink dotted line) appears with a sufficient fraction of the $Al_2O_2F_6^{4-}$ and $Al_2OF_8^{4-}$ anions. The third mechanism seems to come

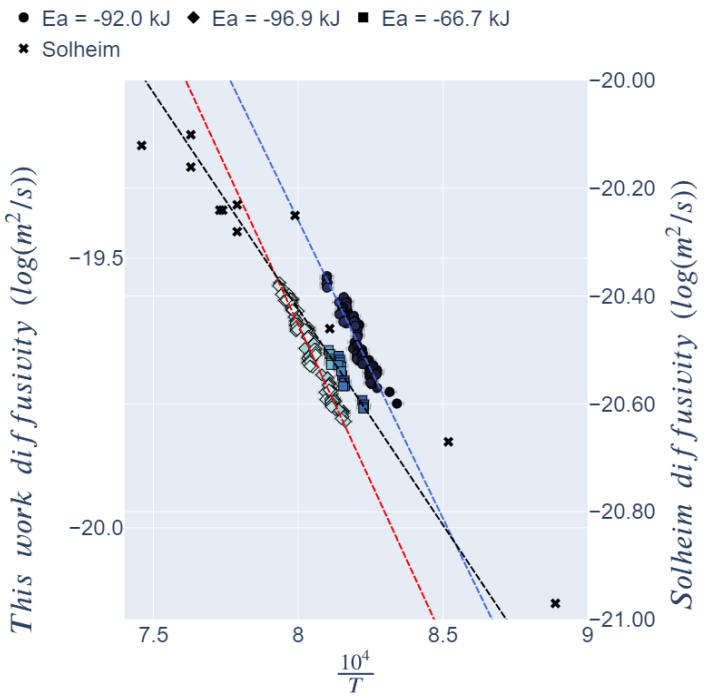

Figure 4.8 : Comparison of the results from this work and the results reported by Solheim et al. [78] (black points).

from the absence of those anions and the $Al_2OF_6^{2-}$ anion formed at lower CR. On the other hand, the anion $Al_2O_2F_4^{2-}$, which we suspect is present at all CR in this work, seems to establish a minimal value of the activation energy of the diffusion process. In addition, the size of the structure of these anions, as modeled by Machado [93], could partially explain these diffusion behaviors. Machado [93] shows that the anion $Al_2O_2F_6^{4-}$ has a slightly more compact structure than the three other anions, so this anion requires relatively less space between the adjacent molecules to diffuse, and then lowers the activation energy required, as explained in Figure 4.6. However, the affinity of the anion with the surrounding molecules also has a strong effect, leading to an overall lower molecular diffusivity for this anion than for $Al_2OF_6^{2-}$.

In brief, the alumina dissolves with the help of the molecules that are adsorbed at its surface. There is indeed a preference to adsorb a given molecule at the surface, which will be the energetically favorable form. However, due to the dissolution, the amount of this molecule in contact with the surface will slowly deplete, and less favorable molecules will then be adsorbed at the surface of the alumina. This kinetics is driven by the diffusive capability of each of these molecules. Then it is difficult to identify these molecules and their diffusive properties in cryolite. Nevertheless, the purpose of this section is not to identify these molecules but to pinpoint the need to research these topics to enhance our knowledge of alumina dissolution. From this analysis and Figure 4.7, it is clear that the formation of some anions, in a given set of conditions, can favor the diffusion process. Two strategies can show up from this statement :

1. At a given temperature in standard industrial conditions, a lower CR can promote the formation of specific anions that facilitate diffusion.

2. At a given cryolite ratio, a higher temperature will increase the diffusion process.

These statements are of first importance because, as stated by Fick's law (eq. 4.1), the dissolution of alumina is limited by the diffusive layer around the solid. The increase of the molecular diffusivity then leads to an increase in the dissolution rate of alumina. The results obtained here are in good agreement with past works, such as presented in Thonstad [106], about the behavior of the dissolving alumina. However, the determination of the dissolution rate by the use of the Sherwood formulation and the Wilke-Chang equation allows the quantitative comparison of the effects of the bath composition on the alumina dissolution. Providing that the Reynolds number and the flow pattern can be determined, the dissolution rate of an alumina piece in the bath can be determined. Therefore, the quantification of the influence of the bath chemistry on

the dissolution rate represents a valuable tool for cell control calculations, concerning the chemistry difference from one pot to another.

The results presented in Figure 4.7 influence the Schmidt number necessary to calculate the Sherwood number. Table 4.3 summarizes the results obtained and their influence on the Schmidt number. Two simple calculations using the product of the viscosity and diffusivity have also been added to Table 4.3. These calculations try to compare the results obtained by the Wilke-Chang equation with those expected from the Stokes-Einstein equation. Here mentioned that the original experimental work was not designed to be used with the Stokes-Einstein equation and more work is needed to draw certain conclusions from this comparison. More tests need to be done at a constant temperature with different electrolyte compositions and different temperatures with the same composition. In this work, only scarce pairs of tests respect these restrictions necessary to apply the Stokes-Einstein law. Nevertheless, the variations in temperature or solvent composition are assumed small enough to allow this comparison to be of interest. As shown in Table 4.3, the product of the viscosity and the diffusivity gives results that vary no more than 4 % from the mean. This can indicate, as predicted by the Stokes-Einstein equation, that the product seems constant within the experimental error. The last column represents a simple attempt to retrieve the influence of the temperature on the otherwise constant parameters of the Stokes-Einstein equation and gives a variation of 2 %. The low variation in these two columns shows that the results obtained by the Wilke-Chang equation are in good agreement with those expected by the Stokes-Einstein. However, as stated above, more work is needed to confirm that the application of the Stokes-Einstein equation to determine the diffusivity of the alumina in cryolite melts is well suited to cryolite melts.

Table 4.3 : Summary of the results obtained for the diffusivity of alumina in cryolite melts.

	Diffusivity $(10^{-9}\frac{m^2}{s})$	Sc	$\mu \cdot D$ $(10^{-12}N)$	$\frac{\mu \cdot D}{T}$ $(10^{-15}\frac{N}{K})$
Min	2.51	345	7.42	6.10
Max	3.28	573	7.75	6.24
Dev.	27 %	50 %	4 %	2 %

4.5.2 ALUMINA DISSOLUTION

The description of the effect of the bath composition on the molecular diffusivity allows the estimation of the Schmidt number (eq. 4.6). Along with the Reynolds number obtained for the flow description and listed in Table 4.4, it is now possible to predict the dissolution rate of our samples with the Sherwood number (eq. 4.4 and 4.6) and the definition of the mass transfer coefficient (eq. 4.2). Note here that the molecular diffusivity obtained by the Wilke-Chang equation remains only an estimation. Therefore, the Schmidt number can have a slight deviation from the real behavior of the molecules. In this case, any regression made on this parameter to find its exponent for the Sherwood number formulation can only be misleading. In consequence, the Schmidt number exponent will remain fixed at $\frac{1}{3}$, because it is the most reasonable approximation available with our current set of hypotheses. To find the other constants (a and m), the logarithm of both the measured dissolution rate and the estimated rate obtained with equation 4.2 to 4.4 must be used. Such manipulation allows obtaining the Reynolds number exponent. From the slope of the regression curve, an exponent of 0.767 can be found with a standard deviation of 0.029. This exponent can be compared to those presented in Table 4.2 and shows a behavior slightly more turbulent than that produced by an infinite flat plate. This added turbulence is expected, because a finite disc will see the flow separate all around it, instead of only on two sides. However, the exponent of

the Reynolds number of our flow is expected to be slightly higher in the same Reynolds number range. Though, since the Reynolds number range in our data is lower than that of an infinite flat plate, ranging from 200 to 425, it is also expected that the exponent found should be lower, as presented by Table 4.2 for the cylindrical tube. Hence, the exponent of 0.767 seems to be plausible with the behavior expected from the literature. Now, to obtain the value of the constant a, a regular regression is made to predict the experimental dissolution rate with the theoretical rate, this time using the exponent found. The result of this second regression leads to Figure 4.9 where the vertical axis is the data obtained from the experimental plan (Table 4.1) and the horizontal axis represents the calculation of the dissolution rate with the help of equations 4.2 to 4.6. The slope of the constrained to the origin regression of the data gives the value of the constant (a) in the Sherwood number equation (eq. 4.4). From Figure 4.9, it is clear that the model used to predict the alumina dissolution can describe the main influences of the melt composition on the dissolution rate.

Table 4.4 : Reynolds number obtained from the flow description method.

	Main	Natural	Bubbling	Resulting
Min	195	0	0	199
Max	264	25	388	425

The experimental error of the method represents a relative error of 6.3 %, with the confidence of 95 %, for values higher than 1 kg/s, at the right end of Figure 4.9. Unfortunately, this same error is much more important relative to the results obtained in the left end of the figure. To overcome this lower confidence, it is appropriate to fix the y-intercept to zero. It is indeed expected that the dissolution rate of the sample will be voided if the concentration gradient, used to compute the horizontal axis, is zero. This led to the retained constrained model presented by the solid orange line with a

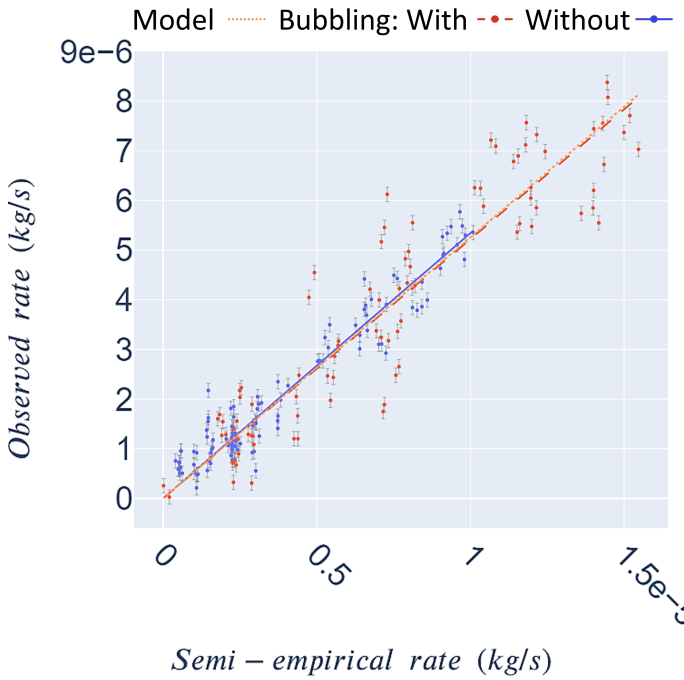

Figure 4.9 : Prediction of the experimental dissolution rate (vertical axis) by the semi-empirical rate obtained from equations 4.2 to 4.6. The slope of the regression line gives the value of the constant a, required in equation 4.4. The error bar represents the repeatability of the measurements.

slope of $0.598 \pm 1.538 \times 10^{-2}$, with a confidence of 95 %. This result is comparable with the known relation presented in Table 4.2. As stated before, an increase in the Reynolds exponent should lower the value of the constant a, while a lower Reynolds number should increase it. This time again, these two phenomena lead to a result similar to that of an infinite plate in a perpendicular flow.

The confidence in this model is reinforced by the study of the assumptions made to build it. Figure 4.10 shows the influence of each assumption on the correlation coefficient of the constrained model. Three major conclusions can be made from this figure. First, the temperature difference between the surface of the sample and the bulk melt, due to the alumina dissolution, does not influence the dissolution rate, due to the presence of

forced convection around the sample (see flow description). Therefore, this curve has been retrieved from Figure 4.10 for clarity. Second, the exponent of the Nusselt number sum (eq. 4.21) has a negligible influence on the quality of the correlation after a value of 3. This is easily understood when you keep in mind that an exponent of 3 is more suitable for a vertical flow. Moreover, this summation is intended for different flows that directly affect the sample. In the experimental setup of this work, the bubbles agitate the melt around the sample, as shown in Figure 4.4. Then, the effect of the bubble agitation and its addition to the model, while important to consider, should be investigated more deeply. The last and primary conclusion is that an adequate description of the flow around the sample is essential to obtain an accurate model. The change in any of the two other assumptions (the emissivity of the system and the relative value of the speed to its maximum value) can easily lead the model to rapidly diverge. Here, the value presented in the method section is in good accordance with the maximum accuracy that we can achieve, suggesting that the description of the flow in the crucible was accurate enough for this work.

4.5.3 INDUSTRIAL APPLICATION

In an electrolysis cell, the dissolution conditions are indeed different from those presented in this work. The flow pattern can be very different, the bubbles have a larger diameter, thus accordingly enhancing the dissolution, and the alumina is in a powder form floating on the bath instead of a disc immersed in the electrolyte. Nevertheless, the work presented here is still of good interest. It shows that the Sherwood number formulation can be used to estimate the dissolution rate of alumina in cryolite melts, which require adequate diffusivity for alumina. In this way, the description of the diffusivity by the Wilke-Chang equation is a convenient tool to assess the influence of

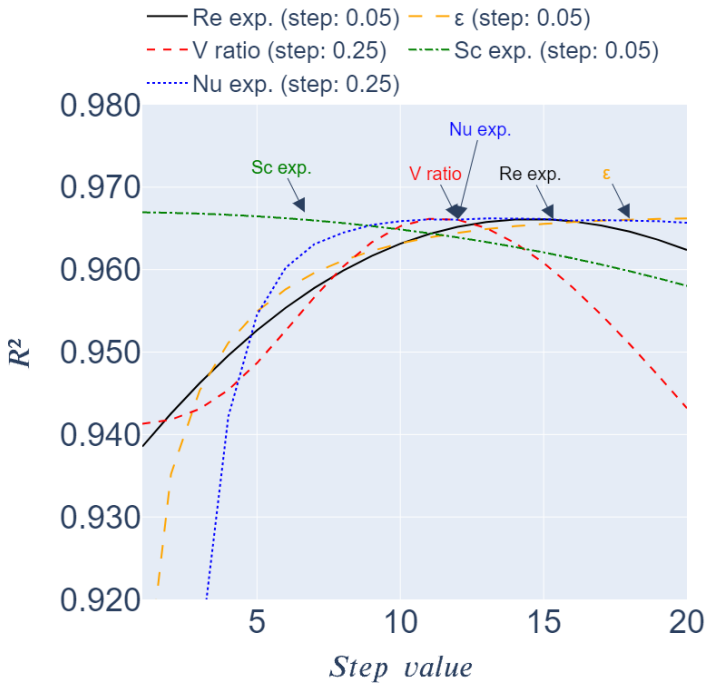

Figure 4.10 : Influence of the assumptions on the correlation coefficient between the observed data and the logarithmic model. X-axis represents the range for the sensitivity analysis. The value of the steps for each parameter is described in the legend.

the fluid properties on the dissolution of alumina and use it in the Schmidt number to find the Sherwood number. The choice of the adequate Sherwood formulation, however, is inherent to the flow pattern and the adequate description of the Reynolds number. The addition of the different sources of convection, as presented in this work, allows for a simple expression of the Reynolds and Sherwood numbers and makes comparison between different cases easier.

The main difference will come from the form of the alumina, which is a powder in electrolysis cells instead of a non-porous surface as in the usual Sherwood formulation. The cold powder injected will rapidly form a floating raft due to the thermal effect [82]. Once the raft is formed, sintering will occur between the alumina grains which

will ensure the structural integrity once the bath is remelted. At this moment, the raft will behave as a porous plate at the surface of the melt. The diffusion of the dissolved alumina through the pore will drive the dissolution rate of the entire raft. Therefore, an effective diffusion of the alumina should be used in the Sherwood formulation to estimate the dissolution rate of the main raft. As the dissolution occurs, smaller pieces of the raft will also disintegrate from the main raft and enhance its effective dissolution.

The dissolution of the small pieces that disintegrate from the main raft can be estimated with the work presented here. These small pieces will have a behavior similar to that of the disc in the experimental work presented. The main flow around the small pieces will come from the relative displacement of the fluid around the sinking piece. Also, bubbles that cross the path of the sinking piece will enhance the dissolution of the alumina. Therefore, the model presented in this work can be directly applied to the disintegrated part of the raft.

4.6 CONCLUSION

To describe the dissolution of solid discs in different cryolite melts, a gravimetric apparatus was used to perform the required tests of a parametric study. With the results obtained, a generic mass transfer model similar to that of a flat plate in perpendicular flow was used to predict the alumina dissolution rate. This analysis needed a strong description of the flow pattern around the sample to compute the adequate Reynolds number. In addition, the Schmidt number benefited from the Wilke-Chang equation to determine the molecular diffusivity in different melt compositions. The Wilke-Chang equation also highlighted the presence of three diffusion mechanisms related to the anions created during the dissolution. With this information, the Sherwood number for each sample has been used to accurately predict the alumina dissolution rate with the

following equation:

$$Sh = 0.6Re^{0.767}Sc^{\frac{1}{3}}$$

This equation allows taking into account the variations of the bath chemistry to compute the dissolution rate of the piece obtained from the disintegration of alumina raft in electrolysis cells.

4.7 ACKNOWLEDGEMENT

The authors want to thank Rio Tinto, the Natural Sciences and Engineering Research Council of Canada, and the Fonds de Recherche Nature et Technologies of Quebec for their technical and financial support for this project.

4.8 POST PUBLICATION REFINEMENT

4.8.1 BATH PROPERTIES

To determine the dissolution conditions of the alumina discs, it is important to measure accurately the properties of the bath. These properties depend on the composition of the bath. To obtain the property values, empirical relations have been used. These relations are easily available in the literature. From the mass fraction of the additives and the superheat, it is possible to obtain the density (Kvande et al. [103]), the viscosity (Hertzberg [104]), the liquidus temperature (Solheim et al. [92]) the alumina solubility limit (Skybakmoen et al. [116]), the surface tension (Daněk et al. [117]) and the thermal conductivity (Khokhlov [105]). Other authors also propose such relations from thermodynamic calculations, such as Robelin and Chartrand [96].

For this purpose, additives were carefully weighed to obtain the desired mass fraction in the melt used to dissolve 5 to 6 discs. However, some adjustments to the expected mass fraction in the melt were needed. The base components, cryolite and aluminum fluoride, were stored in contact with the atmosphere in the laboratory. Therefore, oxidation of these components occurred until an equilibrium state. This oxidation impurities was accounted in the form of added alumina in the melt. It was then needed to increase the amount of the cryolite and aluminum fluoride content to obtain the desirable composition. Also, aluminum fluoride evaporates over time from the crucible. To overcome this situation, bath samples were taken during a test to analyze their composition and adjust the composition for each alumina disc. Moreover, the alumina content of the bath increased from the dissolution of the preceding disc. The alumina mass fraction for each alumina disc is then increased from disc to disc accordingly. The last property that varies over time is the temperature of the bulk bath.

This temperature is measured at 30 mm from the bottom of the crucible, as presented in Figure 4.3 and 4.5. These variations lead to slight differences in the temperature measured, and the diffusivity calculated for each alumina disc and reported in Figure 4.7.

The change in the composition and the temperature will influence the movement ability of the molecules in the liquid. This will indeed influence the proportion between the movement of the molecule and the driving force of this movement [111]. The viscosity is used when the movement is provoked by a pressure difference in the liquid. However, when this movement is initiated by a concentration gradient, the diffusivity is then used. This is why relations such as the Wilke-Chang and the Stokes-Einstein equations use the viscosity of the liquid to estimate the diffusivity of molecules.

4.8.2 FLOW CONDITIONS

The flow around the samples also needs an adequate formulation. The dissolution of a sample is strongly related to the flow pattern around it and the surface available for the mass exchange. Correlations relations to find the Nusselt and Sherwood numbers exist between the most common geometry and flow patterns but need to be found for other situations, such as the one presented in this article. In the case presented here, the flow around the sample is perpendicular to a finite disc of negligible thickness and thus needs its specific formulation as presented in the article. This flow is created by the thermal exchanges of the liquid with its surrounding environment, the bubbling, and, in a limited proportion, from the dissolution of the sample.

For the influence of the bubbling, note that the bubbles were introduced in the experimental setup from the bottom of the crucible around the sample. A horizontal

distance, sufficient to avoid the accumulation of gas under the sample, was necessary to obtain the desirable influence of the bubbling, without introducing too much noise on the sample weight signal. The work of Park [109] was used to estimate that influence, as described in the article. However, a relation, presented in equation 4.27, can be of interest to further improve the effect of the bubbles on the flow. This relation between the Reynolds number, the Eotvos number, and the shape of the bubble presented by Park [109] also uses the Morton number (eq. 4.28) and a factor for the gas internal circulation (f_{sc} presented in eq. 4.29).

$$Re = \frac{1}{\sqrt{f_{sc}^2 \left(\frac{144M}{Eo^3} + \frac{Mo^{5/6}}{0.14425^2 Eo^{5/2}} \right) + \frac{Mo^{1/2}}{Eo^{1/2}(2.14+0.505Eo)}}} \tag{4.27}$$

$$Mo = \frac{g\mu^4}{\rho\sigma^3} \tag{4.28}$$

$$f_{sc} = 1 + \frac{0.5}{1 + e^{\frac{\log Eo + 1}{0.38}}} \tag{4.29}$$

[78] A. Solheim and E. Skybakmoen, "Mass-and heat transfer during dissolution of alumina," in *Light Metals 2020*. Springer, 2020, pp. 664–671.

[79] J. Thonstad, A. Solheim, S. Rolseth, and O. Skar, "The dissolution of alumina in cryolite melts," in *Essential Readings in Light Metals*, 1988, pp. 105–111.

[80] K. Miyabe and R. Isogai, "Estimation of molecular diffusivity in liquid phase systems by the wilke-chang equation," *Journal of Chromatography A*, vol. 1218, no. 38, pp. 6639–6645, 2011.

[81] L. Dion, "Modelisation of perfluorocarbon emissions based on the alumina distribution and local current density in an aluminium electrolysis cell," Ph.D. dissertation, Université du Québec à Chicoutimi, 2018.

[82] L. I. Kiss, "Alumina dissolution - a critical step in aluminum electrolysis," in *TMS 2018*, 2018, Conference Proceedings.

[83] K. Grjotheim, *Introduction to aluminium electrolysis: understanding the Hall-Hérloult process*. Aluminium-Verlag, 1993.

[84] J. Thonstad, F. Nordmo, and J. Paulsen, "Dissolution of alumina in molten cryolite," *Metallurgical and Materials Transactions B*, vol. 3, no. 2, pp. 407–412, 1972.

[85] J. Gerlach, U. Hennig, and K. Kern, "The dissolution of aluminum oxide in cryolite melts," *Metallurgical and Materials Transactions B*, vol. 6, no. 1, pp. 83–86, 1975.

[86] Z. Lubyová and V. Danek, "Control mechanism for alumina dissolution in cryolite melts," *Chemical Papers*, vol. 49, no. 2, pp. 59–63, 1995.

[87] R. Haverkamp, B. Welch, and J. Metson, "The influence of fluorination on the dissolution rate of alumina in smelter electrolyte," in *Light Metals - Warrendale*, 1994, pp. 365–365.

[88] J. Alarie, L. I. Kiss, S. Poncsák, R. Santerre, S. Guérard, and J. F. Bilodeau,

"Influence of additives on alumina dissolution in superheated cryolite melts." in *TMS 2021*. Springer, 2021, pp. 533–540.

[89] J. Alarie, L. I. Kiss, L. Dion, M. Truchon, R. Santerre, S. Guérard, and J.-F. Bilodeau, *Empirical prediction of alumina dissolution rate in a cryolitic melt: comparison with the existing literature.* Springer, 2022, pp. 349–356.

[90] J. Alarie, T. Roger, L. I. Kiss, S. Poncsák, S. Guérard, and J.-F. Bilodeau, "Validation of the gravimetric method to properly follow alumina dissolution in cryolitic bath," in *Light Metals 2020*. Springer, 2020, pp. 680–687.

[91] L. Kiss and S. Poncsák, "Effect of the bubble growth mechanism on the spectrum of voltage fluctuations in the reduction cell," in *Essential Readings in Light Metals*, 2002, pp. 402–408.

[92] A. Solheim, S. Rolseth, E. Skybakmoen, L. Støen, Å. Sterten, and T. Støre, "Liquidus temperatures for primary crystallization of cryolite in molten salt systems of interest for aluminum electrolysis," *Metallurgical and Materials Transactions B*, vol. 27, no. 5, p. 739, 1996.

[93] K. Machado, "Chimie des bains pour l'electrolyse de l'aluminium: Étude rmn haute température et modélisation," Ph.D. dissertation, Université d'Orléans, 2017.

[94] Y. A. Cengel and A. J. Ghajar, *Heat and mass transfer : fundamentals & applications*, 5th ed. New York, N.Y.: McGraw-Hill Education, 2015.

[95] C. Robelin and P. Chartrand, "A density model based on the modified quasichemical model and applied to the naf-alf3-caf2-al2o3 electrolyte," *Metallurgical and Materials Transactions B*, vol. 38, no. 6, pp. 881–892, 2007.

[96] C. Robelin and P. Chartrand, "A viscosity model for the (naf + alf3 + caf2 + al2o3) electrolyte," *The Journal of Chemical Thermodynamics*, vol. 43, no. 5, pp. 764–774, 2011.

[97] A. E. Gheribi, S. Poncsák, R. St-Pierre, L. I. Kiss, and P. Chartrand, "Thermal conductivity of halide solid solutions: Measurement and prediction," *Journal of*

Chemical Physics, vol. 141, no. 10, 2014.

[98] A. E. Gheribi, M. Salanne, and P. Chartrand, "Formulation of temperature-dependent thermal conductivity of naf, β-na 3 alf 6 , na 5 al 3 f 14 , and molten na 3 alf 6 supported by equilibrium molecular dynamics and density functional theory," *The Journal of Physical Chemistry C*, vol. 120, no. 40, pp. 22 873–22 886, 2016.

[99] J. R. Welty, *Fundamentals of momentum, heat, and mass transfer*, 4th ed. New York: J. Wiley, 2001.

[100] J. P. Holman, *Heat transfer*, 7th ed. New York: McGraw-Hill, 1990.

[101] C. F. Hess and C. W. Miller, "Natural convection in a vertical cylinder subject to constant heat flux," *International Journal of Heat and Mass Transfer*, vol. 22, no. 3, pp. 421–430, 1979.

[102] R. B. Bird, E. N. Lightfoot, and W. E. Stewart, *Transport phenomena*, 2nd ed. New York ;: Wiley, 2007.

[103] H. Kvande and H. Rørvik, "Influence of bath density in aluminum electrolysis," *Journal of Metals*, vol. 36, pp. 62–62, 1984.

[104] T. Hertzberg, K. Tørklep, and H. Øye, "Viscosity of molten naf-alf3-al2o3-caf2 mixtures: Selecting and fitting models in a complex system," in *Essential Readings in Light Metals*. Springer, 1980, pp. 19–24.

[105] V. A. Khokhlov, E. Filatov, A. Solheim, and J. Thonstad, "Thermal conductivity in cryolitic melts-new data and its influence on heat transfer in aluminum cells," in *Light Metals 1998)*, 1998, pp. 501–506.

[106] J. Thonstad, *Aluminium electrolysis : fundamentals of the Hall-Héroult process*, 3rd ed. Düsseldorf: Aluminium-Verlag, 2001.

[107] V. D.-G. V. u. Chemieingenieurwesen, *VDI heat atlas*, 2nd ed. Berlin ;: Springer, 2010.

[108] Y. Park, A. Lamont Tyler, and N. de Nevers, "The chamber orifice interaction in the formation of bubbles," *Chemical Engineering Science*, vol. 32, no. 8, pp. 907–916, 1977.

[109] S. H. Park, C. Park, J. Lee, and B. Lee, "A simple parameterization for the rising velocity of bubbles in a liquid pool." *Nuclear Engineering and Technology*, vol. 49, pp. 692–699, 2017.

[110] F. Risso, "Agitation, mixing, and transfers induced by bubbles," *Annual Review of Fluid Mechanics*, vol. 50, pp. 25–48, 2018.

[111] J. O. Hirschfelder, C. F. Curtiss, and R. B. Bird, *Molecular theory of gases and liquids*, ser. Structure of matter series. New York: J. Wiley & Sons, 1967.

[112] C. R. Wilke and P. Chang, "Correlation of diffusion coefficients in dilute solutions," *AIChE Journal*, vol. 1, no. 2, pp. 264–270, 1955.

[113] B. Glorieux, F. Millot, J. C. Rifflet, and J. P. Coutures, "Density of superheated and undercooled liquid alumina by a contactless method," *International Journal of Thermophysics*, vol. 20, no. 4, pp. 1085–1094, 1999.

[114] C. Shi, O. Alderman, D. Berman, J. Du, J. Neuefeind, A. Tamalonis, J. K. R. Weber, J. You, and C. Benmore, "The structure of amorphous and deeply supercooled liquid alumina," *Frontiers in Materials*, vol. 6, 2019.

[115] H. Kvande, "The structure of alumina dissolved in cryolite melts," in *Essential Readings in Light Metals*, 1986, pp. 96–104.

[116] E. Skybakmoen, A. Solheim, and Å. Sterten, "Alumina solubility in molten salt systems of interest for aluminum electrolysis and related phase diagram data," *Metallurgical and materials transactions B*, vol. 28, no. 1, pp. 81–86, 1997.

[117] V. Daněk, O. Pataraák, and T. Østvold, "Surface tension of cryolite-based melts." *Canadian Metallurgical Quarterly*, vol. 34, no. 2, pp. 129–133, 1995.

CHAPTER V
FUNDAMENTAL MASS TRANSFER CORRELATIONS BASED ON EXPERIMENTAL AND LITERATURE DATA.

5.1 SYNOPSIS

5.1.1 OBJECTIVES

This article contributes to the objectives 1 to 3 of the thesis. The contributions are as follows:

1. The applications of the general mass transfer theory apply to the dissolution of alumina powder injected in alumina.
2. The comparison of the results obtained in this work shows good agreement with those presented in the literature.
3. The adequate description of the flow pattern around the sample is of first importance to determine the dissolution rate of alumina.

5.1.2 SCIENTIFIC CONTRIBUTION

Previous article presented how the cryolitic bath composition affects the diffusivity of the alumina dissolved in cryolite. The study was made on solid discs of alumina under specific conditions. Before pushing forward this work, the article presented here tries to apply the knowledge created to data from the literature. The following work achieves three main objectives.

First, it compares the results obtained with our gravimetric method to data available in the literature. The different methods used in the literature make it difficult to compare the results obtained from the different works used for comparison in this article. The results are often presented as the required time to achieve the complete dissolution of the sample, instead of the dissolution rate. Nevertheless, the use of the diffusivity found in the previous article allows the use of the Sherwood number and a fair comparison of the different setups and samples. The results show a good agreement between our experimental data and those from the literature.

Second, the article proposes a convenient presentation of the results to compare the dissolution rates of different samples. The use of a general mass transfer equation allows the reduction of the difference between the experimental tests to two parameters. These parameters are the constants used in the formulation of the Sherwood number, as presented in the article.

Finally, the application of fundamental mass transfer theory on samples with different morphologies helped to develop our approach to the analysis of powder injection in cryolite. The main difference is that the solid discs were immersed in the cryolite and were in the middle of a downward flow of cryolite, perpendicular to the surface of the disc. The comparison with powder injection made in this article showed that the liquid flow is probably more parallel to the surface of the raft. In these cases, a mass transfer model exists for parallel flow to a flat plate and should be used in the case of a floating raft.

5.1.3 AUTHORS CONTRIBUTIONS

Work	Contributors
Direction	Prof. László I. Kiss and Prof. Lukas Dion
Design of the apparatus	Jonathan Alarie
Construction	Jonathan Alarie and Patrice Paquette
Experimental plan	Jonathan Alarie
Tests	Martin Truchon and Jonathan Alarie
Analysis	Jonathan Alarie
Writing	Jonathan Alarie
Revision	Prof. László I. Kiss and Prof. Lukas Dion
Technical Support	Sébastien Guérard and Jean-François Bilodeau

5.1.4 PUBLICATION

Authors	Jonathan Alarie, László I. Kiss, Lukas Dion, Sébastien Guérard, and Jean-François Bilodeau
Year	2023
Title	Fundamental mass transfer correlations based on experimental and literature data
Journal	TMS Light Metals
Status	Published (Reprint permission available in Appendix A.3)
Date	March 2023

5.1.5 RÉSUMÉ

À l'aide d'une description spécifique du transfert de chaleur et de la diffusivité, la théorie générale du transfert de masse est appliquée aux données disponibles dans la littérature pour identifier leur taux de dissolution respectif. Les calculs utilisant des données de la littérature sont ensuite comparés à des travaux expérimentaux effectués dans des conditions de laboratoire en utilisant une méthode gravimétrique pour évaluer la vitesse de dissolution de disques d'alumine. Le contraste entre les données de nos travaux expérimentaux et la validation fournie par la littérature est supposé inhérent à la morphologie de l'échantillon et à la description adéquate de l'écoulement qui l'entoure.

La discussion qui suit met en évidence les facteurs dominants affectant les coefficients de transfert de masse et identifie les défis théoriques à surmonter pour obtenir des relations plus précises pour les travaux futurs.

5.1.6 NOMENCLATURE

Parameter	Definition
a	Sherwood fitting coefficient
A	Area of contact
d	Diameter
D	Diffusivity
h_m	Convection mass transfer coefficient
L_c	Characteristic length
$\dot{m}$	Mass flow rate
m	Mass
Re	Reynolds number
Sc	Schmidt number
Sh	Sherwood number
U	Velocity
w	Mass fraction
Greek letters	**Definition**
θ	Angle of repose
ν	Kinematic viscosity
ρ	Density
ϕ	Mass flux
Subscript	**Definition**
∞	Bulk value
l	Value for the liquid
s	Surface value
Superscript	**Definition**
m	Reynolds fitting exponent
n	Schmidt fitting exponent

FUNDAMENTAL MASS TRANSFER CORRELATIONS BASED ON EXPERIMENTAL AND LITERATURE DATA.

Jonathan Alarie[a, b], László I. Kiss[a], Lukas Dion[a], Sébastien Guérard[c], Jean-François Bilodeau[c]

[a]GRIPS, University of Quebec at Chicoutimi, 555 Boul Universite, Saguenay, G7H 2B1, Quebec, Canada [b]REGAL, Aluminium Research Centre, 2325 Rue de l'Université, Québec, G1V 0A6, Quebec, Canada [c]Arvida Research and Development Centre, Rio Tinto, 1955 Mellon Boulevard, Jonquiere, G7S 4K8, Quebec, Canada

ABSTRACT

Using a specific description of the heat transfer and diffusivity, general mass transfer theory is applied to data available in the literature to identify their respective dissolution rate. The following calculations using data from the literature are then compared to experimental work performed under laboratory conditions using a gravimetric method to evaluate the dissolution rate of alumina disks. The contrast between the data from our experimental work and the validation provided by the literature is assumed inherent to the morphology of the sample and the adequate description of the flow around it. The following discussions highlight the dominant factor affecting the mass transfer coefficients and pinpoint the theoretical challenges to overcome to achieve more precise relations for future works.

Keywords: Aluminum electrolysis, Alumina dissolution, Cryolite properties

5.2 INTRODUCTION

Alumina dissolution in the Hall-Héroult process is a complex phenomenon that limits the uniformity of alumina distribution in industrial electrolysis cells. An uneven distribution may cause instability in the process that leads to undesired anode effects or to an increase of muck under the metal pad. In all cases, environmental and security issues, not to mention productivity, ask for increased comprehension of the alumina dissolution to prevent such problems. For this purpose, a study on the effect of the bath composition and temperature on the dissolution rate of solid discs has been conducted. The results of this experimental work, reproduced here, can be found in Alarie et al. [118] and represent the foundation of the present work. Basically, a mass transfer model for a flat plate in a perpendicular flow has been applied to describe the dissolution of the alumina discs. However, the sample structure used in this work is different from what is formed by an injection of alumina in electrolysis cells. It is well known that the alumina upon injection in the melt forms solid aggregates that are hard to dissolve. Then, the present work tries to apply the same analysis used for the solid discs to data from the literature, with different alumina raft structures.

For nearly 50 years, researchers tried to explain the parameters that influence the alumina dissolution rate. Despite the many names that could be mentioned here, only a few works are reported in this paper due to the lack of details available in the literature for the purpose of this work. The first one is the work of Jain et al. [119] who gave a good description of their experimental setup and dissolution curves over time. They tested the effect of a few chemical compositions, superheat, and alumina properties on the alumina dissolution behavior. With a similar experimental setup, Bagshaw et al. [120] tried to identify the effect of the alumina properties on the dissolution rate. Isaeva et al. [121] gave a few details on their experimental setup to describe the effect of the

alumina content in the bath and a few alumina properties. Finally, the work of Gerlach et al. [122] is of first interest because they studied pressed tablets (geometry similar to the solid discs) with different chemical compositions and alumina properties.

5.3 METHOD

Before applying the mass transfer model previously developed to the data from the literature, there are some points to mention :

1. To compare the dissolution rate obtained by Jain et al. [119] in their work to other authors, the average dissolution rate was used.

2. Where the authors studied the alumina properties, such as Gerlach et al. [122], Jain et al. [119], and Bagshaw et al. [120], the average dissolution rate that they observed for the same Reynolds number was used for comparison.

3. The dissolution rates measured by Isaeva et al. [121] are assumed to come from a stirred melt.

The next analysis relies on Colburn's analogy to apply dimensional analysis to the alumina dissolution (equation 5.1). Most of the concepts presented here can be easily taken from a general reference book on heat and mass transfer, such as Çengel et al. [123] and more details are available in Alarie et al. [118]. This kind of analysis needs a good description of the flow around the system studied and the fluid properties to find adequate Reynolds and Schmidt numbers (equation 5.2 and 5.3, respectively), that leads to the Sherwood number (equation 5.4) and the h_m mass transfer coefficient (equation 5.5). These relations require the use of the fluid velocity (U_l), the characteristic length of the sample (L_c), the melt kinematic viscosity(ν), the diffusivity of the alumina

in the melt (D) and finally, the concentration gradient ($w_s - w_\infty$), expressed here in mass fraction instead of the common weight percent. Since this information is mostly unavailable from all considered authors, the following assumptions were made :

1. Tests are assumed to have been conducted in round crucibles with perfect insulation on the bottom face, the radiative heat input from the sides, and pure radiative heat loss from the top.

2. The stirring of the melt, unless otherwise specified, should create a flow with a velocity of about 10 cm/s.

3. In stirred melt, the diameter of the stirrer is one-fifth of the crucible diameter.

4. Powder injection creates a raft that has a conical shape, with an equivalent circle diameter as the characteristic length. This length is assumed to stay the same all over the dissolution time studied.

$$\phi\left[\frac{kg}{m^2 s}\right] = \frac{\dot{m}}{A} = h_m \rho (w_s - w_\infty) \tag{5.1}$$

$$Re = \frac{U_l L_c}{\nu} \tag{5.2}$$

$$Sc = \frac{\nu}{D} \tag{5.3}$$

$$Sh = a Re^m \cdot Sc^n \tag{5.4}$$

$$Sh = \frac{h_m L_c}{D} \tag{5.5}$$

These assumptions were used to calibrate the parameters of the physical relationship (such as U_l and L_c) between the experimental setup and the dissolution rate, such as to choose between the use of the diameter or the radius.

One of the important information in such analysis is the contact area between the raft and the melt. Without a deep knowledge of the geometries involved in the tests performed by other authors; the following simplification was made. The raft is considered to have a conical shape with an angle of repose (θ) of 4° as presented in Figure 5.1. Experimental observation of the shape of the heap formed by the injected particles on the surface of a liquid can be as small as 2°. Also, Roger et al. [124] observed angles around 4° in an analog model of organic grains injected into water. In perfect conditions, the diameter of such a raft (d) can then be approximated with equation 5.6, the value used in this work. This relation relies on the geometric proportionality of the injected volume of alumina, obtained by the injected mass (m) and its assumed bulk density (ρ), and the diameter of the cone obtained. However, it is also important to mention that the inner diameter of the crucible limits the maximal diameter of the raft. For the subsequent analysis, the diameter found with equation 5.6 will be used as the characteristic length for most of the calculations involved. Another issue with this assumption is that the diameter of the raft changes over time with the dissolution. Ideally, such behavior must be tracked, reducing the characteristic length and the contact area between the melt and the sample. Unfortunately, the information needed to do this update throughout the whole dissolution is mostly unavailable. Also, it can be cumbersome to track the contact area of a dissolving raft. Then, the initial diameter of the raft has been chosen as a reference in the present analysis. Thus, the dissolution rate found with the model presented in this work should be slightly below the real dissolution

rate in the first moment of the dissolution and slightly above at the end. However, the average dissolution rate will be well represented by the model.

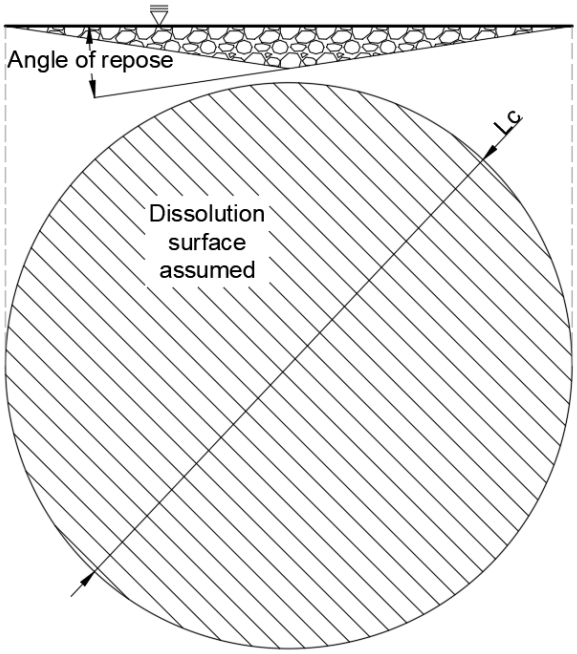

Figure 5.1 : Sketch of the conical raft assumption to obtain the surface of contact and the characteristic length of the dissolution process.

$$d = \sqrt[3]{\frac{24m}{\rho\pi tan\theta}} \tag{5.6}$$

To calculate the Reynolds number, it is important to know the internal properties of the liquid. Most of the publications presented above try to relate the dissolution rate to the mass fraction of the additives in the melt. However, the dissolution process is too complex to be described by linear relations with the content of the additives. So, the use of the fluid properties integrates the interactions between the additives and their non-linear behavior. Fortunately, relations between the composition and the melt

dynamic viscosity (μ, Hertzberg et al. [125]), density (ρ, Kvande and Rørvik [126]), cinematic viscosity ($\nu = \mu/\rho$), and alumina solubility (w_s, Skybakmoen et al. [127]) are easily available in the literature. Once the material properties of the bath are known, the convection in the melt needs to be described. There are four sources of convection identified in the different experimental setups :

1. Natural convection caused by concentration gradients.
2. Natural convection caused by thermal gradients.
3. Bubbling (special forced convection).
4. Forced convection.

It is important to mention here that the real flow in contact with the sample needs to be precisely known to accurately describe the convective dissolution. However, the different works that studied the dissolution of the alumina hardly mention the flow pattern in the experimental setup and barely less their dimensions. So, without a detailed knowledge of the different flow patterns, the following analysis will be considered for comparison purposes only. The first two sources of convection are mostly negligible in the works with stirred melt. The third source applies only to the work with solid discs. These convection sources are detailed in Alarie et al. [118] and are neglected in this analysis.

The last source of convection is the stirring involved in some experimental setups. Most authors considered adding stirring to an intensity similar to that seen in industrial cells, which is estimated to few tenths of a meter per second (See Perron [128] and Kobbeltvedt and Moxnes [129]). To obtain the Reynolds number associated with such

stirring, the velocity of the fluid is required. So, with the help of the diagram in Jain et al. [119], the diameter of the stirrer was estimated of a fifth of that of the crucible. This value seems coherent from one paper to another, since there is not much physical space in a crucible for a larger stirrer, and a smaller one will require higher rotation speed to achieve the desired stirring. In a related matter, the information provided by Isaeva et al. [121] on her experimental setup does not include any input on the design of stirring. In that case, it was assumed that the stirrer has a rotation speed of 200 rpm, just like the one used by Jain et al. [119] and Bagshaw et al. [120]. Note that the design of the stirrer can be very different from one author to the other, and they can provide different stirring patterns. So, the results of Isaeva et al. [121] are here used to confirm that the assumptions made with the works of Jain et al. [119] and Bagshaw et al. [120] are reasonable. To obtain the velocity of the melt, the rotation speed was used in concert with the radius of the stirrer. The velocity obtained from this method gives congruent results with every author with values between 9.4 to 20.9 cm/s. Now, using equation 5.2 with the diameter of the raft as the characteristic length, the Reynolds number for the convection source can be obtained.

The Reynolds number is used to describe the ratio of the inertial forces on the viscous forces in the fluid [123] that interact with the sample. This relationship is reflected by the amplitude of the Reynolds number and its exponent in the Sherwood number equation (5.4). In the case of stirred melt, as presented by most of the authors, the Reynolds number is under 5×10^5, suggesting a laminar flow around the samples. As shown in Hess et al. [130], the flow in a heated round crucible rises along the wall of the crucible then it turns downward in the center. Even with stirring, the melt is assumed to follow a similar flow pattern. In these conditions, the model of a flat plate

perpendicular to the flow, with an exponent of 0.748 as described in Alarie et al. [118], will be used for all authors.

Once the flow pattern has been considered, the Schmidt number (equation 5.3) will dictate the fluid properties' influence on the mass transfer in the medium. Its value characterizes the relative thickness of the velocity boundary layer over the diffusive boundary layer. So, with the viscosity and the diffusivity found in Alarie et al. [118], it is possible to find the Schmidt number for every data point. The Schmidt number usually comes with an exponent of $\frac{1}{3}$ from the exact analysis of the boundary layer, as presented by Blasius and Pohlausen, in Welty [131]. This leads the analysis to the complete description of the Sherwood number, except for the coefficient (a) in equation 5.4. This coefficient is found from experimental data in the next section.

5.4 RESULTS

From the theoretical analysis presented above, the experimental dissolution rate was predicted by the Sherwood number using equation 5.1 to 5.5. Note that the coefficient "a" in the Sherwood formulation (equation 5.4) is found with the help of the regression lines presented in Figure 5.2.

Figure 5.2 shows a good accordance between the model and the observed dissolution rates for each author. However, differences can be seen from one author to another. As explained above, the conditions in which the tests were performed are of first importance in these differences. For example, an increase in the stirring or in the diameter of a sample (the characteristic length) will drag the results to the right, thus lowering the coefficient needed to predict the dissolution rate. These causes explain the differences between the data from Isaeva et al. [121] and the other injections performed by Jain et

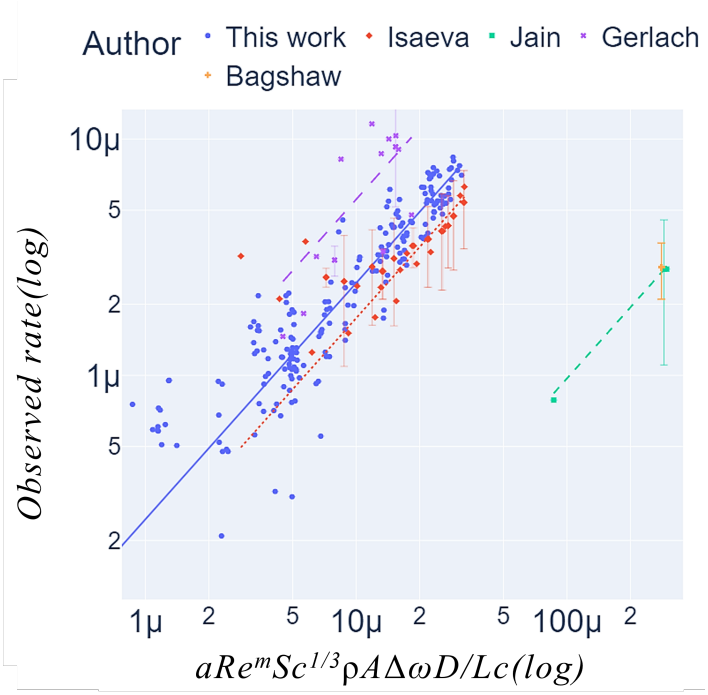

Figure 5.2 : Correlation between the observed dissolution rate values (vertical axis), and the one predicted by the mass transfer theory (horizontal axis). The error bar represents the amplitude of variation of the dissolution rate caused by the alumina properties, not taken into account in the model of this work. The lines are the predictions of the model for the data from this work (solid), Isaeva et al. [121] (dot), Jain et al. [119] (dash) and Gerlach et al. [122] (long dash).

al. [119] and Bagshaw et al. [120], the last two of them using the same experimental method. As stated in the method description, it is difficult to compare the results obtained by different methods, without a deep knowledge of the flow pattern of the melt and the shape of the sample. Here, the assumption made for the stirring in the crucible seems to differ from the reality of the tests of Jain et al. [119] and Bagshaw et al. [120] Though, assuming that these unknowns are fulfilled, the model presented here proved to be able to adequately predict the dissolution rate of powder injection.

It is very relevant to mention that one of the questions that many authors studied, such as Isaeva et al. [121], Gerlach et al. [122], Jain et al. [119], and Bagshaw et al.

[120], is the influence of the alumina properties on the dissolution rate. As it can be seen in Figure 5.2, the model presented here cannot take these parameters into account, as represented by the error bar in the figure. Still, the influence of the bath's internal properties, inherent to its composition and superheat, is larger than most of the alumina properties variations observed by the cited authors, as depicted by the data from this work.

From Figure 5.2 it can also be seen that the results obtained by Isaeva et al. [121], Gerlach et al. [122] and this work gives a fairly similar correlation. This means that the geometries and flow patterns involved in these works are similar to each other, or at least that the differences compensate for the difference in behaviors. These differences include the roughness of the surface of the injected raft compared to the smooth surface of a disc or a pressed tablet of alumina.

5.4.1 SENSITIVITY STUDY

For added confidence in the previous model, a sensitivity analysis was performed on the results from the literature. This analysis shows the influence of the assumed parameters on the correlation coefficient between the model and the different authors and different forms (powder or pressed tablets). Table 5.1 shows the parameter's amplitude of variation. Parameters that influence only the natural convection are neglected since all powder injections were assumed to be made with a similar stirring. The influence of the variation of the parameters is shown in Figure 5.3.

Table 5.1 : Range of the sensibility study of the model

Parameter	Minimum	Maximum	Reference
Reynolds exponent (m)	0.05	1	0.748
Crucible-to-stirrer (diameter ratio)	1	20	5
Angle of cone (°)	1	10	4
Bulk powder density ($\frac{kg}{m^3}$)	950	1150	1000

5.4.2 CORRELATION ACCURACY

From the data of Isaeva et al. [121], and Gerlach et al. [122], it can be seen that the assumptions have a minimal effect on the correlation coefficient between their experimental data and the proposed model. For Isaeva et al. [121], this is easily explained by the small size of the raft created compared to the crucible used. In the case of Gerlach et al. [122], since they used compressed tablets of alumina, only the Reynolds exponent and the crucible-to-stirrer ratio are considered, and they do not have a significant influence. On the other hand, the data from Jain et al. [119], presented as an example in Figure 5.3, show a slight dependence on the parameter's value. Despite the very small change in the values of the correlation coefficient, these dependencies can help to find better values for the parameters. That is the case for the Reynolds number exponent and the cone angle. The Reynolds number exponent seems to reach an optimum accuracy near 0.748, which is expected if the flow around the sample corresponds to the assumption previously made. However, the rafts, as created by Jain et al. [119], are in theory still touching the walls of the crucible with an angle below 4°, explaining the constant value of the correlation coefficient up to this value. Increasing

the angle of the cone to prevent the raft from touching the wall brings the angle near 8°, while the optimum in Figure 5.3 is near 6°. This modification also changes the value of the best fitting exponent which is now about 0.5 for a 6° angle. This result suggests a dissolution behavior more like a flat plate with a parallel flow instead of a perpendicular one. Changing the exponent of the Reynolds number in the Sherwood equation (eq. 5.4) from 0.748 to 0.5 and running another sensitivity study, shows that the most likely angle should be 8°, the angle at which the raft stops touching the walls of the crucible. This behavior should indeed be an ideal scenario for a raft in an electrolysis cell. Also, as mentioned previously, the shape of the raft is strongly influenced by the injection method. This means that the scenario of a flat plate describing the data from Jain et al. [119] is more plausible. The last two parameters (the stirrer diameter and powder density) seem to have little effect on the variation of the correlation coefficient.

5.4.3 COEFFICIENT VALUE

The coefficient a in the Sherwood formulation (equation 5.4) is also influenced by the assumptions made in the method section, as presented as an example in Figure 5.4 from the data of Jain et al. [119]. As mentioned, two models in the mass transfer theory can represent an approximation target for the value of this coefficient; the model for a flat plate, with a coefficient of 0.664 ($0.664Re^{0.5}Sc^{1/3}$), and the one with a perpendicular flow to an infinite plate, with a coefficient of 0.257 ($0.257Re^{0.731}Sc^{1/3}$) (see Çengel et al. [123]). These values represent the maximum that could be achieved, if the sample behaves like a perfect plate and if the flow is adequately described by the exponent of the Reynolds number. For this reason and to keep good readability, Figure 5.4 is limited to the range from 0 to 0.5 for the coefficient a values. Also, a turbulent flow parallel to a flat plate, that is to say at a higher Reynolds number than that observed in this work,

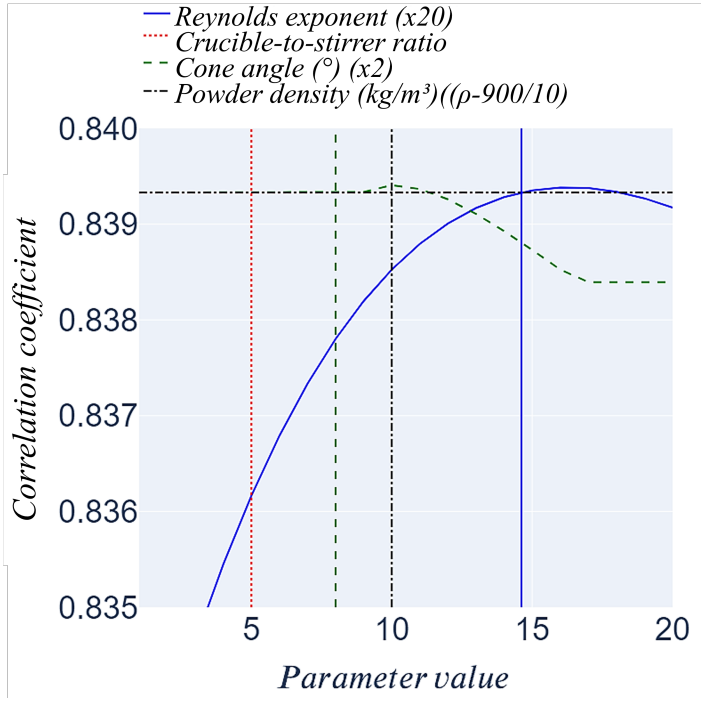

Figure 5.3 : Sensibility study of the assumption on the value of the correlation coefficient compared to the prediction using the Sherwood number formulation for the data from Jain et al. [119]. 20 different values for each parameter were tested. Vertical lines represent values from Table 5.1.

will see its coefficient to be around 0.037 ($Sh = 0.037 Re^{0.8} Sc^{\frac{1}{3}}$, see Çengel et al. [123]). This case is not considered in this work, and thus the coefficients observed should be above this other limiting value.

The most sensitive parameter for the coefficient value is the exponent associated with the Reynolds number, as predicted in the mass transfer theory. A change in the flow pattern and in the intensity of the turbulence is indeed a strong factor that modifies the dissolution behavior of a sample, and thus the coefficient of the Sherwood number formulation. Therefore, the value of the Reynolds number exponent should be selected from a deep knowledge of the flow pattern around the sample. From Figure 5.4, it can

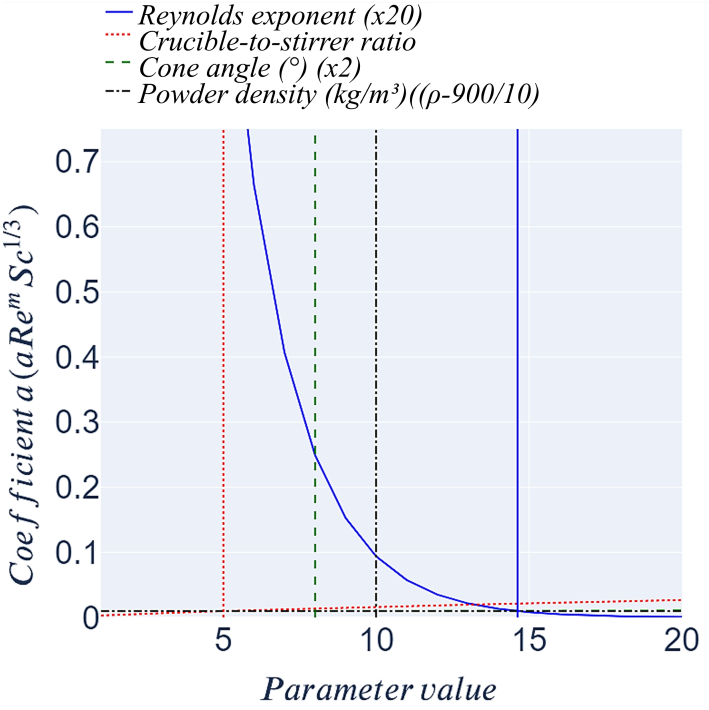

Figure 5.4 : Sensibility study of the assumption on the value of the coefficient "a" in the Sherwood number for the data from Jain et al. [119]. 20 different values for each parameter were tested. Vertical lines represent values from Table 5.1. 0.75 represent the highest plausible value (see text).

be seen that the value fixed for the different parameters allows the coefficient to be within the limits identified above. The sole exception comes from the data from Gerlach et al. [122], which show a higher value than the expected 0.257. However, the use of fragile samples, such as compressed tablets of alumina, can favor the disintegration of the sample and thus easily explain this result. The second more sensitive parameter is the crucible-to-stirrer diameter ratio, which directly changes the velocity of the fluid. As this ratio increases, the diameter of the stirrer decreases, and thus the velocity of the fluid. This will lower the Reynolds number and a greater coefficient in the Sherwood formulation will be needed to fit the data. However, as stated in the method section, a

stirrer of one-fifth of the crucible diameter at 200 rpm should give melt velocity in the order of 10 cm/s and represent a plausible value.

The last two parameters, the powder density and the angle of the conical raft have weak effects on the coefficient since their variation range does not affect much the diameter of the raft, with less than 10 % of variation between the limits studied. Also, while the raft is touching the wall, a change in the density of the powder or the angle has no influence on the diameter of the raft, unless they lower the volume of the raft to the point that the side of the raft cannot touch the wall of the crucible.

This analysis confirms the adequacy of most of the assumptions and the model used to predict the alumina dissolution rate, since it gives the best possible correlation. Only the conical angle should be modified from 4° to 8° and the data from Jain et al. [119] and Bagshaw et al. [120] benefit from a parallel flow model. The results of this modification are shown in Figure 5.5, where the exponent of the Reynolds number in the Sherwood formulation (eq. 5.4) for the data from Jain et al. [119] and Bagshaw et al. [120] is set to 0.5.

Once the model is well-defined, it is possible to see the effect of some parameters on the output of the model. Figure 5.6 shows the effect of the augmentation of the convection and characteristic length on the Sherwood number value through the Reynolds number. As the Reynolds number increases, usually due to its correlation with fluid velocity, the Sherwood number will also slowly increase. However, the Reynolds number can also be increased following an augmentation of the characteristic length. These two parameters are foremost inherent to the electrolysis cell design from which the melt and bubble velocity depend. Next, the injector design can largely influence the shape of

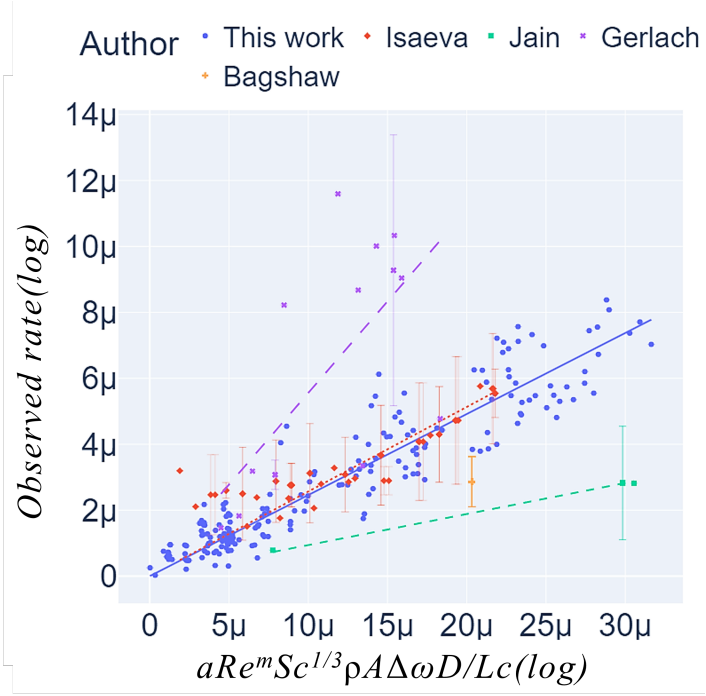

Figure 5.5 : Correlation between the observed dissolution rate values and the revised model. The lines are the predictions of the model for the data of this work (solid), Isaeva et al. [121] (dot), Jain et al. [119] (dash) and Gerlach et al. [122] (long dash).

the raft and thus its characteristic length. On the other hand, the dynamic viscosity of the bath is more a consequence of the bath composition and temperature than set at a desired value. In every case, Figure 5.6 represents a valuable tool to compare the results from the different sets of data used in this work, which have different stirring values. This figure also presents that the chosen idealized case represented by the parallel flow above a flat plate is sufficiently accurate to describe the alumina dissolution rate under a different set of conditions. However, to satisfy this ideal/perfect model, it is necessary to accurately describe the evolution of the surface area over the lifetime of the raft. Along with the measure of the dissolution rate at each instant, it is expected that the pairing of the instantaneous surface and dissolution rate will indeed follow a flat plate

model with parallel flow. Since the information about the instantaneous raft surface is unavailable, the analysis here represents the average dissolution rate over the initial surface of contact. Then, it is natural that the dissolution rates predicted are different from those of the ideal/perfect model. Also, as mentioned in Alarie et al. [118], the flow pattern perpendicular to the raft, with an exponent of 0.748, is similar to that of a piece of raft sinking in the melt, and thus the dissolution rate in this case is higher than with a flat plate in parallel flow.

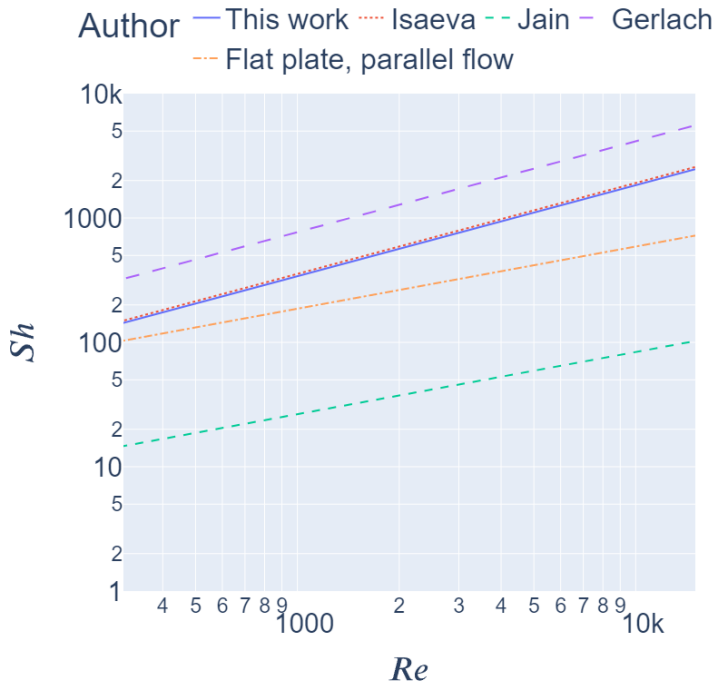

Figure 5.6 : Variation of the Sherwood number with the Reynolds number as predicted by the model obtained from the data of each author. Dash dot line from Çengel et al. [123], dash line from Jain et al. [119], dot line from Isaeva et al. [121], long dash from Gerlach et al. [122] and solid lines from this work.

5.5 CONCLUSION

In this work, a fundamental analysis of mass transfer based on data from experimental tests has been applied to other data from the literature. The results obtained show that the model previously developed for a perpendicular flow to the sample surface can describe most of the dissolution behaviors observed. However, at higher Reynolds numbers, a model using a parallel flow over a flat plate is more suitable to predict the dissolution rate.

Also, the model demonstrated the strong sensitivity of the results to the description of the flow around the sample and the sample itself. Namely, the pattern of the flow and the characteristic length are of first importance to accurately find the dissolution rates of the sample. A sensitivity study of the flow pattern to the bath's internal properties should be part of every dissolution study. Also, special consideration should be taken to prevent the raft from reaching the wall of the crucible and minimize its proximity in future experimental work. Finally, the models presented here describe the mean dissolution rate of the sample involved. The analysis of the Sherwood number and its relation to the raft surface of contact at each instant should give results closer to the mass transfer theory over a flat plate with a parallel flow.

5.6 ACKNOWLEDGEMENT

The authors want to thank Rio Tinto, the Natural Sciences and Engineering Research Council of Canada, and the Fonds de Recherche Nature et Technologies of Quebec for their technical and financial support for this project.

5.7 POST PUBLICATION REFINEMENT

5.7.1 FLOW CONDITIONS

The dissolution of a solid is strongly dependent to the flow pattern and conditions around it. Fortunately, performing tests of dissolution in a crucible tends to create a similar flow, with or without stirring. This is inherent to the geometry of the crucible, which is often a prism-like container with a round base (cylinder) or a squared or rectangular base. Nevertheless, the natural convection of the liquid contained in these crucibles will raise the liquid in contact with the walls, due to the heating of the wall of the crucible. This will lead to a flow mainly vertical in the crucible. Similarly, most of the experimental works on alumina dissolution with stirring using a propeller to push the liquid toward the bottom or the top (see Jain et al. [119] or Gerlach [122]). In these conditions, the main flow will be perpendicular to a floating raft, a suspended disc or a pressed tablet at the bottom of the crucible, as for a natural convection setup.

This vertical flow will have different effects depending on the sample fragility. For fragile samples, such as pressed and free powder, a direct-facing flow toward the sample will help its disintegration. On the other hand, indirect flow, such as bottom bottom-facing stirrer with floating powder or a top-facing stirrer with a pressed tablet at the bottom of the crucible, will tend to maintain the cohesion of the alumina particles. In this case, the flow will travel along the walls of the crucible before creating a concentric flow when encountering the horizontal limit of the liquid. This can explain the large difference in the results observed by Gerlach et al. [122], which can include more disintegration than the tests performed with powder injection. Moreover, after a few seconds, the powder begins to sinter and is no longer fragile, thus limiting further disintegration.

REFERENCES

[118] J. Alarie, L. I. Kiss, L. Dion, S. Guérard, J.-F. Bilodeau, and R. Santerre, "Determination of the mass transfer coefficient for the dissolution of alumina samples immersed in a cryolitic bath," *Acta Materialia (Submitted)*, 2023.

[119] R. Jain, S. Tricklebank, B. Welch, and D. Williams, "Interaction of aluminas with aluminum smelting electrolytes," *Light Metals 1983*, pp. 609–622, 1983.

[120] A. Bagshaw and B. Welch, "The influence of alumina properties on its dissolution in smelting electrolyte," in *Essential Readings in Light Metals*. Springer, 2016, pp. 783–787.

[121] L. A. Isaeva, A. B. Braslavskii, and P. V. Polyakov, "Effect of the content of the alpha-phase and granulometric composition on the dissolution rate of alumina in cryolite-alumina melts," *Russian Journal of Non-Ferrous Metals*, vol. 50, no. 6, pp. 600–605, 2009.

[122] J. Gerlach, U. Hennig, and K. Kern, "The dissolution of aluminum oxide in cryolite melts," *Metallurgical and Materials Transactions B*, vol. 6, no. 1, pp. 83–86, 1975.

[123] Y. A. Cengel and A. J. Ghajar, *Heat and mass transfer : fundamentals & applications*, 5th ed. New York, N.Y.: McGraw-Hill Education, 2015.

[124] T. Roger, L. I. Kiss, L. Dion, J. Bilodeau, Guérard, and G. Bonneau, "Experimental investigation of the alumina cloud during alumina injections in low and high temperature conditions." *Light Metals 2023*, p. NA, 2023.

[125] T. Hertzberg, K. Tørklep, and H. Øye, "Viscosity of molten naf-alf3-al2o3-caf2 mixtures: Selecting and fitting models in a complex system," in *Essential Readings in Light Metals*. Springer, 1980, pp. 19–24.

[126] H. Kvande and H. Rørvik, "Influence of bath density in aluminum electrolysis," *Journal of Metals*, vol. 36, pp. 62–62, 1984.

[127] E. Skybakmoen, A. Solheim, and Å. Sterten, "Alumina solubility in molten salt systems of interest for aluminum electrolysis and related phase diagram data," *Met-*

allurgical and materials transactions B, vol. 28, no. 1, pp. 81–86, 1997.

[128] A. Perron, "Transfert de quantité de mouvement et augmentation de la résistance électrique causés par la présence des bulles dans une cuve hall-héroult," Ph.D. dissertation, Université du Québec à Chicoutimi, Chicoutimi, 2006.

[129] O. Kobbeltvedt and B. Moxnes, "On the bath flow, alumina distribution and anode gas release in aluminium cells," in *Essential Readings in Light Metals*, 1997, pp. 257–264.

[130] C. F. Hess and C. W. Miller, "Natural convection in a vertical cylinder subject to constant heat flux," *International Journal of Heat and Mass Transfer*, vol. 22, no. 3, pp. 421–430, 1979.

[131] J. R. Welty, *Fundamentals of momentum, heat, and mass transfer*, 4th ed. New York: J. Wiley, 2001.

CHAPTER VI

DIMENSIONAL ANALYSIS APPLIED TO THE DISSOLUTION AND DISINTEGRATION OF ALUMINA RAFTS : THE RIDDLE OF DISSOLVING ALUMINA RAFTS SOLVED.

6.1 SYNOPSIS

6.1.1 OBJECTIVES

This article contributes to the objectives 1 to 6 of the thesis. The contributions are as follows:

1. The model relies on the bath and alumina properties to predict the dissolution rate of the raft. Therefore, a parametric study is now possible to determine the best combinations possible.

2. To simulate the dissolution of each layer of the raft, the mass transfer coefficient is calculated at each time step. The calculations are also described in the article.

3. Comparison between experimental results and the model shows that the behavior of a sample is well described by the model.

4. The understanding of the effect of the sintering on the dissolution of a raft is a key piece of this article. By modifying the porosity of the raft, the sintering is an important phenomenon to implement in such a model.

5. The model estimates the structure of the raft by its influence on the porosity. This changes drastically the solid-liquid contact required for dissolution.

6. The results of this article show that the mass fraction of aluminum fluoride can be adjusted to obtain a better dissolution rate for the alumina powder.

6.1.2 SCIENTIFIC CONTRIBUTION

This last article uses all the knowledge from the previous work to confirm the mechanisms of dissolution of an alumina raft. It uses a simple unidimensional simulation to predict the dissolution behavior of a raft. This is the first model that uses only physical relations to predict alumina dissolution. It is also the first time that models have been proposed to predict the rate of sintering of the alumina particles. These models indeed come from the literature but are adapted to the specific case of the alumina in cryolite.

The model is a collection of submodel available in the literature. These models are integrated over time with the finite volume method to obtain the new state of the raft at each time step. The present article explains the methodology to create such global model from the submodels. The article is also structured to describe each of the equation in the same sequence as the model use them. The model take as input the composition and temperature of the bath as well as minimal alumina properties, such as its mean diameter, density, porosity and temperature. Note that some of these submodels can be tedious to present and use. Therefore, the reader should refer himself to the cited works to adequately integrates those submodels in any works. With these input, it computes at each time step the contribution of the following phenomena :

- The infiltration of the raft (Washburn equation).

- The heat exchange between the components of the raft and their environment (heat transfer correlations, enthalpy of phase change and effective conductivity from ZBS model).
- The mass transfer between the parts of the raft (mass transfer correlations).
- The sintering of the alumina (LSW model and Avrami equation).

This model show that the thermal interactions between the solid and the liquid do not create a shell of solidified liquid around the entire raft during the first moment of its life. Be aware that a small part of the bath can effectively solidify inside the raft during this moment. However, this solidification is not complete and does not prevent the infiltration of the powder, as observed in experimental tests. Therefore, it cannot explain the agglomeration of the powder upon injection.

Note that the thermal effect does reduce the dissolution rate of the raft, by lowering the superheat of the bath inside the raft. This leads to a lower diffusivity of the dissolved alumina, and this work shows that the diffusivity is often the limiting factor of the alumina dissolution.

6.1.3 AUTHORS CONTRIBUTIONS

Work	Contributors
Direction	Prof. László I. Kiss and Prof. Lukas Dion
Design of the apparatus	Jonathan Alarie
Construction	Jonathan Alarie and Patrice Paquette
Experimental plan	Jonathan Alarie
Tests	Martin Truchon and Jonathan Alarie
Analysis	Jonathan Alarie
Writing	Jonathan Alarie
Revision	Prof. László I. Kiss and Prof. Lukas Dion
Technical Support	Sébastien Guérard and Jean-François Bilodeau

6.1.4 PUBLICATION

Authors	Jonathan Alarie, László I. Kiss, Lukas Dion, Martin Truchon, Sébastien Guérard and Jean-François Bilodeau
Year	2024
Title	Dimensional analysis applied to the dissolution and disintegration of alumina rafts: The riddle of dissolving alumina rafts solved.
Journal	TMS Light Metals
Status	Published (Reprint permission available in Appendix A.4)
Date	March 2024

6.1.5 RÉSUMÉ

Avec les préoccupations croissantes concernant la performance environnementale et la sécurité des salles d'électrolyse, la production d'aluminium primaire se heurte à de nombreux défis. Parmi eux figurent l'introduction, la dissolution et la distribution de grandes quantités d'alumine dans un petit volume d'électrolyte. De plus, les cellules d'électrolyse ont une grande surface horizontale et utilisent seulement un nombre limité de points d'injection. Généralement, un kilogramme d'alumine est injecté à chaque endroit, environ chaque minute. Cette poudre s'agglomère et crée des radeaux limitant la vitesse de dissolution. Plus important encore, pour éviter toute accumulation, les radeaux

doivent disparaître du point d'injection avant l'ajout suivant. Ceci peut se faire soit à la suite d'une dissolution, d'un transport ou d'une désintégration du radeau. Le travail présenté ici utilise une analyse dimensionnelle pour quantifier le taux de dissolution et de désintégration d'un radeau d'alumine. Une approche théorique est proposée pour comprendre les comportements clés observés lors de travaux expérimentaux approfondis sur la dissolution de différentes formes macroscopiques d'alumine. Enfin, l'application potentielle du modèle proposé est également présentée.

6.1.6 NOMENCLATURE

Parameter	Definition
a	Porosity fitting coefficient
A	Area of contact
c_f	Shape factor
C	Concentration
d	Diameter
D	Diffusivity
h	Convection heat transfer coefficient
H	Height of the infiltration front
h_m	Convection mass transfer coefficient
j	Mass flow rate
k	Avrami fitting constant
L_c	Characteristic length
Nu	Nusselt number
$\dot{Q}$	Heat flux rate
R	Gas constant
Re	Reynolds number
r	Radius
Sh	Sherwood number
t	Time
T	Absolute temperature
$\bar{V}$	Molar volume
w	Mass fraction
x	Fraction of the volume sintered

Greek letters	Definition
γ	Surface tension
Δ	Difference
ϵ	Emissivity of the surface
θ	Contact angle
κ	Thermal conductivity
μ	Dynamic viscosity
ρ	Density
σ	Stefan-Boltzmann constant
ϕ	Porosity
Subscript	**Definition**
0	Initial value
∞	Environment value
eff	Effective value
l	Value for the liquid
p	Particle value
$raft$	Raft value
rad	Value for the radiation
Superscript	**Definition**
b	Porosity fitting exponent
n	Avrami fitting exponent

DETAILED ANALYSIS OF ALUMINA RAFT FORMATION KINETICS UPON INJECTION IN CRYOLITE

Jonathan Alarie[a], László I. Kiss[a], Lukas Dion[a], Martin Truchon[a], Sébastien Guérard[b] and Jean-François Bilodeau[b]

[a] *University of Quebec at Chicoutimi, 555 Boul Universite, Saguenay, G7H 2B1, Quebec, Canada*

[b] *Arvida Research and Development Centre, Rio Tinto, 1955 Mellon Boulevard, Jonquiere, G7S 4K8, Quebec, Canada*

ABSTRACT

With increasing concerns about environmental performance and workplace security, the production of primary aluminum encounters many challenges. Among them is the introduction, dissolution, and distribution of large quantities of alumina into a small volume of electrolyte with a large horizontal surface using only a limited number of discrete injection points. Typically, one kilogram of alumina is injected at each location every minute or so, which agglomerates and creates rafts limiting the dissolution rate. More importantly, to prevent instability, the rafts must disappear from the injection point before the next addition, either as a result of dissolution, transport, or disintegration. The work presented uses a dimensional analysis to quantify the dissolution and disintegration rate of alumina rafts. A theoretical approach is proposed to understand the key behaviors observed from extensive experimental work on the dissolution of different macroscopic forms of alumina. Finally, the potential application of the model proposed is also presented.

Keywords: Aluminum electrolysis, Alumina dissolution, Cryolite properties

6.2 INTRODUCTION

The production of primary aluminum is done through the electrolysis of dissolved aluminum oxide in a cryolite melt. The dissolution of alumina is of primary concern to keep the process stable. When the content of dissolved alumina in the melt is extended beyond the operational range, instabilities appear in the thermal and electrical equilibrium. The most common of these instabilities is the anode effect, which leads to unnecessary greenhouse gas emissions, increased power consumption, and possible damage to the cell, due to localized overheating of the cell lining. On the other hand, higher concentration promotes the formation of muck under the liquid metal pad. This muck also increases the instabilities of the cell and locally modifies the electrical resistance of the cathode, causing uneven consumption of the latter. Therefore, it is essential to create a steady flux of alumina that dissolves into the electrolyte, which is challenging due to the nature of the feeding strategies. The cells are fed through periodic 1000 g additions of powdered material from 3 to 5 points over a surface of more than 70 m^2. Such cold alumina poured onto the cryolite surface rapidly agglomerates to form solid floating rafts. These rafts limit the solid-to-liquid contact necessary for an efficient dissolution of the alumina. Following recent progress related to the effect of the liquid composition on the diffusivity of alumina in cryolite melt [132] and on the raft formation dynamics [133], this work builds on to describe the mechanisms of the raft sintering, disintegration and dissolution. A model is then proposed to predict the alumina dissolution. The differences between the model and experimental results are discussed highlighting the benefits and limitations of this approach. Finally, a potential industrial application of this model is discussed.

6.3 EXPERIMENTAL METHOD

The effect of the bath conditions on alumina dissolution was estimated using a parametric study of injections in a laboratory experimental setup. The range of the parameters tested are presented in Table 6.1 and were distributed in eight conditions. These tests were conducted in a round crucible of 185 mm high and 203 mm in diameter placed in a radiative furnace. The sample was produced by the injection of 40 g of alumina, previously dried at temperatures reported in Table 6.1 for one hour. The alumina was poured into a curved funnel, with its extremity placed at 25 mm from the surface of the melt. The apparent mass of the sample was recorded with a gravimetric apparatus previously developed (see Alarie et al. [134]), with the help of a sample holder. The holder consisted of a cross of Nichrome wire with a stainless steel ring of 12 mm in height and 12 cm in diameter to limit the horizontal spreading of the powder and hold the powder by its center to the bath-air interface.

Table 6.1 : Conditions range used in the parametric study

Parameter	Minimum	Maximum
Superheat (°C)	5	15
AlF_3 (w%)	9	14
CaF_2 (w%)	4	7
Al_2O_3 (w%)	3	6
Drying temperature (°C)	100	800

6.4 RAFT DISSOLUTION MODEL

To simulate the dissolution of an alumina raft it is necessary to understand the different phenomena in action. For simplicity, the raft is considered to be cylindrical and at rest in the instants following the injection process. The dynamics of the injection

have been described by Alarie et al. [132] and allow the estimation of the alumina that goes through the interfaces, as an initial alumina cloud, and the remaining fraction that forms the alumina raft. At the moment of its formation, this raft is considered completely dry. Thus, the wetted particles are associated with the alumina cloud and are not considered at this point. Following injection, the process becomes static and the relative movement between the alumina particles is negligible. In this phase, the active phenomena affecting the alumina particles are the infiltration and phase change of the liquid, the dissolution and phase change of the alumina as well as the dry and liquid phase sintering of the particles.

The rate of these phenomena is driven by heat and mass transfer dynamics. An accurate knowledge of the properties of the materials is then important to obtain a model with adequate precision. For this purpose, the properties of the bath were calculated according to the method presented by Alarie et al. [132]. The properties range of the bath used for calculations are presented in Table 6.1. Note here that the alumina is considered as spheroid particles of 80 µm in diameter ($d_s = 8 \cdot 10^{-5}$ m) with low deformation, usually similar to those of sand particles, which have a shape factor (c_f) of 1.4 (see the VDI heat atlas [135]). The thermal properties of alumina come from an analysis presented by Alarie et al. [133].

The simulation considered is one-dimensional, and the raft simulated is similar to the ones created in the laboratory setup. Thus, they are the results of an injection of 40 g, forming a raft that is 12 cm in diameter and 3 mm in height. This heap of powder has been discretized in 51 layers as presented in Figure 6.1.

For every time step, the simulation proceeds with a specific sequence of phenomena solved explicitly. First, the raft is a dry heap of powder filled with air with fluoride

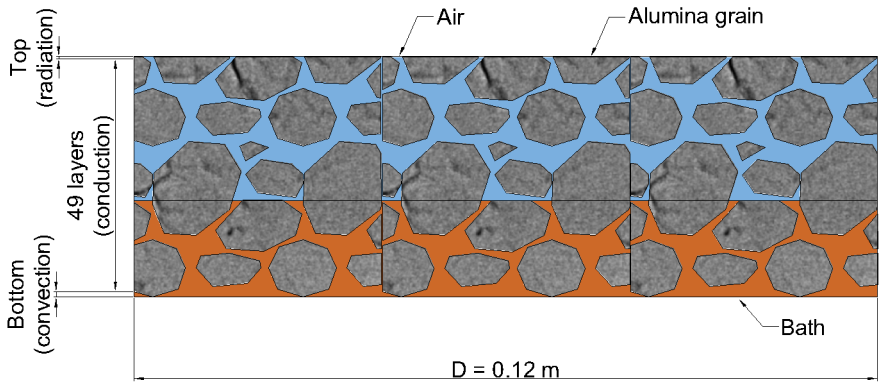

Figure 6.1 : Sketch of the discretized raft.

gas. Then, the infiltration rises in the raft, allowing more particles to be in contact with the liquid. The liquid contact also enables the liquid phase mass transfer, that is to say, the sintering of alumina, the cause of its phase change, and the dissolution. During this time, dry phase sintering of the grain modifies the porosity of the particles not in contact with the liquid. Finally, the dissolution of the alumina is calculated. This dissolution also includes the mechanisms needed for the alumina to reach the lower part of the raft and be caught by the convective flow under the raft surface.

More precisely, the simulation goes through the following phases at each time step:

1. The infiltration of the raft.
   (a) Porosity of the raft.
   (b) Height of the liquid.
2. The heat transfer mechanisms.
   (a) Effective thermal conductivity of each layer.
   (b) Convection heat transfer at the bottom of the raft.

(c) Thermal conduction.

(d) Radiative heat loss.

(e) Enthalpies influences.

3. The sintering of the alumina.

   (a) Dry sintering of the powder.

   (b) Liquid phase sintering (alumina phase change).

4. The dissolution of the raft.

   (a) Internal dissolution of **grains**.

   (b) Effective dissolution of the grain in the **layer of the raft**.

   (c) Convective mass transfer at the bottom of the raft.

   (d) Diffusion of alumina in the raft.

The calculation of each of these phases is presented thereafter.

6.4.1 THE INFILTRATION OF THE RAFT

POROSITY OF THE RAFT

The initial porosity of the raft is one of the primary parameters that influence the behavior in this porous media. It was determined with the model presented by Yu et al. [136]. This model is presented in equation 6.1, resulting from experimental measurements to obtain a model for a poured packing of the spheres from an initial parameter ($\varphi_0 = 0.567$), and two constants ($a = 0.247$ and $b = 0.749$). This model is presented in equation 6.1.

$$\varphi = \varphi_0 + (1 - \varphi_0)e^{-ad^b} \tag{6.1}$$

It is also important to consider the internal porosity of the alumina particles. This parameter was determined, using scanning electron microscopy, to be near 0.15 V%. Details on the method are presented by Alarie et al. [133]. Finally, the porosity of the wetted layer is updated at each time step from the sintering and dissolution of the alumina.

HEIGHT OF THE LIQUID

The infiltration behavior is modeled with the help of the Washburn equation, as presented by Kirdponpattara et al. [137] and reported in equation 6.2. It uses the effective particle radius (r_{eff}) in combination with the surface tension of the liquid (γ), the angle of contact between the liquid and the solid in the air (θ) as well as the liquid viscosity (μ) and the time (t) to find the height of infiltration (H). The effective particle radius is calculated from equation 6.3, presented by Hapgood et al. [138]. The use of the effective radius of the particle is to model the real porosity connection to the equivalent vertical tube, necessary for the use of the Washburn equation [137]. In the model, the bulk bath properties are used to obtain the height of the rising front of the liquid in the powder. Thereafter, each time the liquid goes up a layer, the bath in each layer also rises to the next layer, bringing a hotter bath in each layer.

$$H = \sqrt{\frac{r_{eff}\gamma cos\theta}{2\mu}t} \tag{6.2}$$

$$r_{eff} = \frac{c_f d}{3}\frac{\phi}{1-\phi} \tag{6.3}$$

6.4.2 THE HEAT TRANSFER MECHANISMS

CONVECTION HEAT TRANSFER AT THE BOTTOM OF THE RAFT

From the lower surface, a convective heat transfer toward the bulk bath is considered. Since the crucible in the experimental setup is heated from the side and because the sample represents less than 0.5 w% of the bath mass, the bulk temperature is considered constant during the test. Note that this case is also similar to that of the heating produced in industrial cells. The raft is considered as a flat plate with parallel flow and the heat transfer is calculated according to equations 6.4 to 6.6 [139]. These equations use a velocity of 35 mm/s, as measured in our experimental setup by video recording to calculate the Reynolds number. Then, the heat transfer coefficient (h) is found from the Nusselt number using the diameter of the raft as its characteristic length (L_c) and the bulk bath thermal conductivity (κ). Knowing the temperature difference between the bottom layer of the raft (from initial conditions and at each time step) and the bulk temperature (ΔT) and the surface of contact between the raft and the liquid (A) finally allows finding the convective heat flux ($\dot{Q}_c$)

$$Nu = 0.664 Re^{0.5} Pr^{1/3} \tag{6.4}$$

$$Nu = \frac{hL_c}{\kappa} \tag{6.5}$$

$$\dot{Q}_c = hA\Delta T \tag{6.6}$$

THERMAL CONDUCTION

The heat transfer in this simulation involves finding an effective thermal conductivity for each discretized layer of the raft. This effective conductivity has been found with the help of the Zehner-Bauer-Schlünder model presented in the VDI heat atlas [135]. This is a unit cell model that estimates the effective conductivity of a powder bed knowing its porosity and the thermal conductivity of the components as the primary parameters. They also consider the contribution of the radiative heat transfer and the shape of the particle to the effective thermal conductivity. This results in a thermal conductivity that changes over time and space in the raft. Moreover, the dry and wet thermal conductivities are nearly one order of magnitude apart, with a value of around 0.15 W/mK and 0.95 W/mK, respectively. In addition, an equivalent temperature must be found to estimate the heat flux between each of the layers. This is achieved with the help of the thermal capacity to weigh the temperature of the bath and the particles at this average temperature. These hypotheses allow computing the heat transfer through the body of the raft.

RADIATIVE HEAT LOSS

For the top of the raft, only a radiative heat transfer is considered. This approximation was used following previous work, which highlighted that with high temperature in the experimental setup, the convective heat transfer becomes negligible. It is also a limiting case because the convection on top of the sample can help to raise its temperature more rapidly in the first seconds, which is expected to help the overall dissolution rate of the raft. The absence of this heat input can only lower the dissolution rate in the model. The radiative heat loss ($\dot{Q}_{rad}$) was calculated with the help of equation 6.7, using the emissivity of the grains (ε_p), the Stephan-Boltzmann constant (σ) and the temperature of the grains (T_p) and the environment (T_∞).

$$\dot{Q}_{rad} = \varepsilon_p \sigma A_{raft}(1-\varphi)(T_p^4 - T_\infty^4) \tag{6.7}$$

REACTION ENTHALPIES

Finally, the enthalpies of the different reactions, taken from Dassylva-Raymond [140], are considered as follows. First, the heat flux from the adjacent layers is computed, along with the heat capacity of the liquid bath from its liquidus to its actual temperature is calculated. Then, three cases of figures can happen:

1. The total heat flux is positive and can melt solidified bath, if any. In this case, the melting of the bath absorbs energy until all the solid bath is melted. Then the bath temperature rises.

2. The total heat flux is negative, but there is sufficient heat capacity to absorb it. Then the bath temperature only decreases.

3. The total heat flux is negative and brings the bath temperature to its liquidus. Then, the bath temperature remains at its liquidus temperature due to the energy released by the bath that solidifies.

The first two cases are pretty straightforward and raise or lower the temperature of the layer of the raft according to simple thermal balance. The third case is of more concern. It is known that the solid bath that usually forms is mainly consisting of pure cryolite. Therefore, the solidification of the bath inside the raft changes the additive mass fraction in the remaining liquid. This behavior is also considered in the simulation and lowers the liquidus temperature of the melt for the successive time step. Consequently, only a small amount of solid bath is formed in the raft. Moreover, no layer completely solidifies its liquid content at any time of the simulation. This is due to the infiltration of the bath, the convective heat transfer under the raft, and the effective conductivity of the dry layer above the liquid. These three phenomena cause the temperature of the alumina grains to rise quickly before contact with the liquid.

6.4.3 THE SINTERING OF THE ALUMINA

It is clear here that the initial properties of the alumina are of first importance in the raft sintering kinetic. Properties such as α-alumina content, the BET surface, the MOI, the LOI, and the presence of adsorbed fluoride in the alumina particles are known to influence the dissolution process of alumina, but, moreover, its sintering behavior. Note that the relation is not linear, nor direct, for the influence of these parameters on

the dissolution, because they impact the sintering process. The exact contribution of each of these parameters to the alumina sintering is exposed hereafter.

DRY SINTERING OF THE POWDER

The dry sintering kinetics is usually modeled with the Avrami equation, reported in equation 6.8 as presented by Macêdo et al. [141]. It relies on a kinetic constant (k) and an exponent (n) to fit experimental data to the Avrami equation. This kinetic depends on the gas in contact with the alumina and the volatile molecules created during the sintering. To find the experimental parameters (k and n), the exact composition of the gas in the pores of the raft and their effect on sintering should be the subject-specific investigations. Without this information, the data reported by Bagwell and Messing [142] are here used. Their work estimated the influence of water vapor in the sintering of alumina. It appears that this speed is similar to that of Shacklee, reported in Bagwell and Messing [142], which concerns fluoride gas influence. For this reason, an exponent of $n = 2.1$ was selected to use in the Avrami equation with AlF_3 vapor. Along with the value reported by Shacklee in Bagwell and Messing [142] ($x = 1$ and $t = 30min$), the constant k of the Avrami equation was approximated to be 0.03. With these parameters, the dry sintering speed has been estimated in an alumina raft.

In the dry sintering process, the gas composition in contact with the grains is of first importance. Two specific gases, in addition to the air, can be identified; water vapor and fluoride gas. Bagwell and Messing [142] demonstrated the importance of the water vapor in the particles on the kinetics of dry sintering. The effect of the water vapor, which comes from the MOI content, has a proportional effect on the sintering rate just a little lower than that of the fluoride vapor. For the purpose of these simulations,

the MOI content effect has been associated with the effect of the fluoride vapor and a unique value has been applied to the dry sintering process. A better description of the composition of the gas in the porosities of the raft should be the subject of future experimental tests. The LOI parameter is related to the moisture content in the alumina crystal. It allows the release of water vapor all along the liquid phase sintering. This creates bubbles inside the body of the raft, which increases in volume as the vapor is released and the temperature of the gas increases.

Since the absolute mass fraction of AlF_3 in the liquid bath is nearly constant, around half of total mass of the bath (with BR range from 1 to 1.2), we can also assume that the vapor composition is nearly constant and that the dry sintering of alumina particles is the same for all conditions.

$$x = 1 - e^{(-kt^n)} \tag{6.8}$$

LIQUID PHASE SINTERING (ALUMINA PHASE CHANGE)

The liquid phase sintering is the less known of the mass transfer phenomena that occurs in a raft. It relies on the alumina diffusivity in the liquid to establish a dynamic equilibrium between the dissolution of the alumina and its precipitation in α-alumina, which corresponds to the phase change of alumina. In fact, the γ-alumina dissolution, catalyzed by the presence of fluoride [143], quickly saturates the melt inside the alumina particle, while the α-alumina content of the particle remains in the solid form. Therefore, due to the local pressure gradient created by the curvature of the surfaces, the dissolved alumina precipitates on these α-alumina seeds, forming alumina platelets [144].

Bagwell and Messing [142] also described the influence of the number of α-alumina seeds in the alumina crystal. The α-alumina seed content in the particle, which has been related to the weight fraction in this simulation, acts as precipitation sites for the dissolved alumina. Bagwell and Messing [142] also suggested that the sintering kinetics is favored proportional to the number of seeds until a given value. In the case of the alumina raft dissolution, this also means that alumina with a higher value of α-alumina content undergoes faster sintering than that with less α-alumina phase until this threshold. Above this value, it is important to understand that a smaller fraction of the raft undergoes sintering since the alumina is already in its more stable form. Therefore, the increase in porosity created by the dissolution-precipitation phenomenon inherent to the sintering does not occur, thus limiting the effective diffusion of the alumina and then the overall dissolution process.

Note that the shape of the internal porosities of the grain, usually related to the BET surface of the grain, also creates a suitable site for the precipitation of the dissolved alumina. A change in the BET surface of the alumina modifies the sintering behavior of the alumina. Macêdo et al. [141] showed that the rate of sintering of the alumina is proportional to its surface area. This is expected since a larger area of the surface increases the availability of precipitation sites and the availability of the alumina to dissolve.

The transport of the dissolved alumina is then strongly inherent to the diffusivity of the alumina in the liquid. This dissolution precipitation happens very fast in the first seconds of the bath presence and slowly decays over time. The equilibrium is reached when the alumina platelets have a diameter of about 10 μm, as reported in the literature [145, 144, 146, 147]. Once the equilibrium is established, the alumina platelets begin to slowly dissolve and shrink, leading to the efficient part of the raft dissolution.

The Lifshitz-Slyozov-Wanger (LSW) theory (from Kang [148]) was used to simulate the liquid phase sintering. According to this theory, the grain growth of the alumina can be estimated using the gas constant (R), the diffusivity of the alumina in the liquid (D), the molar ratio (C_∞) of alumina dissolved around the particle and its molar volume ($\bar{V}$). Equation 6.9 then allows finding the particle radius (r) at a given absolute temperature (T) after a certain time (t). Once the sintering phase of the simulation is completed, the porosity of the raft is updated accordingly.

$$r = \sqrt[3]{\frac{8}{9}\frac{D\gamma C_\infty \bar{V}}{RT}t + r_0^3} \tag{6.9}$$

Here it is important to understand that the particles involved are the α-alumina seeds and not the alumina grains. As mentioned earlier, the dissolved alumina precipitates on the α-alumina present in the grains to form the platelets. Note that for simplicity, the platelets are considered as a sphere for this calculation instead of the octagonal prism that is presented in the literature.

The number of seeds and their size are of primary concern to adequately simulate the sintering behavior. Moreover, the size at which they reach equilibrium drives the alumina surface available for dissolution in further steps. Unfortunately, this information is not available in the literature, and the usage of a specific hypothesis was required to proceed with this step of the work. The mass fraction of α-alumina in an alumina particle, obtained by chemical analysis, was used to find its volume in the grain. Thus, with the assumption that the platelets are spherical particles, the volume of α-alumina was divided into several seeds of a given diameter to match the appropriate value. The diameter of the seeds was fitted to the size observed using scanning electron microscopy, obtained in experimental tests on this specific subject.

6.4.4 THE DISSOLUTION OF THE RAFT

Convection plays an important role in the heat and mass transfer affecting the raft dissolution. This convection is driven by the bath properties (density, viscosity, alumina solubility, and alumina diffusivity) and can be calculated from the composition of the melt [132]. With these properties, it is easy to find the Grashof or Reynolds (depending on the case described further) and the Schmidt numbers useful in the calculation of the Sherwood number with reported semi-empirical relations. These relations, reported in equations 6.10 and 6.11, relate the dissolution flux of an alumina surface (ϕ) to the Sherwood number by the use of the contact area (A), the bath density (ρ_l), the alumina mass fraction gradient (ΔC), the characteristic length of the raft (L_c) and the diffusivity of alumina in the melt. Once the Sherwood number is known, the alumina flux through a given surface can be calculated, using the convective mass transfer coefficient and the alumina solubility. The detail on the diffusivity of the alumina in cryolite melts can be found in Alarie et al. [132].

$$Sh = \frac{h_m L_c}{D} \tag{6.10}$$

$$j = h_m \rho_l A_{raft} \Delta w \tag{6.11}$$

INTERNAL DISSOLUTION OF GRAINS

At the beginning of the dissolution-precipitation behavior caused by the liquid phase sintering, a part of the dissolved alumina is allowed to diffuse from the inside of the alumina particle to the bath trapped inside the raft. The amount of diffusing alumina increases as the equilibrium of precipitation is achieved. This diffusion is also

limited by the presence of the solid alumina in the diffusion path, leading to a lower effective diffusion from the alumina particle to the bath inside the raft. This effective dissolution of the particles then increases the alumina content of the intergranular bath, which also need to diffuse toward the surface of the raft. To find the dissolution rate of the seeds, a Sherwood number of 3 is used, which corresponds to the limiting case where the Grashof number tends to zero.

EFFECTIVE DISSOLUTION OF THE GRAIN IN THE LAYER OF THE RAFT

In the effective dissolution of an alumina grain, it is necessary to consider the flow of the bath around it. Since there is infiltration, which creates a liquid flow in the porous media, a higher Sherwood number is expected. Moreover, the bubbles created by the desorption of the gas trapped inside the grains create a dynamic flow in the raft. The volume of the bubble is crucial for the dissolution process. This is because the growth of the bubble push saturated bath, situated in the raft porosities, outside the raft, thus momentarily increasing the effective diffusion of the dissolved alumina. On the contrary, the release of the bubble from the raft body creates a void that the bath in the surrounding pores fills, bringing fresh bath in contact with the alumina. This decreases the effective diffusion of the alumina for a very short time but enhances the overall dissolution of the alumina. Consequently, the LOI content of the alumina is favorable to the dissolution process, but this effect is also dependent on the viscosity of the gas and liquid inside the raft. The model presented here is not yet mature enough to take this dynamic into account. Therefore, it is approximated by an additional increase in the Sherwood number, which was fixed at 5.

CONVECTIVE MASS TRANSFER AT THE BOTTOM OF THE RAFT

The last layer of mass transfer represents the effective dissolution of the alumina raft through its surface in contact with the bulk electrolyte. Here again, this dissolution is inherent to the effective diffusion of the alumina inside the porosities of the raft. However, this part of the dissolution is subject to intensive agitation of the liquid, which leads to a larger convective mass transfer, strongly influenced by the bath properties. The convective dissolution of the raft is then modeled by equation 6.12, which represents the dissolution of a flat plate parallel to the flow.

$$Sh = 0.664 Re^{0.5} Sc^{1/3} \tag{6.12}$$

DIFFUSION OF ALUMINA IN THE RAFT

The diffusivity of alumina in cryolite is influenced by the presence of solid particles along the path. To take this into account, the model from Weissberg [149], presented in equation 6.13 from Kim et al. [150] was used. It uses the diffusivity of alumina in cryolite (D) to obtain the effective diffusivity (D_{eff}) from the porosity (ε) of the porous media. Two levels of porosity need to be considered, that of the alumina particles and that of the raft. Accordingly, the effective diffusivity in these two cases is different and expressed as in equation 6.13.

$$D_{eff} = \frac{D}{1 - 0.5 \cdot \ln \phi} \tag{6.13}$$

6.5 RESULTS

The experimental measurements made on powder poured on the bath surface still imply more phenomena than those that were described in the previous section. Therefore, considering the dissolution behavior in a single injection is unlikely to give a proper estimation of the accuracy of the proposed method. Nevertheless, Figure 6.2 presents a typical result from a single test to understand the overall raft behavior, along with a simulation run with the same conditions. Also note that the interpretation presented in this analysis comes from the results of the model

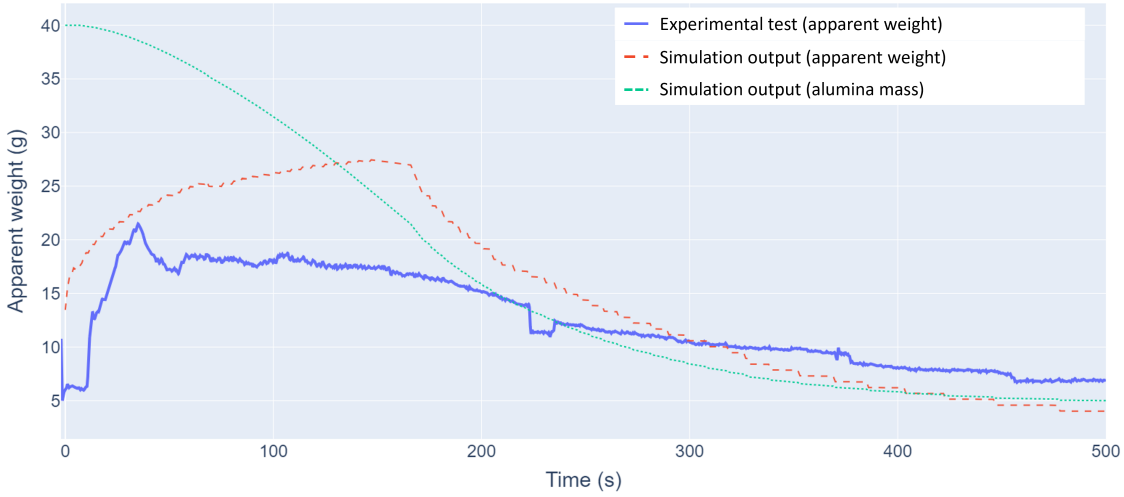

Figure 6.2 : Typical gravimetric curves obtained in the parametric study compared to the output of the model.

It can be seen that the mass of the raft increases rapidly at the beginning of the test. Therefore, a large amount of gas is generated and escapes the raft, causing an abrupt change in the apparent weight of the raft, which is also lower due to its gas content. Also, the mass of the raft seems to attain its maximum near 35 seconds, when half of the raft is infiltrated and the dissolution of alumina is not quite set. After this maximum, the mass of the raft decreases almost linearly until the complete dissolution.

Note here that, since the dissolution of the raft was recorded on video, the opening of the furnace induced cooling at the surface of the bath, limiting the dissolution of the top layer of the raft.

For comparison Figure 6.2 also presents the apparent weight calculated with the model developed in this work, as well as the real alumina mass in the raft. Note that, from the model output, the bath temperature is colder than the liquidus of the bulk bath for less than 20 seconds. This is due to the rising of the hot bath during the infiltration of the raft and because the heat transfer from the bulk bath is more intensive in the alumina particles. Therefore, a very low amount of cryolite is allowed to solidify in the lower layers of the raft, and then no solid barrier is created to stop the alumina diffusion. From Figure 6.2, it can be seen that the dissolution of alumina begins in the first ten seconds of contact with the melt. However, at the beginning, only the first layers are able to dissolve. Then, as the liquid rises in the raft, the dissolution of the subsequent layers begins and increases the alumina mass fraction in the raft. This dissolved alumina can then reach the lower surface of the raft to be dispersed in the bulk electrolyte. Then, when enough layers dissolve, the alumina dissolution rates increase and become quite linear after 60 seconds, until 200 seconds. Afterward, the lower layers begin to disappear more rapidly, thus limiting the number of layers that effectively dissolve, and the dissolution rates decrease accordingly.

6.6 DISCUSSION

The models and hypotheses employed to build the simulations presented here have their own limitations and the coupling between them can be enhanced by appropriate models and experiments. Nevertheless, this first attempt to simulate the whole behavior of an alumina raft dissolution gives results in agreement with the experimental tests

and illustrates the high potential of the described model. The simulations presented can benefit from the addition of specific values, namely for the BET surface, MOI, and LOI. The use of adequate values should increase the reliability of the model for the reasons presented here. The following considerations should be taken into account to enhance the model's reliability.

The use of spheroid particles of alumina with constant diameter for the calculation is surely one of the most influential parameters in error mitigation. The real alumina raft has a much broader range of particle size and shape. This greatly influences the porosity of the raft, which controls the infiltration velocity and the liquid-to-solid ratio. These parameters then influence the effective thermal conductivity of the raft, the sintering of the alumina, and the effective diffusion of alumina. For more precision, a size distribution function should be used in the equations of the model.

The one-dimensional simulation presented here is indeed simpler than reality and thus participates in the error of the model. A radial infiltration of the raft can be observed in the dissolution test performed. This is inherent to the size distribution of the particles as well as the angle of repose of the heap of powder. A three-dimensional approach should lead to results closer to the real behavior. However, the one-dimensional simulation has the advantage of requiring fewer computational resources, which lead to a simulation versus real time ratio of 2. The optimization of the program used to compute the model should allow for real-time simulation, which is beneficial for considering the potential coupling of the method with other mathematical models.

The Lifshitz-Slyozov-Wanger theory assumes a dispersed system with a solid fraction that tends to zero. This is not the case in an alumina raft and the use of the LSW theory is here only a rough approximation of the sintering behavior of the alumina

particles. Moreover, models of sintering with infiltration already exist and should be applied here (see German [151]).

The use of the bath properties of the first layer in the Washburn equation gives only an estimation of the infiltrating front. The properties of the bath, at the infiltration front should be used instead. However, this only changes slightly the position of the front, since two things arise from this situation. First, the decrease in temperature increases the viscosity and slows down the infiltration. Second, the solidification of cryolite, if the temperature drops under the liquidus, decreases the cryolite ratio (CR), which in turn decreases the viscosity. More work is needed here to quantify the exact influence that those two behaviors will have on the infiltration speed. However, calculations made in this work are fairly close to the observed value in experimental tests.

The main difference between the simulation and the experimental results comes from the presence of gas inside the raft. The model presented here is not yet capable of simulating the desorption of the gas and its influence on the amount of liquid inside the raft. Moreover, the gas desorption creates voids in the porosities of the raft. As the gas amount in these voids increases, their volume expands, pushing the cold bath saturated with alumina outside the raft. When these internal bubbles are released, the voids created suck more hot bath with low alumina content from the bulk liquid. Then, the formation of bubbles inside the raft limits the dissolution while the bubble forms but increases the amount of fresh bath inside the raft.

6.7 INDUSTRIAL CONCERNS

The model presented here can greatly help the industry to see the effect of their operating conditions on the dissolution of a batch of alumina. For example, Figure 6.3

shows the impact of the mass fraction of aluminum fluoride on the dissolution rate of a raft in a standard industrial bath.

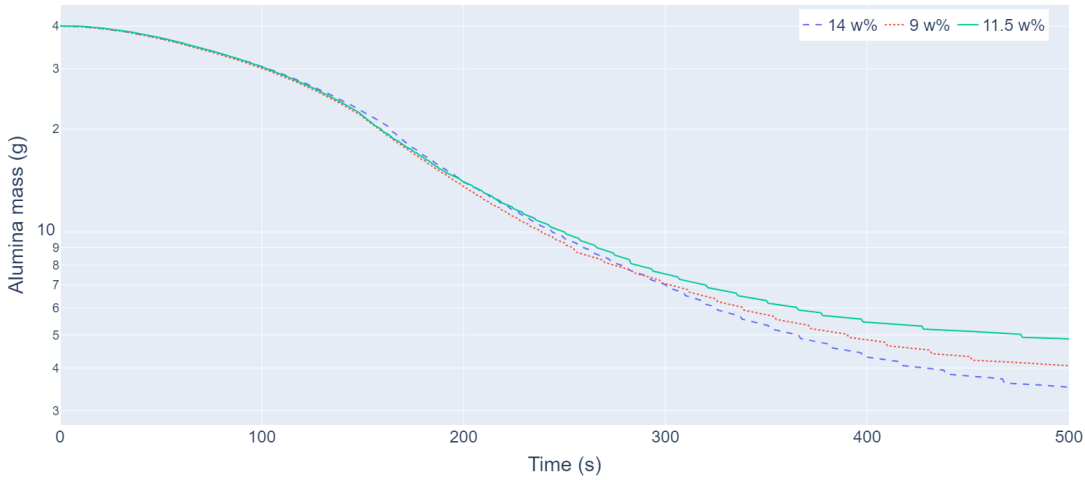

Figure 6.3 : Dissolution rate of an alumina raft at various mass fractions of AlF_3.

Figure 6.3 shows that an increase in aluminum fluoride has a small impact on the dissolution rate of a raft. This can be explained by the fact that the dissolution of a raft is limited by the diffusivity of the alumina between the layers of the raft more than by the concentration gradient. Therefore, since the AlF_3 content of the bath increases the diffusivity of the alumina (see Alarie et al. [132]), the raft will dissolve at a fairly similar rate. However, the increase of the AlF_3 allows reducing the temperature of the cell, by about 15 °C in the case presented here. This will lead to a favorable effect such as the limitation of the sintering of the alumina. Then, the raft created will be more fragile and will disintegrate more easily. Unfortunately, the actual model cannot take this parameter into account, but a more sophisticated model will be built, from the one presented here, to address these concerns.

6.8 CONCLUSION

The dissolution of alumina rafts has been modeled by the coupling of different models already existing in the literature. This model takes into account the infiltration of the liquid, as well as the heat and mass transfer inside the raft. Results show that the dissolution of alumina occurs in the first seconds of contact with the liquid and that temperature does not limit the dissolution at this moment. This model was compared with experimental results and the difference between the two sets of results is discussed. In the end, some improvements have been suggested, but the model proves to predict the alumina raft dissolution rate with impressive precision for its simplicity. The results obtained from the model will therefore be an essential tool for anyone who wants to improve the dissolution of alumina in industrial cells.

6.9 ACKNOWLEDGEMENT

The authors want to thank Rio Tinto, the Natural Sciences and Engineering Research Council of Canada, the Fonds de recherche Nature et Technologies of Quebec, by the intermediary of doctoral scholarship, and the Aluminum Research Centre REGAL, for their technical and financial support for this project.

6.10 POST PUBLICATION REFINEMENT

6.10.1 POROSITY ROLE

The porosity in the model is one of the most important parameters, which evolves over time. The porosity of the raft is composed of two levels of porosity: intergranular porosity and intragranular porosity. To fully understand the following explanation, it is

suggested to have a second look at Figure 2.8, which show the transformation of alumina described thereafter.

The intergranular porosity is determined by the granulometry of the powder and by the friction forces between the grains that lead to a packed bed of particles. To estimate this porosity, the present model uses a submodel created by Yu et al. [136], which depends solely on the diameter of the particles.

The intergranular porosity will drive the infiltration behavior of the liquid through the Wasburn equation [137, 138], along with the surface tension [152]. Depending on the size of the particles, the porosities will act as capillary of different effective radius (equivalent to a cylinder of constant radius).

The intragranular porosity represents the fraction of the void inside an alumina particle. These porosities are the real surface of exchange between the bath and the solid alumina. The initial porosity is estimated from SEM images, such as the one presented in Figure 2.8c.

Once the γ-alumina particles are put in contact with fluoride (gas or liquid), the γ-alumina transform into platelets of α-alumina as described by Shaklee [143]. This transformation will greatly increase the porosity of the alumina grains, but will also increase the mean diameter of such grains. Therefore, the intergranular porosity and the intragranular porosity of the raft will be influenced by the sintering of alumina. These modifications of the porosities are computed with the help of the Avrami equation [141, 142], for sintering with gaseous fluoride, and the LSW model [148], when in contact with the liquid.

However, since the sintering of alumina in contact with gaseous fluoride is much slower than that with liquid fluoride, the infiltration speed of the raft is only slightly influenced by the sintering, and mostly in the superior layers of the raft.

6.10.2 GAS DYNAMIC

Alumina is well known to adsorb moisture and other gases[153], especially during the dry scrubbing process [154]. Therefore, the heating of alumina will allow these gases to desorb. While the heating of the alumina particles in a raft is mainly due to the contact with the hot liquid, the desorption of these gases will create bubbles inside the body of the raft. As the desorption occurs, gases will fill the porosities with the raft, both intergranular and intragranular. Figure 2.8b show the kind of structure that can be achieved in this case.

As the bubbles growth and fill more adjacent porosities, the liquid bath will be expelled from those porosities. This will push the bath surrounding the bubble to other parts of the rafts, which can be higher or lower part of the raft. In the first case, the bubbles push the bath toward the top of the raft, thus promoting the infiltration of the raft. On the other hand, pushing the bath toward the bottom of the raft will expel that bath from the raft itself. When the bubble escapes from the top of the raft, the reaction will be inverse, and the bath pushed away will flow back and fill the porosities.

This dynamic will create a flow of bath inside the raft, as the bath will be pushed and drag into the porosities. The bath inside the raft can contain much more dissolved alumina then the bulk bath, due to the dissolution of the platelets inside the raft. Also, the bath expelled from the raft will be quickly replaced bath fresh bath under the raft surface. Therefore, when the bubble escapes the raft, the bath that will reenter the raft

will have a lower alumina content. In these conditions, the dissolution of the platelets in contact with this new bath inside the raft will be enhanced. This is true for two reasons, the movement of the liquid inside the raft represents a forced convection that helps the dissolution, while the new bath creates a larger gradient in dissolved alumina.

Despite the enhancement of the dissolution by this behavior, bubbles can also be harmful to it. The presence of the bubbles prevent all dissolution during its creation and growth, until its release. These are the reasons why the bubbles influence is estimated to be negligible in the actual model. However, more works are definitely needed on that topic. Also, note that the composition of the gases in the bubbles is still unknown at the moment. For the purpose of the simulation, the composition is estimated to be similar to that used by Shaklee [143] and Bagwell and Messing [142]. Their results suggest that the sintering behavior is similar regardless of the gas used for the tests. Nevertheless, this is another important subject to study in future work.

6.10.3 SOLIDIFICATION OF THE BATH

Solidification of the bath inside the raft is another important feature. To adequately catch this behavior, it is necessary to know the precipitating molecules. There are usually two possibilities in a standard industrial bath: alumina or pure cryolite. The dynamic of dissolution and precipitation of the alumina is already taken into account in the sintering phase. Therefore, in the thermal phase, only the precipitation of pure cryolite is considered.

In the actual model, the enthalpy of fusion pure cryolite is then applied at the same time as the other contributions to the change in temperature, that is to say the enthalpy of dissolution, the heat exchange between the layers and the heat exchange

between the bath and the grains. The solidified mass is then obtained and subtracted from the total amount of cryolite in the melt. As the cryolite solidifies, the mass fraction of the additives will augment, thus changing the local properties of the bath.

Finally, it is also important to tune the time step of the calculations. If a time step too long is used, instabilities in the simulations appears and temperatures of the component of the raft greatly oscillate. These instabilities are self-amplified and lead the simulation to the failure of the simulation. Therefore, a time step of 5 milliseconds was used to avoid those instabilities.

REFERENCES

[132] J. Alarie, L. I. Kiss, L. Dion, S. Guérard, J.-F. Bilodeau, and R. Santerre, "Determination of the mass transfer coefficient for the dissolution of alumina samples immersed in a cryolitic bath," *Acta Materialia (Submitted)*, 2023.

[133] J. Alarie, L. Kiss, L. Dion, S. Guérard, and J.-F. Bilodeau, "Detailed analysis of alumina raft formation kinetics upon injection in cryolite." *In Preparation*, 2024.

[134] J. Alarie, T. Roger, L. I. Kiss, S. Poncsák, S. Guérard, and J.-F. Bilodeau, "Validation of the gravimetric method to properly follow alumina dissolution in cryolitic bath," in *Light Metals 2020*. Springer, 2020, pp. 680–687.

[135] V. D.-G. V. u. Chemieingenieurwesen, *VDI heat atlas*, 2nd ed. Berlin ;: Springer, 2010.

[136] A. B. Yu, J. Bridgwater, and A. Burbidge, "On the modelling of the packing of fine particles," *Powder Technology*, vol. 92, no. 3, pp. 185–194, 1997.

[137] S. Kirdponpattara, M. Phisalaphong, and B.-m. Z. Newby, "Applicability of washburn capillary rise for determining contact angles of powders/porous materials," *Journal of Colloid And Interface Science*, vol. 397, pp. 169–176, 2013.

[138] K. P. Hapgood, J. D. Litster, S. R. Biggs, and T. Howes, "Drop penetration into porous powder beds," *Journal of colloid and interface science*, vol. 253, no. 2, pp. 353–66, 2002.

[139] Y. A. Cengel and A. J. Ghajar, *Heat and mass transfer : fundamentals & applications*, 5th ed. New York, N.Y.: McGraw-Hill Education, 2015.

[140] V. Dassylva-Raymond, "Analyse et modélisation du comportement des agrégats d'alumine dans le procédé hall-héroult," Thesis, 2015. [Online]. Available: https://constellation.uqac.ca/4121/

[141] M. I. F. Macědo, C. A. Bertran, and C. C. Osawa, "Kinetics of the $\gamma \rightarrow \alpha$-alumina phase transformation by quantitative x-ray diffraction," *Journal of Materials Science*, vol. 42, no. 8, pp. 2830–2836, 2007.

[142] R. B. Bagwell and G. L. Messing, "Effect of seeding and water vapor on the nucleation and growth of α-al2o3 from γ-al2o3," *Journal of the American Ceramic Society*, vol. 82, no. 4, pp. 825–832, 1999.

[143] C. A. Shaklee II, *Matrix-mediated, chemical vapor transport synthesis of alpha alumina platelet-shaped particles.* The Pennsylvania State University, 1994.

[144] A. R. Johnson, "Alumina crusting and dissolution in molten electrolyte," *Journal of Metals*, vol. 34, no. 3, pp. 63–68, 1982.

[145] R. F. Hill, R. Danzer, and R. T. Paine, "Synthesis of aluminum oxide platelets," *Journal of the American Ceramic Society*, vol. 84, no. 3, pp. 514–520, 2001.

[146] D. Townsend and L. Boxall, "Crusting behavior of smelter aluminas," in *Essential Readings in Light Metals*, 1984, pp. 613–621.

[147] P. N. Østbø, "Evolution of alpha phase alumina in agglomerates upon addition to cryolitic melts," Ph.D. dissertation, Trondheim, 2002.

[148] S.-J. L. Kang, *Sintering: densification, grain growth and microstructure.* Elsevier, 2004.

[149] H. L. Weissberg, "Effective diffusion coefficient in porous media," *Journal of Applied Physics*, vol. 34, no. 9, pp. 2636–2639, 1963.

[150] J.-H. Kim, J. A. Ochoa, and S. Whitaker, "Diffusion in anisotropic porous media," *Transport in Porous Media*, vol. 2, no. 4, pp. 327–356, 1987.

[151] R. M. German, *Sintering theory and practice*, 1996.

[152] V. Daněk, O. Pataraák, and T. Østvold, "Surface tension of cryolite-based melts." *Canadian Metallurgical Quarterly*, vol. 34, no. 2, pp. 129–133, 1995.

[153] Y. Yang, W. Tao, W. Liu, X. Hu, Z. Wang, Z. Shi, and X. Shu, "The adsorption behavior of moisture on smelter grade alumina during transportation and storage—for

primary aluminum production," *Metals*, vol. 10, no. 3, p. 325, 2020.

[154] A. Gillespie, M. Hyland, and J. Metson, *The Surface Chemistry of Secondary Alumina from the Dry Scrubbing Process*, 2000, pp. 956–961.

CHAPTER VII
CONCLUSION

7.1 OBJECTIVES

The work presented in this thesis is of first importance in the electrolysis process to produce aluminum. It describes the kinetics dissolution of alumina, and thus the effect of the bath conditions on the Sherwood number. This work aims to explain how the alumina rafts are formed and how they dissolve and are then considered a success.

More precisely, the objectives of the research project are reached with the following advances :

1. Determine the optimal chemical and physical conditions for dissolving alumina in cryolite:

   The dissolution of alumina powder is limited by the diffusivity of the dissolved alumina in the cryolitic bath. A simple simulation, with the use of the Wilke-Chang equation presented in chapter 4, shows that the optimal composition of the bath should be around its eutectic composition. However, these results depend on the reliability of the Wilke-Chang equation in this region and should be the subject of experimental tests to confirm it. Nevertheless, literature data [155, 156] present values for the diffusivity of the dissolved alumina similar as those found in Chapter 4 Also, Chapter 6, along with preliminary analysis of the parametric study results for floating rafts, prove that the diffusivity estimation is adequate.

2. Determine the mass transfer coefficient of alumina in cryolite as a function of the morphology of the alumina, the physicochemical properties of the bath, and the flow conditions;

   The mass transfer coefficient of the alumina in cryolite can be obtained from the general mass transfer relation and the diffusivity found with the Wilke-Chang equation. The simulation presented in chapter 6 explains how to apply it to different morphology of alumina and different flow patterns.

3. Identify the dissolution mechanisms of alumina;

   Chapter 4 gives an insight into the molecular mechanisms involved in alumina dissolution. Depending on the bath composition and temperature, ions $Al_2OF_x^{4-x}$ seems to be produced at low alumina concentration and $Al_2O_2F_x^{2-x}$ seems more probable at high alumina concentration (see Machado [157]). The precise identification of the ions produced can be of great interest to further improve the understanding of the alumina dissolution.

   For the macroscopic mechanisms, chapter 4 and 6 demonstrate that the limiting factor is the diffusivity of the dissolved alumina. This is particularly true in the case of the powder trapped in a raft. The alumina that dissolves in the pores of the raft can only reach the bulk liquid by diffusion through the adjacent pores. Increasing the diffusivity then increases the dissolution rate of a raft.

4. Understand the phenomena surrounding the formation of alumina powder rafts; Chapter 6 explains how the sintering of the alumina changes the internal porosity of the raft. The evolution of the porosity will impact the internal dissolution rate of the alumina and the diffusivity of the dissolved molecules in the pores inside the raft.

5. Explain the structure of rafts and their formation conditions;

   Once the raft is established, chapter 6 explains how the bath properties will influence the sintering of the alumina grains, and thus its porosity.

6. Determine favorable conditions for the formation of rafts.

   Finally, chapter 6 shows that a higher temperature and aluminum fluoride content in the melt is also a favorable condition to increase the sintering velocity of the alumina particles, once they are trapped in the heap of powder that forms the raft.

7.2 OUTCOME OF THE PROJECT

Currently, electrolysis cells are operated using an overfeeding sequence to increase the dissolved alumina concentration, followed by an underfeeding sequence to reduce the cell alumina concentration. Each plant uses its own sequence, but the overfeeding period is generally of a fixed duration, while the underfeeding is stopped when the cell is close to the anode effect. With no reliable reference to know the exact alumina concentration in the cell, the process relies on the variation of the bath resistance, which does indeed correlate with the alumina concentration in the bath. However, this variation in resistance can also be influenced by other factors outside the process control, such as temperature. Thus, the alumina underfeeding of the cell could be stopped at a concentration different from that desired in the cell. In this case, there is a greater chance that the cell will reach a critical alumina concentration.

The current project allows the development of a virtual sensor by calculating the dissolution rate of injected alumina. Of course, the accuracy of this sensor is directly influenced by the prediction of the dissolution rate of an alumina raft. However, Chapter

6 demonstrates the reliability of the proposed approach to build such a sensor. Thanks to this virtual sensor, it will be possible to obtain a second source of information on the alumina concentration of the bath to stop the underfeeding sequence at the desired alumina concentration. With such an enhanced control, it is also possible to lower the overall variation in alumina concentration of the pot, and remain closer to the optimal operation value.

Also, the spatial distribution of dissolved alumina in the tank is not uniform (see Dion et al. [158]). Some anodes are known to have a more difficult supply of dissolved alumina. In the case of an underfeeding sequence completed late, these anodes are very likely to trigger an anode effect.

Many simulators are currently available to estimate this spatial distribution. However, these works require knowledge of the diffusivity of alumina in the cryolite. Previously, only one data was available for this purpose. Thanks to the content of Chapter 4, it is now possible to obtain a reliable value for the diffusivity of alumina, which varies with the composition of the bath. The dependence on the composition of the bath is very important, since the optimization of the Hall-Héroult process is now based on improvements of the order of one percent. However, as explained in Chapter 4 and by Thonstad [155], the diffusivity of alumina can vary substantially (more than 10%). Chapter 4 is therefore essential for understanding the spatial distribution of alumina in electrolysis cells. With such an understanding, it also becomes possible to implement a different feed frequency for each feeder, depending on the quantity required for each zone of the cell.

Another advantage to knowing the diffusivity of the alumina will also be that the overvoltage of the cell can be optimized. The overvoltage is imposed on the cell

especially to quicken the migration of the dissolved alumina toward the reaction zone [159]. This migration is also possible through the concentration difference between the reaction zone and the bulk bath in the cell. Therefore, an accurate knowledge of the diffusivity of the dissolved alumina in the cryolitic bath allows the estimation of the velocity of this molecular migration. Then, the overvoltage should only compensate for the missing molecular flux toward the reaction zone. In short, since the diffusivity depends on the bath chemistry, so should the overvoltage needed to ensure a constant flux of dissolved alumina under the anode.

7.3 RECOMMENDATIONS

The work presented here is indeed a breakthrough in the research about the dissolution of the alumina. It gives a precise overview of the phenomena involved in the dissolution of a raft. However, some phenomena should be accessed with more details, as follows:

- The relation between the bath composition and the diffusivity, here estimated with the Wilke-Chang equation, should use a more suitable expression. Special formulation exists [160] that involves the different ions in the mixture and their properties. Such information was unavailable during this work but can enhance the results obtained for the diffusivity related to the bath composition, especially far from the composition interval studied.

- The identity of the ions that are created by the dissolution of the alumina in the cryolitic melt is still to be clearly determined. An accurate knowledge of these ions and their properties will help to develop the model about the diffusivity of the alumina.

- A detailed simulation integrating the concept of wet agglomeration should be created. This will help to have a better understanding of the phenomena that occur upon the contact of the powder with the liquid. Since these first agglomerates are responsible for the creation of the raft, a better comprehension can create new solutions to the problem.

- The role of the fluoride in the alumina sintering should be accessed in detail. It is well-accepted that it catalyzes the sintering reaction. However, the sintering occurs only after the dissolution of the alumina, which therefore can precipitate on adequate sites. If the fluoride content of the bath can enhance this reaction. Then it is obvious that the fluoride can also strongly influence the dissolution of the alumina.

- The raft dissolution model, as presented in chapter 6, is only a proof of concept. Therefore, a more ambitious model should be built to take into account the geometry of the raft and confirm that the results obtained are close to the reality.

- The degassing of the water and air trapped at the surface of the alumina particles has not yet been implemented. The addition of this phenomenon will also influence the dissolution rate by preventing the solid-liquid contact locally while the gas is trapped in the pores of the particle. Note also that the release of these bubbles will favor the movement of the bath inside the raft and enhance the dissolution. This whole process needs a lot of experimental work to confirm the dynamic and add it to the model. These works include the measurement and analysis of the gas adsorbed at the alumina surface and measuring its rate of release at various temperatures.

- Work has been conducted aside from this project on the microscopic structure of the alumina raft under different conditions. General knowledge has been obtained from this side work that has been included in this thesis. However, a detailed analysis is not directly included here and would be the subject of future publication.

REFERENCES

[155] J. Thonstad, A. Solheim, S. Rolseth, and O. Skar, "The dissolution of alumina in cryolite melts," in *Essential Readings in Light Metals*, 1988, pp. 105–111.

[156] J. Gerlach, U. Henning, and H.-D. Pöthsch, "Zur auflösungskinetik von aluminiumoxid in kryolithschmelzen mit zusätzen von al2o3, alf3, caf2, lif oder mgf2," *Erzmetall*, vol. 31, no. 11, pp. 496–504, 1978.

[157] K. Machado, "Chimie des bains pour l'electrolyse de l'aluminium: Étude rmn haute température et modélisation," Ph.D. dissertation, Université d'Orléans, 2017.

[158] L. Dion, "Modelisation of perfluorocarbon emissions based on the alumina distribution and local current density in an aluminium electrolysis cell," Ph.D. dissertation, Université du Québec à Chicoutimi, 2018.

[159] A. T. Tabereaux and R. D. Peterson, *Chapter 2.5 - Aluminum Production.* Boston: Elsevier, 2014, pp. 839–917.

[160] J. R. Welty, *Fundamentals of momentum, heat, and mass transfer*, 4th ed. New York: J. Wiley, 2001.

APPENDIX A

PUBLICATION AUTHORIZATION

A.1 EMPIRICAL PREDICTION OF ALUMINA DISSOLUTION RATE IN A CRYOLITIC MELT: COMPARISON WITH THE EXISTING LITERATURE.

SPRINGER NATURE LICENSE
TERMS AND CONDITIONS

Aug 29, 2024

This Agreement between Jonathan Alarie ("You") and Springer Nature ("Springer Nature") consists of your license details and the terms and conditions provided by Springer Nature and Copyright Clearance Center.

License Number	5858190227344
License date	Aug 29, 2024
Licensed Content Publisher	Springer Nature
Licensed Content Publication	Springer eBook
Licensed Content Title	Empirical Prediction of Alumina Dissolution Rate in a Cryolitic Melt: Comparison with the Existing Literature
Licensed Content Author	Jonathan Alarie, László I. Kiss, Lukas Dion et al
Licensed Content Date	Jan 1, 2022
Type of Use	Thesis/Dissertation
Requestor type	academic/university or research institute
Format	print and electronic
Portion	full article/chapter
Will you be translating?	no

Circulation/distribution	200 - 499
Author of this Springer Nature content	yes
Title of new work	Dimensional analysis applied to the dissolution and disintegration of alumina rafts : The riddle of dissolving alumina rafts solved.
Institution name	University of Quebec in Chicoutimi
Expected presentation date	Sep 2024
The Requesting Person / Organization to Appear on the License	Jonathan Alarie
Requestor Location	Mr. Jonathan Alarie 2188 Rue des hydrangées Jonquière, QC G7S 5M5 Canada Attn: Mr. Jonathan Alarie
Billing Type	Invoice
Billing Address	Mr. Jonathan Alarie 2188 Rue des hydrangées Jonquière, QC G7S 5M5 Canada Attn: Mr. Jonathan Alarie
Total	0.00 CAD

A.2 DETERMINATION OF THE ALUMINA DIFFUSIVITY AND DISSOLUTION RATE FOR ALUMINA SAMPLES IMMERSED IN A CRYOLITIC BATH

Determination of the alumina diffusivity and dissolution rate for alumina samples immersed in a cryolitic bath

Author:
Jonathan Alarie,László I. Kiss,Lukas Dion,Sébastien Guérard,Jean-François Bilodeau,Renaud Santerre

Publication: Materialia

Publisher: Elsevier

Date: December 2023

A.3 FUNDAMENTAL MASS TRANSFER CORRELATIONS BASED ON EXPERIMENTAL AND LITERATURE DATA.

SPRINGER NATURE LICENSE
TERMS AND CONDITIONS

Jun 13, 2023

This Agreement between Mr. Jonathan Alarie ("You") and Springer Nature ("Springer Nature") consists of your license details and the terms and conditions provided by Springer Nature and Copyright Clearance Center.

License Number	5567160684794
License date	Jun 13, 2023
Licensed Content Publisher	Springer Nature
Licensed Content Publication	Springer eBook
Licensed Content Title	Fundamental Mass Transfer Correlations Based on Experimental and Literature Data
Licensed Content Author	Jonathan Alarie, László I. Kiss, Lukas Dion et al
Licensed Content Date	Jan 1, 2023
Type of Use	Thesis/Dissertation
Requestor type	academic/university or research institute
Format	print and electronic
Portion	full article/chapter
Will you be translating?	no
Circulation/distribution	200 - 499
Author of this Springer Nature content	yes

Title	Étude de la cinétique de dissolution de l'alumine injectée dans un bain de cryolite, par analyse expérimentale et théorique des comportements thermique, chimique et de la dynamique des fluides.
Institution name	University of Quebec in Chicoutimi
Expected presentation date	Aug 2023
Requestor Location	Mr. Jonathan Alarie 2188 Rue des hydrangées Jonquière, QC G7S 5M5 Canada Attn: Mr. Jonathan Alarie
Billing Type	Invoice
Billing Address	Mr. Jonathan Alarie 2188 Rue des hydrangées Jonquière, QC G7S 5M5 Canada Attn: Mr. Jonathan Alarie
Total	0.00 CAD

A.4 DIMENSIONAL ANALYSIS APPLIED TO THE DISSOLUTION AND DISINTEGRATION OF ALUMINA RAFTS : THE RIDDLE OF DISSOLVING ALUMINA RAFTS SOLVED.

SPRINGER NATURE LICENSE
TERMS AND CONDITIONS

Aug 21, 2024

This Agreement between Jonathan Alarie ("You") and Springer Nature ("Springer Nature") consists of your license details and the terms and conditions provided by Springer Nature and Copyright Clearance Center.

License Number	5853740220953
License date	Aug 21, 2024
Licensed Content Publisher	Springer Nature
Licensed Content Publication	Springer eBook
Licensed Content Title	Dimensional Analysis Applied to the Dissolution and Disintegration of Alumina Rafts: The Riddle of Dissolving Alumina Rafts Solved
Licensed Content Author	Jonathan Alarie, László I. Kiss, Lukas Dion et al
Licensed Content Date	Jan 1, 2024
Type of Use	Thesis/Dissertation
Requestor type	academic/university or research institute
Format	print and electronic
Portion	full article/chapter
Will you be translating?	no

Circulation/distribution	200 - 499
Author of this Springer Nature content	yes
Title of new work	Dimensional analysis applied to the dissolution and disintegration of alumina rafts : The riddle of dissolving alumina rafts solved.
Institution name	University of Quebec in Chicoutimi
Expected presentation date	Sep 2024
The Requesting Person / Organization to Appear on the License	Jonathan Alarie
Requestor Location	Mr. Jonathan Alarie 2188 Rue des hydrangées Jonquière, QC G7S 5M5 Canada Attn: Mr. Jonathan Alarie
Billing Type	Invoice
Billing Address	Mr. Jonathan Alarie 2188 Rue des hydrangées Jonquière, QC G7S 5M5 Canada Attn: Mr. Jonathan Alarie
Total	0.00 CAD

A.5 SPRINGER TERMS AND CONDITIONS

The following terms and conditions ("Terms and Conditions") together with the terms specified in your [RightsLink] constitute the License ("License") between you as Licensee and Springer Nature Customer Service Centre GmbH as Licensor. By clicking 'accept' and completing the transaction for your use of the material ("Licensed Material"), you confirm your acceptance of and obligation to be bound by these Terms and Conditions.

1. Grant and Scope of License

1. 1. The Licensor grants you a personal, non-exclusive, non-transferable, non-sublicensable, revocable, world-wide License to reproduce, distribute, communicate to the public, make available, broadcast, electronically transmit or create derivative works using the Licensed Material for the purpose(s) specified in your RightsLink Licence Details only. Licenses are granted for the specific use requested in the order and for no other use, subject to these Terms and Conditions. You acknowledge and agree that the rights granted to you under this License do not include the right to modify, edit, translate, include in collective works, or create derivative works of the Licensed Material in whole or in part unless expressly stated in your RightsLink Licence Details. You may use the Licensed Material only as permitted under this Agreement and will not reproduce, distribute, display, perform, or otherwise use or exploit any Licensed Material in any way, in whole or in part, except as expressly permitted by this License.

1. 2. You may only use the Licensed Content in the manner and to the extent permitted by these Terms and Conditions, by your RightsLink Licence Details and by any applicable laws.

1. 3. A separate license may be required for any additional use of the Licensed Material, e.g. where a license has been purchased for print use only, separate permission must be obtained for electronic re-use. Similarly, a License is only valid in the language selected and does not apply for editions in other languages unless additional translation rights have been granted separately in the License.

1. 4. Any content within the Licensed Material that is owned by third parties is expressly excluded from the License.

1. 5. Rights for additional reuses such as custom editions, computer/mobile applications, film or TV reuses and/or any other derivative rights requests require additional permission and may be subject to an additional fee. Please apply to journalpermissions@springernature.com or bookpermissions@springernature.com for these rights.

2. Reservation of Rights

Licensor reserves all rights not expressly granted to you under this License. You acknowledge and agree that nothing in this License limits or restricts Licensor's rights in or use of the Licensed Material in any way. Neither this License, nor any act, omission, or statement by Licensor or you, conveys any ownership right to you in any Licensed Material, or to any element or portion thereof. As between Licensor and you, Licensor owns and retains all right, title, and interest in and to the Licensed Material subject to the license granted in Section 1.1. Your permission to use the Licensed Material is expressly conditioned on you not impairing Licensor's or the applicable copyright owner's rights in the Licensed Material in any way.

3. Restrictions on use

3. 1. Minor editing privileges are allowed for adaptations for stylistic purposes or formatting purposes provided such alterations do not alter the original meaning or intention of the Licensed Material and the new figure(s) are still accurate and representative of the Licensed Material. Any other changes including but not limited to, cropping, adapting, and/or omitting material that affect the meaning, intention or moral rights of the author(s) are strictly prohibited.

3. 2. You must not use any Licensed Material as part of any design or trademark.

3. 3. Licensed Material may be used in Open Access Publications (OAP), but any such reuse must include a clear acknowledgment of this permission visible at the same time as the figures/tables/illustration or abstract and which must indicate that the Licensed Material is not part of the governing OA license but has been reproduced with permission. This may be indicated according to any standard referencing system but must include at a minimum 'Book/Journal title, Author, Journal Name (if applicable), Volume (if applicable), Publisher, Year, reproduced with permission from SNCSC'.

4. STM Permission Guidelines

4. 1. An alternative scope of license may apply to signatories of the STM Permissions Guidelines ("STM PG") as amended from time to time and made available at https://www.stm-assoc.org/intellectual-property/permissions/permissions-guidelines/.

4. 2. For content reuse requests that qualify for permission under the STM PG, and which may be updated from time to time, the STM PG supersede the terms and conditions contained in this License.

4. 3. If a License has been granted under the STM PG, but the STM PG no longer apply at the time of publication, further permission must be sought from the Rightsholder. Contact journalpermissions@springernature.com or bookpermissions@springernature.com for these rights.

5. Duration of License

5. 1. Unless otherwise indicated on your License, a License is valid from the date of purchase ("License Date") until the end of the relevant period in the below table:

Reuse in a medical communications project	Reuse up to distribution or time period indicated in License
Reuse in a dissertation/thesis	Lifetime of thesis
Reuse in a journal/magazine	Lifetime of journal/magazine
Reuse in a book/textbook	Lifetime of edition
Reuse on a website	1 year unless otherwise specified in the License
Reuse in a presentation/slide kit/poster	Lifetime of presentation/slide kit/poster. Note: publication whether electronic or in print of presentation/slide kit/poster may require further permission.

Reuse in conference proceedings	Lifetime of conference proceedings
Reuse in an annual report	Lifetime of annual report
Reuse in training/CME materials	Reuse up to distribution or time period indicated in License
Reuse in newsmedia	Lifetime of newsmedia
Reuse in coursepack/classroom materials	Reuse up to distribution and/or time period indicated in license

6. Acknowledgement

6. 1. The Licensor's permission must be acknowledged next to the Licensed Material in print. In electronic form, this acknowledgement must be visible at the same time as the figures/tables/illustrations or abstract and must be hyperlinked to the journal/book's homepage.

6. 2. Acknowledgement may be provided according to any standard referencing system and at a minimum should include "Author, Article/Book Title, Journal name/Book imprint, volume, page number, year, Springer Nature".

7. Reuse in a dissertation or thesis

7. 1. Where 'reuse in a dissertation/thesis' has been selected, the following terms apply: Print rights of the Version of Record are provided for; electronic rights for use only on institutional repository as defined by the Sherpa guideline (www.sherpa.ac.uk/romeo/) and only up to what is required by the awarding institution.

7. 2. For theses published under an ISBN or ISSN, separate permission is required. Please contact journalpermissions@springernature.com or bookpermissions@springernature.com for these rights.

7. 3. Authors must properly cite the published manuscript in their thesis according to current citation standards and include the following acknowledgement: '*Reproduced with permission from Springer Nature*'.

8. License Fee

You must pay the fee set forth in the License Agreement (the "License Fees"). All amounts payable by you under this License are exclusive of any sales, use, withholding, value added or similar taxes, government fees or levies or other assessments. Collection and/or remittance of such taxes to the relevant tax authority shall be the responsibility of the party who has the legal obligation to do so.

9. Warranty

9. 1. The Licensor warrants that it has, to the best of its knowledge, the rights to license reuse of the Licensed Material. **You are solely responsible for ensuring that the material you wish to license is original to the Licensor and does not carry the copyright of another entity or third party (as credited in the published version).** If the credit line on any part of the Licensed Material indicates